DYNAMIC PHASE FILTERING WITH INTEGRATED OPTICAL RING RESONATORS

A Dissertation

by

DONALD BENJAMIN ADAMS

Submitted to the Office of Graduate Studies of
Texas A&M University
in partial fulfillment of the requirements for the degree of

DOCTOR OF PHILOSOPHY

August 2010

Major Subject: Electrical Engineering

DYNAMIC PHASE FILTERING WITH INTEGRATED OPTICAL RING RESONATORS

A Dissertation

by

DONALD BENJAMIN ADAMS

Submitted to the Office of Graduate Studies of
Texas A&M University
in partial fulfillment of the requirements for the degree of

DOCTOR OF PHILOSOPHY

Approved by:

Chair of Committee,	Christi K. Madsen
Committee Members,	Ohannes Eknoyan
	Henry Pfister
	Alvin T. Yeh
Head of Department,	Costas N. Georghiades

August 2010

Major Subject: Electrical Engineering

ABSTRACT

Dynamic Phase Filtering with Integrated Optical Ring Resonators. (August 2010)

Donald Benjamin Adams, B.S., Brigham Young University

Chair of Advisory Committee: Dr. Christi K. Madsen

Coherent optical signal processing systems typically require dynamic, low-loss phase changes of an optical signal. Waveform generation employing phase modulation is an important application area. In particular, laser radar systems have been shown to perform better with non-linear frequency chirps. This work shows how dynamically tunable integrated optical ring resonators are able to produce such phase changes to a signal in an effective manner and offer new possibilities for the detection of phase-modulated optical signals.

When designing and fabricating dynamically tunable integrated optical ring resonators for any application, system level requirements must be taken into account. For frequency chirped laser radar systems, the primary system level requirements are good long range performance and fine range resolution. These mainly depend on the first sidelobe level and mainlobe width of the autocorrelation of the chirp. Through simulation, the sidelobe level and mainlobe width of the autocorrelation of the non-linear frequency modulated chirp generated by a series of integrated optical ring resonators is shown to be significantly lower than the well-known tangent-FM chirp.

Proof-of-concept experimentation is also important to verify simulation assumptions. A proof-of-concept experiment employing thermally tunable Silicon-Nitride integrated optical ring resonators is shown to generate non-linear frequency modulated chirp waveforms with peak instantaneous frequencies of 28 kHz.

Besides laser radar waveform generation, three other system level applications of dynamically tunable integrated optical ring resonators are explored in this work. A series of dynamically tunable integrated optical ring resonators is shown to produce constant dispersion which can then help extract complex spectral information. Broadband photonic RF phase shifting for beam steering of a phased array antenna is also shown using dynamically tunable integrated optical ring resonators. Finally all-optical pulse compression for laser radar using dynamically tunable integrated optical ring resonators is shown through simulation and proof-of-concept experimentation.

ACKNOWLEDGEMENTS

I would like to thank everyone who has helped me work on my dissertation and all of the research and study that has gone towards my Ph.D. First and foremost I'd like to thank Dr. C. Madsen for helping me to discover the exciting field of optical signal processing, and always motivating me to do better. I'd also like to thank Dr. O. Eknoyan for his guidance along the path to my Ph.D. Thanks to Dr. H. Pfister and Dr. A. Yeh for serving on my graduate committee, particularly Dr. Pfister who came on board only within the final year. Many thanks to all of my friends who have helped along the way: Mehmet Solmaz, Tim Snider, Wee-Chong Tan, Alex Xia, Sameer Grover, Rafael Salas, Jim Gardner, Dennie Spears, Robert Atkins, J. Paul Chambers, and Michael Thompson; great experiences are measured by the friends you make along the way. Above all I would like to thank my parents and family who have always supported me in every way possible and helped me discover the true joy of learning.

TABLE OF CONTENTS

TABLE OF CONTENTS (continued)

TABLE OF CONTENTS (continued)

LIST OF FIGURES

LIST OF FIGURES (continued)

LIST OF FIGURES (continued)

LIST OF FIGURES (continued)

LIST OF FIGURES (continued)

LIST OF FIGURES (continued)

LIST OF FIGURES (continued)

LIST OF FIGURES (continued)

CHAPTER I

INTRODUCTION

A. Background and Applications Preview

In optical and electrical engineering, filters traditionally are used to change the amplitude response of a signal. In fact, in most applications require that the filter have a linear phase response to ensure minimal impact on the dispersion of a signal. In this light, the concept of a filter that passes all amplitudes equally and only changes the phase of a signal seems almost absurd.

As fiber optic based communication systems became more popular though, a common problem began to surface, optical dispersion. Optical dispersion arises from the fact that the refractive index of standard optical fiber varies slightly depending on wavelength. This slight variation in turn causes short pulses to spread temporally based on wavelength because the wavelengths in a pulse that see a lower refractive index effectively travel faster. Therefore, to maintain high bit rates without signal degradation, some sort of dispersion compensation is required.

Dispersion is proportional to the second derivative of optical phase. From this perspective, dispersion compensation becomes optical phase filtering. In other words, to compensate for dispersion effects, a filter is needed that passes the amplitudes equally and only changes the optical phase of a signal. Generally, these filters are called optical all-pass filters.

This dissertation follows the style of *IEEE Journal of Lightwave Technology*.

Historically, dispersion compensation began by creating custom fibers that had little to no dispersion, but these fibers tended to have optical non-linearity problems [1]. Then dispersion compensating fibers that had a negative dispersion were created, but a great deal of dispersion compensating fiber must be passed through to restore the signal [2]. Chirped fiber-Bragg gratings were also investigated and were found to have very good dispersion compensation characteristics without needing long lengths of fiber [3]. Chirped fiber-Bragg gratings continue to see wide-spread use.

Optical ring resonators were shown to have tunable dispersion characteristics early on [4]. But it wasn't until optical ring resonators began to be incorporated into an integrated platform that their true benefits began to be exploited [5]. Integrated optical ring resonators allow for much more dynamic filtering characteristics on a compact platform.

Dispersion compensation is certainly not the only application of integrated optical ring resonators. A huge horizon of optical signal processing applications exist from many areas such as: optical filtering, lasers, RF photonics, chemical and bio-sensing, signal characterization, optical modulation, and so forth. As each area has its own distinct requirements, it is likely that no one design or even integration technology will suit them all. Nonetheless a great deal of research is continuing to go towards integrated optical ring resonator technology.

This dissertation will investigate four distinct applications of integrated optical ring resonators: complex optical spectrum analysis, RF photonic phase shifters, LADAR waveform generation, and group-delay based all-optical pulse compression. The

benefits of integrated optical ring resonators over existing techniques will be shown through simulation and proof-of-concept experimentation.

B. Chapter Overview

Integrated optical ring resonator research generally covers three major areas of study: electromagnetics/optics, solid-state physics and fabrication, and signal processing. Each one is important in the understanding of integrated optical ring resonator function; therefore a brief review of each will be given in this dissertation. In Chapter II, a review of optical/electromagnetic theory will be shown. In Chapter III, an overview of current fabrication technology will be given. In Chapter IV, the basic signal processing theory behind optical ring resonators will be shown.

One of the keys to understanding optical ring resonators is understanding the systems that measure them. Therefore, in Chapter V, a review of the measurement systems used for integrated optical ring resonator characterization will be given. This includes not only a review of current function, but also of additional modifications added to the system to improve performance.

Then, in Chapters VI through IX, we will show the actual applications of integrated optical ring resonators; Chapter VI covering the complex optical spectrum analyzer, Chapter VII covering the RF/photonic phase shifter, Chapter VIII covering the LADAR waveform generator, and Chapter IX covering the group-delay based all-optical pulse compressor. Finally, in Chapter X, we will draw some conclusions and look forward into what future research may be pursued for each of these applications.

CHAPTER II

OPTICS REVIEW

A. Representations: Ray Optics, Wave Optics, and Quantum Optics

Although light pervades human existence, its fundamental nature remains at least a partial mystery. We know how to quantify light phenomena and make predictions based on this knowledge, and we know how to use and control light for our own convenience. Yet light is often interpreted in different ways to explain different experiments and observations: sometimes light behaves in a geometrical ray-like way, sometimes light behaves as a particle, and sometimes light behaves like a wave. A great many text-books reviewing these various representations can be found; the ensuing discussion will follow the material from some of these [6]-[9].

A.1 Ray optics

A number of optic phenomena are adequately explained by considering that the optical energy in a wave follows narrow paths, called rays. Rays obey a few simple rules:

1. In a vacuum rays travel at the velocity $c = 3 \times 10^8 \ {}^{m}/_{s}$. In any other medium rays travel at a slower speed given by

$$v = \frac{c}{n} \tag{2.1}$$

   where n is the refractive index of the medium.
2. Rays travel in straight paths unless deflected by some change in the medium.
3. At a plane boundary between two media, a ray is reflected at an angle equal to the angle of incidence.

4. If any power crosses the boundary, the transmitted ray direction is given by Snell's law:

$$\frac{\sin(\theta_t)}{\sin(\theta_i)} = \frac{n_1}{n_2} \qquad 2.2$$

where θ_t is the transmitted angle, θ_i is the incident angle, and n_1 and n_2 are the refractive indices of the incident and transmission regions, respectively.

Although ray optics provides some insights into waveguide operation, it is generally most useful for understanding lenses, mirrors, and other bulk optics. As the experiments in this dissertation primarily employ optical waveguides and not bulk optical devices no further discussion of ray optics will pursued.

A.2 Quantum optics

Sometimes light behaves as though it were made up of very small particles called photons. The energy of a single photon is:

$$W_p = hf \qquad 2.3$$

where $h = 6.626 \times 10^{-34}\, J \cdot s$ and is called Planck's constant. Particle theory explains generation of light by sources and amplifiers, as well as explaining detection of light by conversion of optical radiation to electrical current. Although any optical signal processing system necessitates the use of optical sources and detectors, the quantum level effects of these devices will not be studied extensively in this dissertation. Therefore, no further explanation of quantum optics will be given.

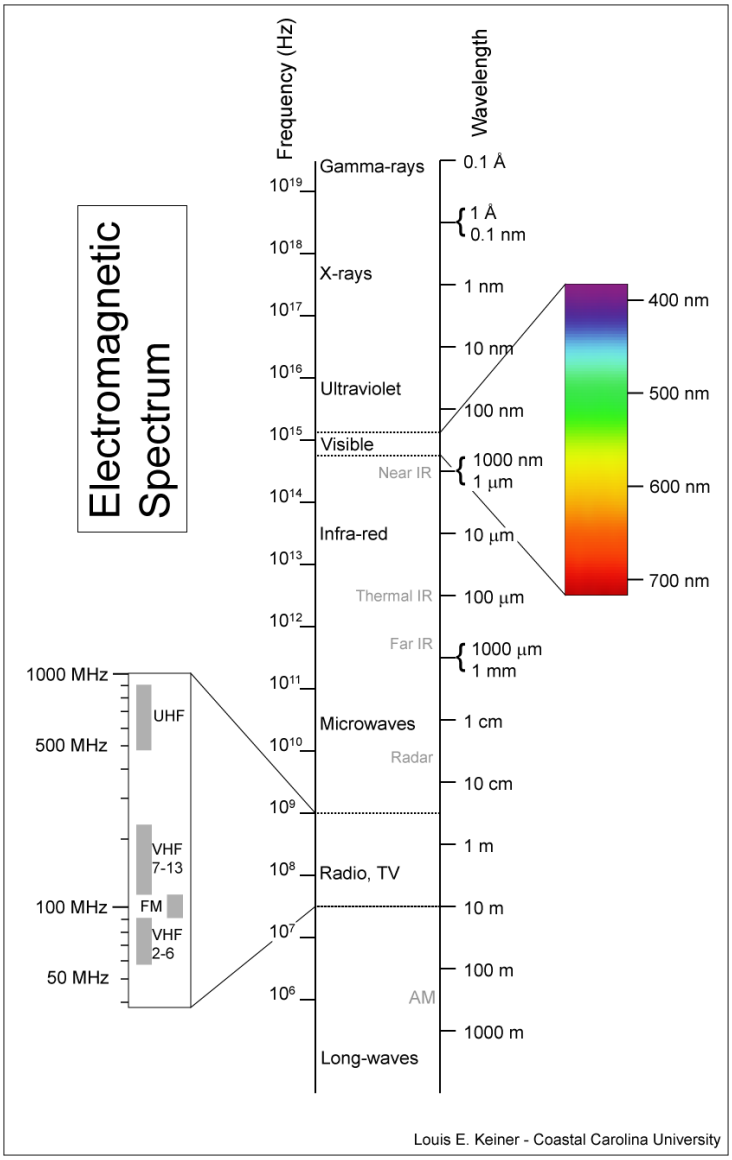

Fig. 1 The electromagnetic spectrum.

A.3 Wave optics

Many light phenomena can be explained if we look at light as being an electromagnetic wave having a very high oscillation frequency and a very short wavelength. The electromagnetic spectrum can be seen in Fig. 1. The portion of the

electromagnetic spectrum visible to the human eye is actually quite small, including wavelengths only from about 400 nm to 700nm. The term optic (as well as the term light) generally refers to frequencies in the infrared, visible, and ultraviolet portions of the spectrum because so many of the same analyses, techniques, and devices are applicable to these ranges.

The frequency of an electromagnetic wave is determined by the emitting source and does not change when the light travels from one material to another. Instead, the velocity of the wave changes and this difference causes a change in wavelength given by:

$$\lambda = \frac{v}{f} \tag{2.4}$$

where v is the beam velocity, and f is its frequency. Unless otherwise specified, all wavelengths refer to the free-space wavelength.

Electromagnetic waves often are represented as a function of both time and position such as:

$$E = E_o \sin(\omega t - kz) \tag{2.5}$$

or

$$E = E_o e^{j(\omega t - kz)} \tag{2.6}$$

where E_o is the peak amplitude, $\omega = 2\pi f \ {}^{rad}/_{s}$, and k is the propagation factor given by:

$$k = \frac{\omega}{v} \tag{2.7}$$

If a wave does not lose energy as it propagates then (2.5) and (2.6) provide appropriate descriptions. If attenuation is important however, then (2.5) and (2.6) must be modified as follows:

$$E = E_o e^{-\alpha z} \sin(\omega t - kz) \tag{2.8}$$

and

$$E = E_o e^{-\alpha z} e^{j(\omega t - kz)} \tag{2.9}$$

where α is the attenuation coefficient. The use of complex notation is standard in electromagnetic theory, but it should be noted that only the real parts of the complex exponential are physically significant.

Wave theory forms the mathematical foundation of optical waveguides and will be the principle optical representation used in this dissertation. No discussion of optical wave theory would be complete without a review of Maxwell's equations.

B. Electromagnetic Theory

B.1 Maxwell's equations

Maxwell's equations are the governing equations for electromagnetic wave propagation. In fact, Maxwell's equations describe not only wave propagation at high frequencies, but also zero hertz electrostatics and everything in between. Maxwell's equations in time domain point form are:

$$\nabla \times \boldsymbol{\mathcal{E}}(r,t) = \frac{-\delta}{\delta t}\boldsymbol{\mathcal{B}}(r,t) \tag{2.10}$$

$$\nabla \times \boldsymbol{\mathcal{H}}(r,t) = \frac{\delta}{\delta t}\boldsymbol{\mathcal{D}}(r,t) - \boldsymbol{\mathcal{J}}(r,t) \tag{2.11}$$

$$\nabla \cdot \boldsymbol{\mathcal{D}}(r,t) = \rho(r,t) \tag{2.12}$$

$$\nabla \cdot \mathcal{B}(r,t) = 0 \tag{2.13}$$

where $\mathcal{E}(r,t)$ is the electric field vector, $\mathcal{B}(r,t)$ is the magnetic flux density vector, $\mathcal{H}(r,t)$ is the magnetic field vector, $\mathcal{D}(r,t)$ is the electric flux density vector, $\mathcal{J}(r,t)$ is the density vector of free currents, and $\rho(r,t)$ is the volume density of free charge.

Maxwell's equations in this form are a little bit unwieldy for our purposes. A linear (μ and ε are independent of $\mathcal{E}$ and $\mathcal{H}$), non-magnetic ($\mu = \mu_0$), dielectric medium free of currents and charge sources ($\mathcal{J} = 0$ and $\rho = 0$) gives the relations:

$$\mathbf{D} = \varepsilon \mathbf{E} \tag{2.14}$$

$$\mathbf{B} = \mu_0 \mathbf{H} \tag{2.15}$$

where if the medium is isotropic:

$$\begin{bmatrix} \mathrm{D_x} \\ \mathrm{D_y} \\ \mathrm{D_z} \end{bmatrix} = \begin{bmatrix} \varepsilon_{xx} & \varepsilon_{xy} & \varepsilon_{xz} \\ \varepsilon_{yx} & \varepsilon_{yy} & \varepsilon_{yz} \\ \varepsilon_{zx} & \varepsilon_{zy} & \varepsilon_{zz} \end{bmatrix} \begin{bmatrix} \mathrm{E_x} \\ \mathrm{E_y} \\ \mathrm{E_z} \end{bmatrix}. \tag{2.16}$$

Maxwell's equations in frequency domain point form then simplify into:

$$\nabla \times \mathbf{E} = -j\omega\mu_0 \mathbf{H} \tag{2.17}$$

$$\nabla \times \mathbf{H} = j\omega\varepsilon \mathbf{E} \tag{2.18}$$

$$\nabla \cdot \mathbf{E} = 0 \tag{2.19}$$

$$\nabla \cdot \mathbf{H} = 0. \tag{2.20}$$

B.2 The wave equation

If we take the curl of both sides of 2.17:

$$\nabla \times \nabla \times \mathbf{E} = \nabla \times -j\omega\mu_0 \mathbf{H} \tag{2.21}$$

then simplify the left side using vector identities and plug (2.18) into the right side:

$$-\nabla^2\mathbf{E} + \nabla(\nabla \cdot \mathbf{E}) = -j\omega\mu_0(j\omega\varepsilon\mathbf{E}) \quad 2.22$$

finally noting (2.19) and rearranging we get:

$$\nabla^2\mathbf{E} + k^2\mathbf{E} = 0 \quad 2.23$$

where $k = \omega\sqrt{\mu\varepsilon}$. This equation is known as the vector Helmholtz equation or the wave equation. Expanding (2.23) gives

$$\left(\frac{\delta^2}{\delta x^2} + \frac{\delta^2}{\delta y^2} + \frac{\delta^2}{\delta z^2} + k^2\right)\mathbf{E} = 0 \quad 2.24$$

B.3 Plane wave solution

For a plane wave propagating along z, there is no variation in the transverse direction; so the derivatives with respect to x and y are zero, leaving:

$$\frac{\delta^2\mathbf{E}}{\delta z^2} + k^2\mathbf{E} = 0. \quad 2.25$$

The full solution of this ordinary differential equation, including time domain variation is:

$$\mathbf{E}(z) = E_{0+}e^{j(\omega t - kz)} + E_{0-}e^{j(\omega t + kz)}. \quad 2.26$$

By plotting the first and second terms as a function of z at different times, it becomes obvious that the first term describes a plane wave traveling along the positive z direction while the second term describes a plane wave traveling along the negative z direction.

The above solution was calculated for a wave traveling along the z axis. For a general situation, the solution for a forward traveling wave will be of the following form:

$$\mathbf{E}(\mathbf{r}) = \boldsymbol{E}_{\mathbf{0}+}e^{j(\omega t - \boldsymbol{k}\mathbf{r})} \quad 2.27$$

where $\mathbf{r}$ is the position vector, and $\boldsymbol{k}$ is the wave vector.

B.4 Dielectric interfaces

The reflection and transmission of electromagnetic waves at dielectric boundaries is fairly well described by ray optics, but how does wave theory and Maxwell's equations factor into our understanding of dielectric boundaries? For the following discussion we'll assume that an electromagnetic plane wave encounters an infinite dielectric boundary at an angle θ_i as seen in Fig. 2.

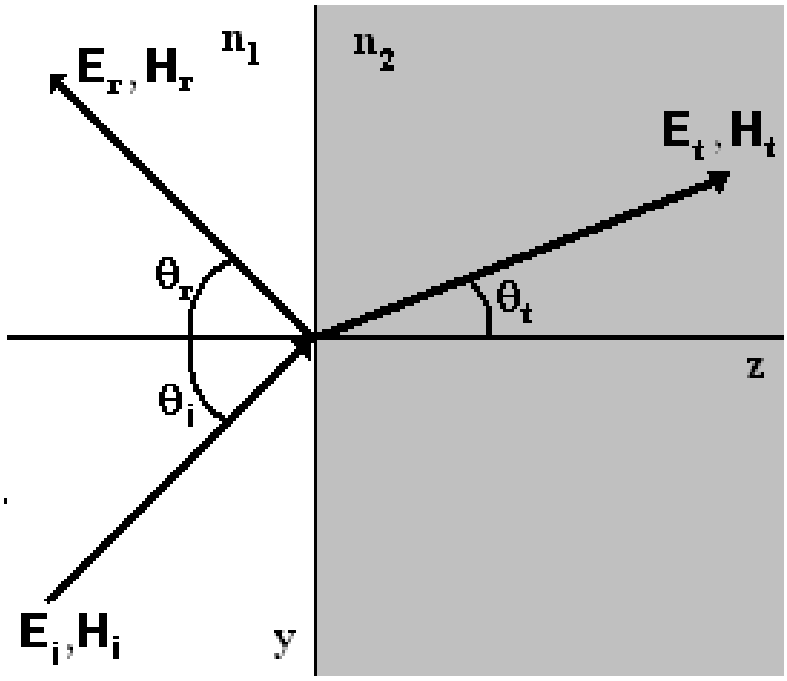

Fig. 2 Plane wave at an infinite dielectric interface.

The rules connecting the reflected and the transmitted fields to the incident field are the boundary conditions:

$$\mathbf{n} \times (\mathbf{E_2} - \mathbf{E_1}) = 0 \qquad 2.28$$

and:

$$\mathbf{n} \times (\mathbf{H_2} - \mathbf{H_1}) = 0. \tag{2.29}$$

Assuming that the reflected and transmitted waves are also plane waves:

$$\mathbf{E_i} = \mathbf{E_i^a} e^{-j\boldsymbol{k_i r}} = \mathbf{E_i^a} e^{j(k_1 y\, sin(\theta_i) - k_1 z\, cos(\theta_i))} \tag{2.30}$$

$$\mathbf{E_r} = \mathbf{E_r^a} e^{-j\boldsymbol{k_r r}} = \mathbf{E_r^a} e^{j(k_1 y\, sin(\theta_i) + k_1 z\, cos(\theta_i))} \tag{2.31}$$

$$\mathbf{E_t} = \mathbf{E_t^a} e^{-j\boldsymbol{k_t r}} = \mathbf{E_t^a} e^{j(k_2 y\, sin(\theta_t) - k_2 z\, cos(\theta_t))} \tag{2.32}$$

where

$$\boldsymbol{k_i r} = (k_1 y\, sin(\theta_i) - k_1 z\, cos(\theta_i)) \tag{2.33}$$

$$\boldsymbol{k_r r} = (k_1 y\, sin(\theta_i) + k_1 z\, cos(\theta_i)) \tag{2.34}$$

$$\boldsymbol{k_t r} = (k_2 y\, sin(\theta_t) - k_2 z\, cos(\theta_t)) \tag{2.35}$$

(2.28) becomes:

$$\mathbf{n} \times (\mathbf{E_i^a} e^{jk_1 y\, sin(\theta_i)} + \mathbf{E_r^a} e^{jk_1 y\, sin(\theta_i)}) = \mathbf{n} \times \mathbf{E_t^a} e^{jk_2 y\, sin(\theta_t)} \tag{2.36}$$

$$\mathbf{n} \times (\mathbf{E_i^a} + \mathbf{E_r^a}) e^{jk_1 y\, sin(\theta_i)} = \mathbf{n} \times \mathbf{E_t^a} e^{jk_2 y\, sin(\theta_t)}. \tag{2.37}$$

Equating phases

$$k_1 y\, sin(\theta_i) = k_2 y\, sin(\theta_t) \tag{2.38}$$

and relating wave vectors to their wave velocities:

$$k_1 = \frac{\omega}{v_1} = \omega\sqrt{\mu_1 \varepsilon_1} = \frac{\omega}{n_1 c} \tag{2.39}$$

$$k_2 = \frac{\omega}{v_2} = \omega\sqrt{\mu_2 \varepsilon_2} = \frac{\omega}{n_2 c} \tag{2.40}$$

gives us Snell's law:

$$\frac{\omega}{n_1 c}\, sin(\theta_i) = \frac{\omega}{n_2 c} sin(\theta_t) \tag{2.41}$$

or:

$$\frac{\sin(\theta_t)}{\sin(\theta_i)} = \frac{n_1}{n_2}. \quad 2.42$$

Let us now use the boundary conditions to establish the amplitude relationship among the incident, reflected and transmitted fields. Although all the wave vectors lie on the same incident plane, each wave vector has associated with it two independent directions of polarization. It is therefore necessary to discuss the two cases separately: **E** perpendicular and **E** parallel to the incident plane.

Case (1) : **E** perpendicular to the incident plane. Applying (2.28 – 2.29):

$$\mathbf{E_{i\perp}} + \mathbf{E_{r\perp}} = \mathbf{E_{t\perp}} \quad 2.43$$

$$\mathbf{H_{i\perp}} cos(\theta_i) + \mathbf{H_{r\perp}} cos(\theta_r) = \mathbf{H_{t\perp}} cos(\theta_t) \quad 2.44$$

Because $\mathbf{H} = \sqrt{\varepsilon/\mu}\,\mathbf{E}$ and $\mu = \mu_0$ (2.44) becomes

$$\sqrt{\varepsilon_1}(\mathbf{E_{i\perp}} - \mathbf{E_{r\perp}})cos(\theta_i) = \sqrt{\varepsilon_2}\mathbf{E_{t\perp}} cos(\theta_t). \quad 2.45$$

Combining (2.42 – 2.44) yields:

$$\frac{\mathbf{E_{r\perp}}}{\mathbf{E_{i\perp}}} = \mathbf{R}_\perp = \frac{sin(\theta_i - \theta_t)}{sin(\theta_i + \theta_t)} \quad 2.46$$

and:

$$\frac{\mathbf{E_{t\perp}}}{\mathbf{E_{i\perp}}} = \mathbf{T}_\perp = \frac{2\cos(\theta_i)\sin(\theta_t)}{\sin(\theta_i + \theta_t)} \quad 2.47$$

where $\mathbf{R}_\perp$ and $\mathbf{T}_\perp$ are the reflection and transmission coefficients for the perpendicular case respectively.

Case (2) : **E** parallel to the incident plane. Applying (2.28 – 2.29):

$$\mathbf{E_{i\parallel}} cos(\theta_i) + \mathbf{E_{r\parallel}} cos(\theta_r) = \mathbf{E_{t\parallel}} cos(\theta_t) \quad 2.48$$

$$\mathbf{H_{i\parallel}} + \mathbf{H_{r\parallel}} = \mathbf{H_{t\parallel}} \tag{2.49}$$

Again because $\mathbf{H} = \sqrt{\varepsilon/\mu}\,\mathbf{E}$ and $\mu = \mu_0$ (2.49) becomes

$$\sqrt{\varepsilon_1}(\mathbf{E_{i\parallel}} - \mathbf{E_{r\parallel}}) = \sqrt{\varepsilon_2}\mathbf{E_{t\parallel}}. \tag{2.50}$$

Combining 2.42, 2.48, and 2.50:

$$\frac{\mathbf{E_{r\parallel}}}{\mathbf{E_{i\parallel}}} = \mathbf{R}_{\parallel} = \frac{tan(\theta_i - \theta_t)}{tan(\theta_i + \theta_t)} \tag{2.51}$$

and:

$$\frac{\mathbf{E_{t\parallel}}}{\mathbf{E_{i\parallel}}} = \mathbf{T}_{\parallel} = \frac{2\cos(\theta_i)\sin(\theta_t)}{sin(\theta_i + \theta_t)\cos(\theta_i - \theta_t)} \tag{2.52}$$

where $\mathbf{R}_{\parallel}$ and $\mathbf{T}_{\parallel}$ are the reflection and transmission coefficients for the parallel case respectively. Equations (2.46), (2.47), (2.51), and (2.52) describe the ratio of reflected and transmitted field amplitude to the incident field amplitude, and are sometimes referred to as the Fresnel formulas.

B.5 Brewster and critical angles

Two cases are of special note. For the parallel polarization, if:

$$\theta_i + \theta_t = \frac{\pi}{2} \tag{2.53}$$

there is no reflection coefficient according to (2.51). Equation (2.53) is called Brewster's law, and the incident angle is referred to as the Brewster angle.

The second special case, which will become more important in the sections that follow, is the law of total internal reflection. If the refractive index of material 1 is greater than the refractive index of material two, aka:

$$n_1 > n_2 \tag{2.54}$$

then according to Snell's law the transmitted angle will be greater than (or equal to) the incident angle:

$$\theta_t > \theta_i \tag{2.55}$$

If the incident angle is sufficiently large, there will be total reflection of the incident wave. The angle at which this occurs is called the critical angle:

$$\sin(\theta_c) = \frac{n_2}{n_1} \tag{2.56}$$

If the incident angle is greater than the critical angle, the transmitted wave vector becomes imaginary. Remember:

$$\boldsymbol{k_t r} = k_2 y \sin(\theta_t) - k_2 z \cos(\theta_t) \tag{2.57}$$

$$\boldsymbol{k_t r} = k_2 y \sin(\theta_t) - z\sqrt{k_2^2 - k_2^2 \sin^2(\theta_t)} \tag{2.58}$$

Using Snell's law:

$$k_1 \sin(\theta_i) = k_2 \sin(\theta_t) \tag{2.59}$$

(2.58) becomes:

$$\boldsymbol{k_t r} = k_1 y \sin(\theta_i) - z\sqrt{k_2^2 - k_1^2 \sin^2(\theta_i)} \tag{2.60}$$

and if $\theta_i > \theta_c$ then $k_1^2 \sin^2(\theta_i) > k_2^2$ and the z-component of the wave vector is imaginary. This can be seen as a wave propagating along the y direction with a decaying component in the z-direction. In other words, this transmitted wave exists only at regions very close to the interface.

C. Waveguide Theory

C.1 Dielectric slab waveguide

Consider the dielectric slab waveguide shown in Fig. 3. The field in the film is a plane wave zigzagging back and forth at the angle θ. Somewhat similarly, we can view the total field as the sum of two uniform plane waves, one traveling upward at angle θ and one traveling downward at that angle. These waves have a propagation factor that can be written as $k = k_0 n_1$ where k_0 is the free-space propagation factor. The guided wave's net direction of travel is horizontal in this figure. The component of the propagation factor along this direction is:

$$\beta = k \sin(\theta) = k_0 n_1 \sin(\theta) \tag{2.61}$$

called the longitudinal propagation factor. Because of the interference between the upward- and downward-traveling waves, the field is not uniform along the y-direction, but varies sinusoidally. This variation is the standing-wave pattern. The field in the film can be written as:

$$\mathbf{E} = \mathbf{E_1} \cos(hy) \sin(\omega t - \beta z) \tag{2.62}$$

for modes evenly distributed about the $y = 0$ plane. Fields having an odd distribution are represented by:

$$\mathbf{E} = \mathbf{E_1} \sin(hy) \sin(\omega t - \beta z). \tag{2.63}$$

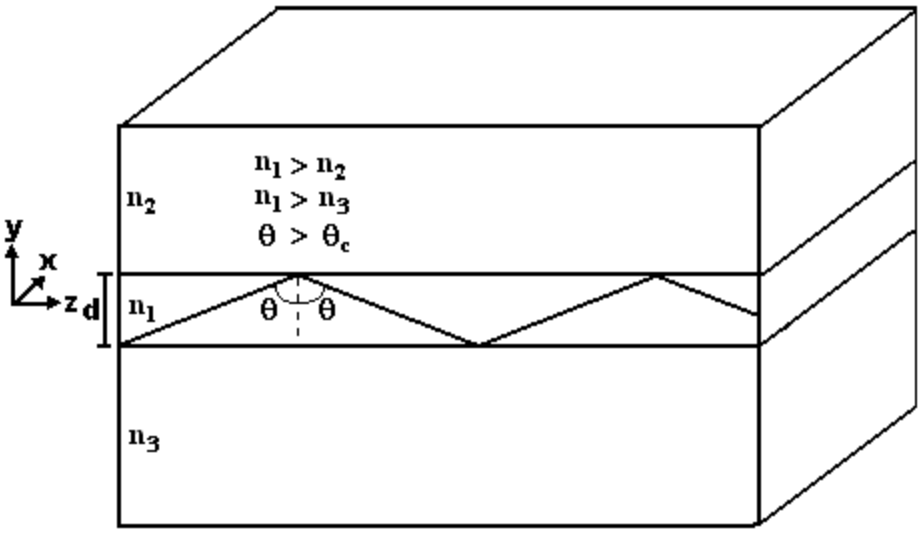

Fig. 3 Asymmetric dielectric-slab waveguide, $n_1 > n_2, n_1 > n_3$

.

In (2.62 – 2.63), $\mathbf{E_1}$ is the peak value of the electric field and $h = k\cos(\theta)$. (h is the vertical component of the propagation factor k.) The midpoint of the central layer is located at $y = 0$. Comparison with (2.5) for an unguided wave shows the same variation along the direction of travel, except for the replacement of k by β. By making this replacement in (2.7) we can write the relationship between the waveguide phase velocity v_g and the longitudinal propagation factor:

$$\beta = \frac{\omega}{v_g} \qquad 2.64$$

or:

$$v_g = \frac{\omega}{\beta}. \qquad 2.65$$

The effective refractive index is defined as the free-space velocity divided by the guided wave velocity. That is:

$$n_{eff} = \frac{c}{v_g} \tag{2.66}$$

Using (2.65) and (2.7) we obtain:

$$n_{eff} = \frac{\beta}{k_0} \tag{2.67}$$

or using (2.61):

$$n_{eff} = n_1 \sin(\theta) \tag{2.68}$$

Evanescent fields outside the film decay exponentially as:

$$\mathbf{E} = \mathbf{E_2}\ e^{-\alpha_2(y-d/2)}\ \sin(\omega t - \beta z) \tag{2.69}$$

for the upper layer ($y \geq d/2$), and:

$$\mathbf{E} = \mathbf{E_3}\ e^{\alpha_3(y+d/2)}\ \sin(\omega t - \beta z) \tag{2.70}$$

for the lower layer ($y \leq d/2$). $\mathbf{E_2}$ and $\mathbf{E_3}$ are the peak values of the electric field at the lower and upper boundaries respectively. The evanescent decay factor α_2 and α_3 can be derived from (2.60):

$$\alpha_2 = k_0\sqrt{(n_1^2 sin^2(\theta_i) - n_2^2)} \tag{2.71}$$

and:

$$\alpha_3 = k_0\sqrt{(n_1^2 sin^2(\theta_i) - n_3^2)}. \tag{2.72}$$

C.2 Mode condition

Many waves may be launched into the dielectric slab waveguide that have directions such that they encounter the lower and upper boundaries at angles greater than both critical angles. Although these waves will be contained by the waveguide, not all will propagate along the structure. Only waves that have a stable interference pattern

will propagate, aka. waves that experience a round-trip phase shift equal to an integer multiple of 2π radians. This resonance condition is given by:

$$\Delta\varphi = m2\pi. \tag{2.73}$$

Waves that satisfy this condition are called the modes of the waveguide. Just as reflections at a dielectric interface are different for the TE and TM polarizations of an optical wave, the modes of a waveguide also are different for the TE and TM polarizations. For TE modes the solution to (2.73) is:

$$\tan(hd) = \frac{(p+q)}{\left(h - \frac{pq}{h}\right)} \tag{2.74}$$

where:

$$\mathrm{h} = \sqrt{k_0^2 n_1^2 - \beta^2} \tag{2.75}$$

$$\mathrm{p} = \sqrt{\beta^2 - k_0^2 n_3^2} \tag{2.76}$$

and;

$$\mathrm{q} = \sqrt{\beta^2 - k_0^2 n_2^2}. \tag{2.77}$$

For TM modes the solution to (2.73) is almost the same:

$$\tan(hd) = \frac{\left(\frac{n_1^2}{n_3^2}p + \frac{n_1^2}{n_2^2}q\right)}{\left(h - \left(\frac{n_1^2}{n_2 n_3}\right)\frac{pq}{h}\right)}. \tag{2.78}$$

Equations (2.74) and (2.78) are called the transcendental equations.

The variation of light across the plane transverse to the waveguide axis is the transverse mode pattern. According to (2.62 – 2.63) the electric field in the film varies

sinusoidally across the transverse plane. Outside the film, there is an exponentially decaying evanescent field, given by (2.69 – 2.70). Penetration into the outer layer increases as the mode order increases. For a fixed thickness and wavelength, each mode has a different pattern. A few of these are drawn in Fig. 4.

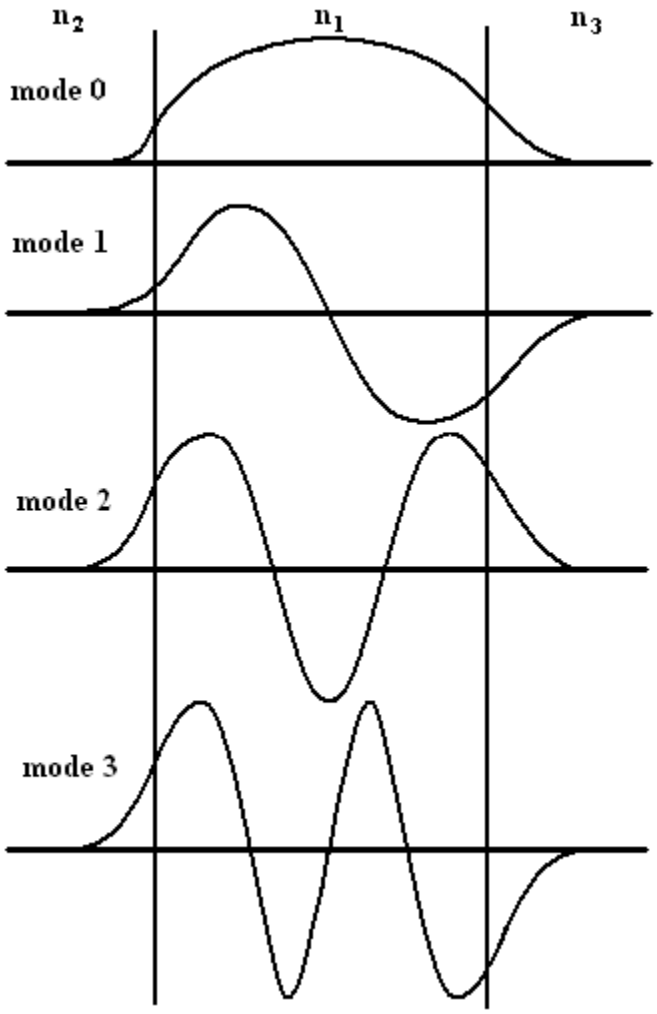

Fig. 4 Transverse mode pattern in the asymmetric dielectric slab waveguide.

Up to this point we have assumed a step-index waveguide; the dielectric interfaces sharply transitioning from one index to another. Sometimes the dielectric interface has a gradual transition from one index to another; such create graded-index waveguides. In this case the refractive index is a function of position y, which changes (2.75) as follows:

$$\mathrm{h} = \sqrt{k_0^2(n_1(y))^2 - \beta^2}. \qquad 2.79$$

C.2 Three-dimensional waveguides

For most real-world applications, optical waveguides must confine light along two dimensions; e.g. if the waveguide propagates light along the z-axis the light must be confined in both the x and y axes.

Microwave rectangular waveguides with perfect conductor walls can support pure TE and TM modes. On the contrary optical 3-D waveguides surrounded by different dielectric materials do not support pure TE and TM modes. Rather two families of hybrid modes exist, which are essentially TEM modes polarized along the x and y directions. The mode having the main electric field in the x direction resembles the TM mode in a slab waveguide; therefore this mode is frequently referred to as the TM mode even though strictly speaking it isn't a pure TM mode. Likewise the mode having the main electric field in the y direction resembles the TE mode in a slab waveguide, therefore this mode is frequently referred to as the TE mode.

Generally, the boundary value problem for 3-D waveguides cannot be solved accurately without resorting to numerical solutions. Some approximation methods

include Marcatili's method and the effective index method, but a description of such is beyond the scope of this dissertation. More information can be found in [8].

CHAPTER III

DEVICE FABRICATION

A. Waveguide Types

Although waveguides come in many forms, most real-world optical waveguides fall into one of two categories: deposited-ridge waveguides (Fig. 5 a) and channel diffused waveguides (Fig. 5 b).

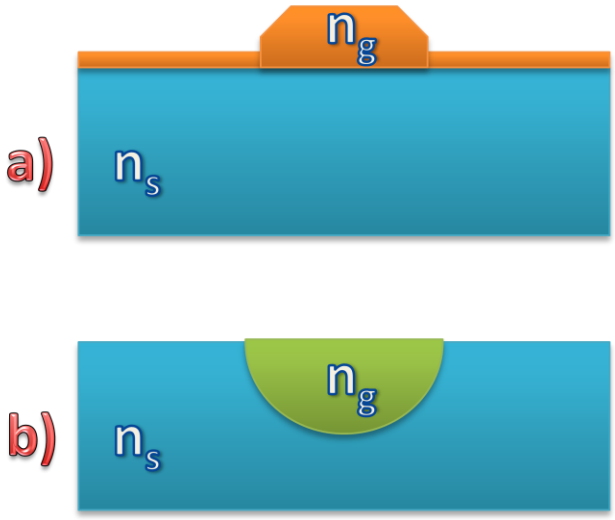

Fig. 5 a) Deposited ridge waveguide. b) Channel diffused waveguide. $n_g > n_s$.

A.1 Deposited ridge waveguides

Deposited ridge waveguides are usually fabricated by depositing a higher index film (ng) on a substrate (ns), followed by patterning and removal of the undesired film through wet or dry etching. Generally the deposited film has a significantly higher index than the substrate or cladding giving the waveguide much tighter mode confinement (see

Fig. 6.) This allows deposited ridge waveguides to have very small bend radii; as low as 10s of micrometers. Small bend radii in turn lead to more fabricated devices per chip. The shortcoming of deposited ridge waveguides is significant scattering losses due to waveguide wall roughness.

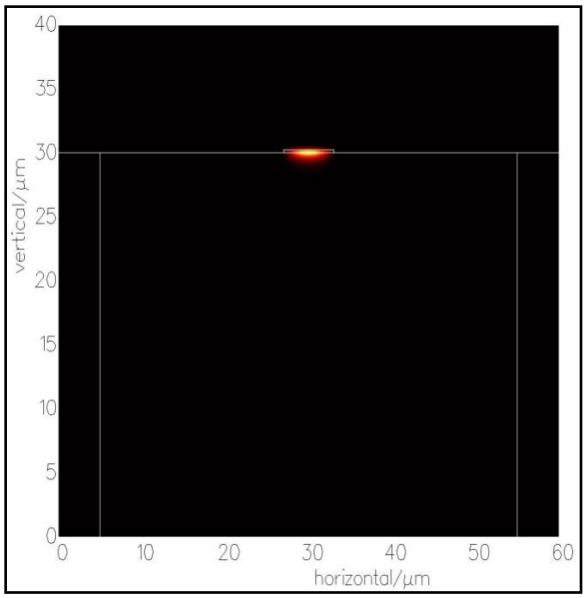

Fig. 6 Waveguide mode of a typical deposited ridge waveguide; size 0.3um by 6um.

A.2 Channel diffused waveguides

Channel diffused waveguides can be formed in a variety of ways. The most common technique is to diffuse a metal into the substrate and thus increase the refractive index in the diffused region. Other techniques include ion-exchange, ion implantation, and light or electron beam irradiation. Channel diffused waveguides almost always exhibit graded profiles as opposed to the step index transition common among deposited

ridge waveguides. This allows low propagation loss channel waveguides to be fabricated with ease.

On the other hand, channel diffused waveguides generally have very low index contrasts ($\Delta n < 0.001$). Therefore bent waveguide structures will frequently show high losses, and the minimum bend radius is typically on the order of centimeters. Therefore channel diffused waveguides usually cannot achieve as many fabricated devices on-chip as deposited ridge waveguides.

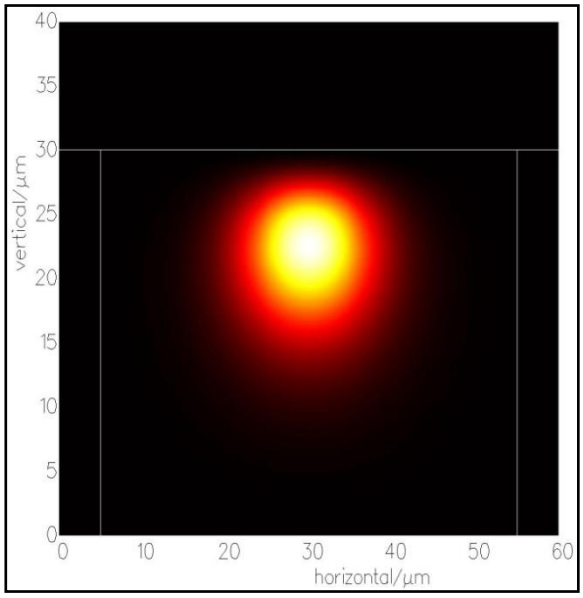

Fig. 7 Waveguide mode of a typical channel diffused waveguide; size 12um by 15um.

B. Fabrication Materials

Integrated optical waveguides have been demonstrated with many different materials including glass, chalcogenide, lithium-niobate, silicon, silicon-nitride, and

many others. Understanding these materials and their associated fabrication techniques is the key to successful optical device fabrication and implementation in real-world problems.

B.1 Silicon based fabrication

Silicon has a band-gap energy of 1.12 eV, which places its absorption band edge at a wavelength of 1.1μm. For wavelengths shorter than this silicon is highly absorbing, but its transparency extends well into the infrared. Its refractive index is about equal to 3.5 at wavelengths near 1.5μm. Silicon-nitride (Si_3N_4) on the other hand has a band-gap energy of about 2.4 eV, so its absorption band-edge is down at wavelengths of about 0.5μm, but its transparency also extends through most of the infrared. Its refractive index is about equal to 2.05 at wavelengths near 1.5μm [10].

The great advantage of silicon and silicon-nitride fabrication is the ability to use the same fabrication techniques developed for integrated electronics. Although low index contrast channel diffused waveguides can be fabricated by properly doping the silicon substrate, deposited ridge waveguides are more common. Fabrication is generally done on a silicon substrate with a fairly thick thermally grown oxide layer. The refractive index of silicon-dioxide is around 1.5 at wavelengths near 1.5μm, so this layer serves as an optical buffer layer from the high refractive index of the silicon substrate (~3.5). Then, a thin layer of silicon or silicon-nitride (usually about 100 to 500nm) is grown on top of the oxide and patterned and etched into ridge waveguides. These waveguides exhibit tight bend radii (sub-millimeter) but have difficulty coupling to a fiber due to the mode size mismatch.

B.2 Lithium niobate based fabrication

Lithium niobate ($LiNbO_3$) covers a wide spectrum and is transparent from 420nm to 4500nm. Since it is a birefringent material, it has 2 refractive indices, about 2.21 for the ordinary axes and 2.14 for the extraordinary axis at wavelengths near 1.5μm. Although several methods of fabricating waveguides with $LiNbO_3$ exist, the most common is thermal in-diffusion of titanium (Ti). Since the melting point of Ti is 1725^o C, the Ti film is usually deposited with an electron-beam evaporation system or a DC, RF, or magnetron-type RF sputtering system. A waveguide pattern is then created using standard photolithographic techniques followed by etching in a hydrofluoric acid bath or with a reactive ion etching system. Finally, by heating at ~1000^o C, the Ti is diffused into the $LiNbO_3$ substrate [8].

B.3 Arsenic sulphide based fabrication

As_2S_3 is an important material which is transparent from visible to the far infrared (8μm) range. Its refractive index is about 2.4 at wavelengths near 1.5μm. As_2S_3 films are usually deposited by thermal evaporation and laser deposition. Recent work has demonstrated beneficial depositions using magnetron sputtering [11]. Then optical waveguides are fabricated by laser writing, or chemical wet etching or dry etching after patterning [12].

One proposed optical ring resonator structure using As_2S_3 is shown in Fig. 8 [13]. First, light from a laser source is coupled into a Ti-diffused waveguide in a $LiNbO_3$ substrate. Then the light couples vertically to an As_2S_3 ring with a sub millimeter bend radius which has some taper structures to aid in coupling. Finally, the light from the ring

couples back into the Ti-diffused $LiNbO_3$ waveguide, and from the Ti-diffused waveguide into an optical detector. An additional Ti-diffused waveguide is placed on the back side of the ring along with some phase electrodes for refractive index tuning of the entire ring structure. One of the main motivations for using the Ti-diffused $LiNbO_3$ waveguide is that its mode will match the mode of a standard fiber much better than As_2S_3 alone will.

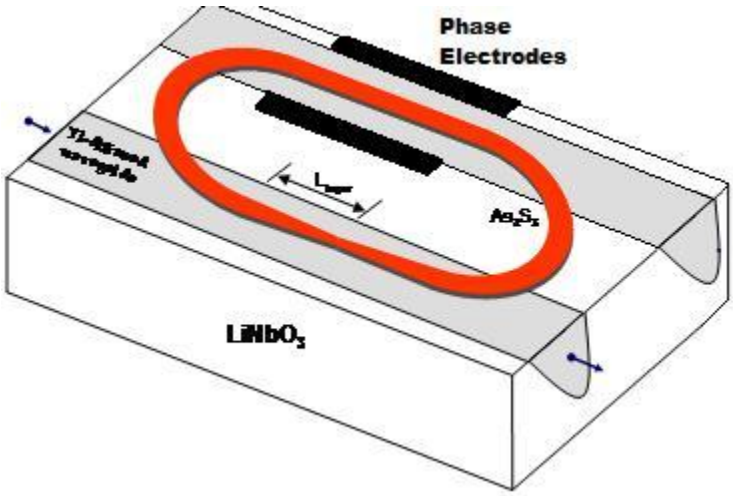

Fig. 8 Schematic of an As_2S_3 ring structure on $LiNbO_3$.

C. Index Changing Effects

As we shall see in the next chapter, slight refractive index changes can cause a significant change to optical device functionality. Dynamic tunability due to refractive index change is a desirable characteristic for devices in many applications. The fact that only slight refractive index changes are needed is very good because most refractive index changing effects are quite small.

C.1 Thermo-optic effect

The thermo-optic effect is one of the larger refractive index controlling mechanisms, and has a value of:

$$\frac{\Delta n}{\Delta T} = 2 \times 10^{-4} \frac{1}{K°} \quad 3.1$$

for Si and:

$$\frac{\Delta n}{\Delta T} = 5.3 \times 10^{-5} \frac{1}{K°} \quad 3.2$$

for $LiNbO_3$ where Δn is the refractive index change and ΔT is the change in temperature [8]. Even a $100\ C°$ change yields a refractive index change of only 5.3×10^{-3} in $LiNbO_3$ and 2×10^{-2} in Si. This is more than sufficient change for most applications though.

The thermo-optic effect usually requires time on the order of milliseconds to complete the refractive index change. This is acceptable for some applications if they don't require high speed transitioning. Regardless of whether an application specifically uses the thermo-optic effect for dynamic tuning or not, good thermal control is important for waveguide device function. Another downside is power consumption since it is a thermal process

C.2 Electro-optic effect

Perhaps the fastest refractive index changing effect studied thus far is the electro-optic effect [8]. It comes in two varieties, the linear or Pockels effect and the second-order or Kerr effect. The Pockels effect is generally found in crystals that lack inversion-symmetry such as $LiNbO_3$ and GaAs, whereas the Kerr effect is generally

found in centrosymmetric crystals such as Si. The Kerr effect in silicon is far too small to be of any use ($\Delta n = 10^{-4}$ for an applied field of 10^6 $\frac{V}{cm}$), but the Pockels effect in $LiNbO_3$ is much larger and allows for Δn of up to 1.6×10^{-3}. Specifically in $LiNbO_3$:

$$\Delta n_o = \frac{1}{2}\,(8.6 \times 10^{-12}\frac{m}{V})n_o^3 E_z \qquad 3.3$$

$$\Delta n_e = \frac{1}{2}\,(30.8 \times 10^{-12}\frac{m}{V})n_e^3 E_z \qquad 3.4$$

for an electric field applied in the z crystal direction (E_z) where Δn_o equals the refractive index change for the ordinary axes (x and y) and Δn_e equals the refractive index change for the extraordinary axis (z). Electro-optically controlled $LiNbO_3$ is the principle technique used in most modern high-speed modulators, and modulations of 40 GHz are common. Therefore switching times can be as low as tens of picoseconds.

D. Fabrication Research

Device level characteristics determined during fabrication heavily influence system level performance. At the system level, these device characteristics are usually lumped into single mathematical terms such as waveguide loss, power coupling constant, etc. At the fabrication level, these terms can be influenced in several ways. For example, waveguide loss can come from tight bend radii, sidewall roughness, waveguide mode profile changes, etc. Each of these characteristics is in turn affected immensely by individual process parameters such as flow rate, temperature, electric field strength, time, solution concentration, and many more.

The remainder of this dissertation will focus on system level design, employing computer simulations and proof-of-concept experiments. Accordingly, device level

characteristics will be lumped into single mathematical terms. Rather than try to forecast specific fabrication parameters that will be important in determining these lumped terms, fabrication tolerances (usually a percentage accuracy requirement) on the different lumped terms will instead be pursued.

CHAPTER IV

SIGNAL PROCESSING OVERVIEW

A. Ring Resonators

Optical ring resonators are one of the simplest optical structures and can be very useful tools for signal processing. A standard optical ring resonator consists of two optical waveguides coupled together where one of the waveguides feeds back on itself, creating a ring structure (see Fig. 9). This feedback structure causes an input optical wave to mix with scaled and delayed replicas of itself. Frequently a second waveguide is coupled to the ring as well for additional functionality.

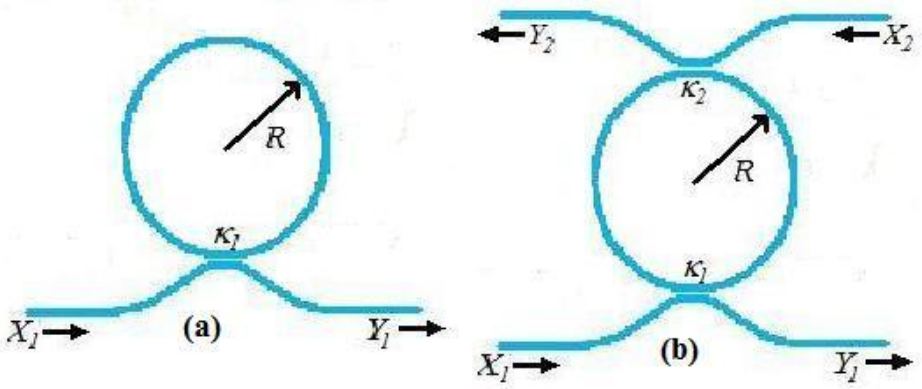

Fig. 9 Simple optical ring resonators with (a) one input and output for all-pass functionality, and (b) two inputs and outputs for add/drop functionality.

A.1 Ring resonator quantification

Ring resonators have three important quantities that determine their response: the power coupling constant κ, the round trip loss factor γ, and the feedback delay time T.

The feedback delay time can be easily calculated from the total round-trip length of the ring as follows:

$$T = \frac{Ln_g}{c} \tag{4.1}$$

where L is the total round trip length, n_g is the group refractive index, and c is the speed of light.

The round-trip loss is important in determining the ring resonator's spectral response as it attenuates the feedback wave. Since waveguide loss is frequently represented as loss per unit length, ring round trip loss is as well. As α is the waveguide loss in dB per unit length, and L is the total round-trip length, αL is the round-trip loss. The normalized amplitude for electric field transmission after one round trip γ becomes:

$$\gamma = 10^{\frac{-\alpha L}{20}} \tag{4.2}$$

In most cases it is desirable to reduce the round trip loss as much as possible.

The power coupling is determined by the optical directional coupler between the ring and straight waveguide (see Fig. 10) where κ is the power coupling in dB, $\cos(\theta)$ is the through port transmission coefficient and $-j\sin(\theta)$ is the cross port transmission coefficient [14].

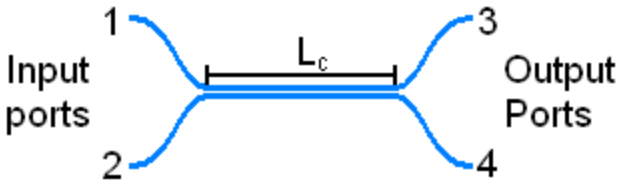

Fig. 10 An optical directional coupler.

The well known equations which describe the input and output electric field of the lossless coupler shown in Fig. 10 are given by:

$$\begin{bmatrix} E_3 \\ E_4 \end{bmatrix} = \begin{bmatrix} \sqrt{1-\kappa} & -j\sqrt{\kappa} \\ -j\sqrt{\kappa} & \sqrt{1-\kappa} \end{bmatrix} \begin{bmatrix} E_1 \\ E_2 \end{bmatrix} \tag{4.3}$$

or:

$$\begin{bmatrix} E_3 \\ E_4 \end{bmatrix} = \begin{bmatrix} \cos(\theta) & -jsin(\theta) \\ -jsin(\theta) & \cos(\theta) \end{bmatrix} \begin{bmatrix} E_1 \\ E_2 \end{bmatrix}. \tag{4.4}$$

The relation between input and output intensity of a lossless symmetrical directional coupler is given by:

$$\begin{bmatrix} I_3 \\ I_4 \end{bmatrix} = \begin{bmatrix} 1-\kappa & \kappa \\ \kappa & 1-\kappa \end{bmatrix} \begin{bmatrix} I_1 \\ I_2 \end{bmatrix}. \tag{4.5}$$

If both waveguides have the same propagation constant which is the case in this configuration and the light is inserted into input port 1, then after a length L_C the energy will have coupled into the other waveguide and can be detected at output port 4.

The coupling behavior dependent on L_C for light inserted at input port 1 is expressed by:

$$E_3(x) = E_1 \cos\left(\frac{\pi}{2L_c}x\right) \tag{4.6}$$

$$E_4(x) = jE_1 \sin\left(\frac{\pi}{2L_c}x\right) \quad 4.7$$

$$I_3(x) = E_3(\mathrm{x})\overline{E_3(\mathrm{x})} \quad 4.8$$

and:

$$I_4(x) = E_4(\mathrm{x})\overline{E_4(\mathrm{x})} \quad 4.9$$

where the bar denotes the complex conjugate.

A.2 Ring resonator model

As will be seen shortly, the amplitude and phase response of an optical ring resonator has a periodic nature in the frequency domain. The spectral size of each repetition is known as the Free Spectral Range (FSR), and can be calculated by taking the inverse of the feedback delay time of the ring:

$$FSR = \frac{1}{T} = \frac{c}{Ln_g}. \quad 4.10$$

This periodic nature is also commonly seen in digital filters. Consequently, ring resonators are often modeled in the z-domain using digital filter theory. This allows for a great deal of digital filter theory to be applied to ring-resonator based filters. It is important to note, though, that no sampling or digitization is taking place; the z-domain is simply a useful representation for optical ring resonators.

We therefore model the ring resonator's response using digital filter theory as a cross-coupled feedback delay line, as shown in Fig. 11 [7]. If we take $z = e^{j\omega T}$ then our output equation for Y_2 becomes:

$$Y_2(z) = -\sin(\theta_1)\sin(\theta_2)\sqrt{\gamma z^{-1}}(1 + \cos(\theta_1)\cos(\theta_2)\gamma z^{-1} + \ldots)X_1(z) \quad 4.11$$

which simplifies to:

$$H_{21}(z) = \frac{Y_2(z)}{X_1(z)} = \frac{-\sin(\theta_1)\sin(\theta_2)\sqrt{\gamma z^{-1}}}{1-\cos(\theta_1)\cos(\theta_2)\gamma z^{-1}}. \quad 4.12$$

Likewise the equation for Y_1 becomes:

$$Y_1(z) = [\cos(\theta_1) - \sin^2(\theta_1)\cos(\theta_2)\gamma z^{-1}(1 + \cos(\theta_1)\cos(\theta_2)\gamma z^{-1} + \ \ldots)]X_1(z) \quad 4.13$$

which simplifies to:

$$H_{11}(z) = \frac{Y_1(z)}{X_1(z)} = \frac{\cos(\theta_1) - \cos(\theta_2)\gamma z^{-1}}{1-\cos(\theta_1)\cos\,(\theta_2)\gamma z^{-1}}. \quad 4.14$$

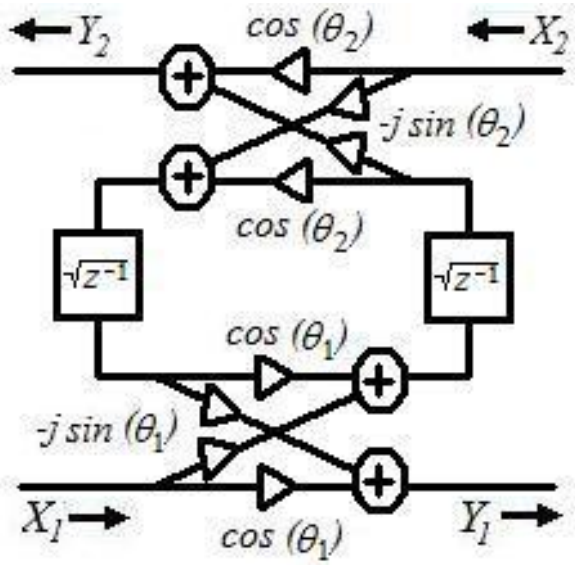

Fig. 11 Z-transform schematic of a ring resonator.

The spectral response follows directly from (4.12) and (4.14). As you can see in Fig. 12, the H_{11} amplitude response (called the through port) behaves like a notch filter and the H_{12} amplitude response (called the cross port) behaves like a band pass filter, allowing the frequencies that the through port filtered out. The width and depth of the notch is a function of the coupling constants (κ_1,κ_2) and the round trip ring loss (αL).

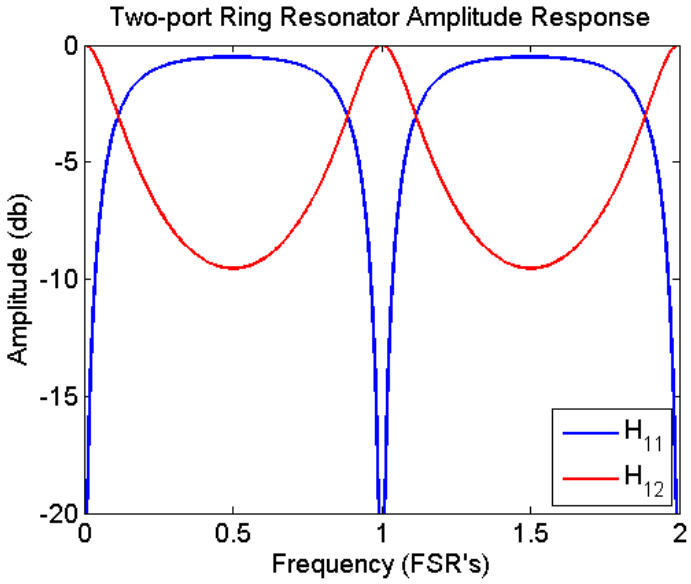

Fig. 12 The amplitude response of an ideal two port ring resonator for $\kappa_1 = \kappa_2 = 0.5$ and $\alpha = 0$.

A.3 Optical all-pass filters

If $\kappa_2 = 0$ and $\gamma = 1$ then there will be no notches and the response will become an all-pass filter. Setting $\kappa_2 = 0$ is equivalent to an optical ring resonator with only one coupling waveguide (see Fig. 9 a). This arrangement of the optical ring resonator is typically called an all-pass filter configuration. The z-domain equation describing its behavior is similar to (4.7) except without θ_2:

$$H_{apf}(z) = \frac{Y_1(z)}{X_1(z)} = \frac{\cos(\theta_1) - \gamma z^{-1}}{1 - \cos(\theta_1)\,\gamma z^{-1}} \qquad 4.15$$

The amplitude response of the optical all-pass filter ($\kappa = 0.5$) is shown in Fig. 13 for various amounts of round-trip loss. Note the first case: if the ring has zero round-trip loss, all frequencies pass equal amplitudes, thus the name all-pass filter.

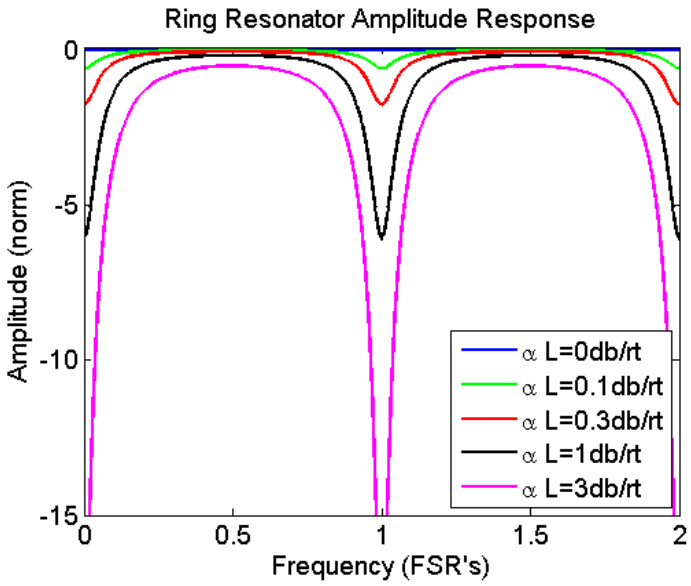

Fig. 13 The amplitude response of an optical ring resonator ($\kappa = 0.5$) in an all-pass configuration with various amounts of round-trip loss.

Also of note is the final case where the round-trip loss $\alpha L = 3\, db/rt$. In this case the normalized round-trip amplitude $\gamma = 0.5$ is equal to the coupling constant. Any case where the normalized round-trip amplitude equals the coupling constant is called the critical coupling condition. For critical coupling the amplitude notch theoretically extends to minus infinity in terms of dB.

A.4 All-pass filter phase and group-delay response

For many applications, the phase response of the filter is of greater interest than the amplitude response. The phase response of a lossless optical ring resonator for various coupling constants is shown in Fig. 14. Clearly the phase response is non-linear, but as will be seen shortly this actually turns out to be beneficial.

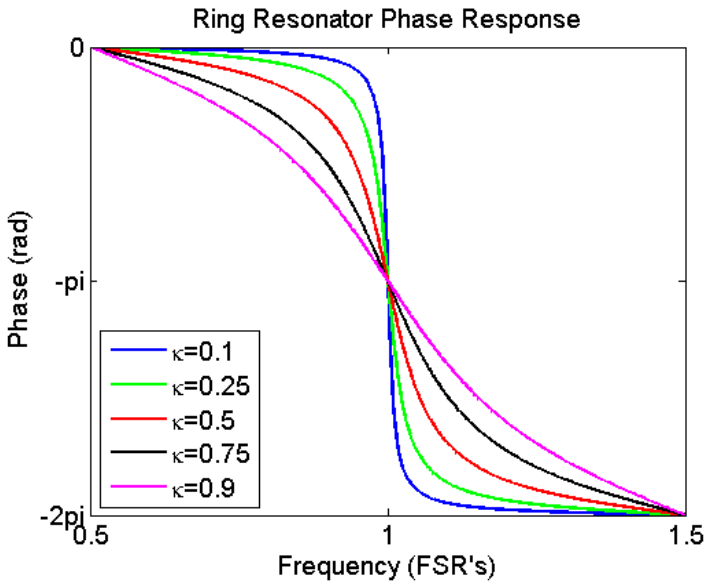

Fig. 14 The phase response of a lossless ring resonator in an all-pass configuration with various coupling constants.

The group delay is defined as the first derivative of the phase with respect to the frequency as follows:

$$T_g = \frac{-\delta\varphi}{\delta\omega} \tag{4.16}$$

where φ can be found by taking only the angle of (4.8). Group delay effectively measures the amount of time different frequencies take to pass the filter; its usual units are picoseconds. The group delay response of a lossless ring resonator in an all-pass configuration for various coupling constants is shown in Fig. 15. This clarifies why many digital filters are required to be linear phase; the derivative of a linear phase is a constant group delay. Optical filters with variable group delay are quite useful though as will be seen in subsequent chapters.

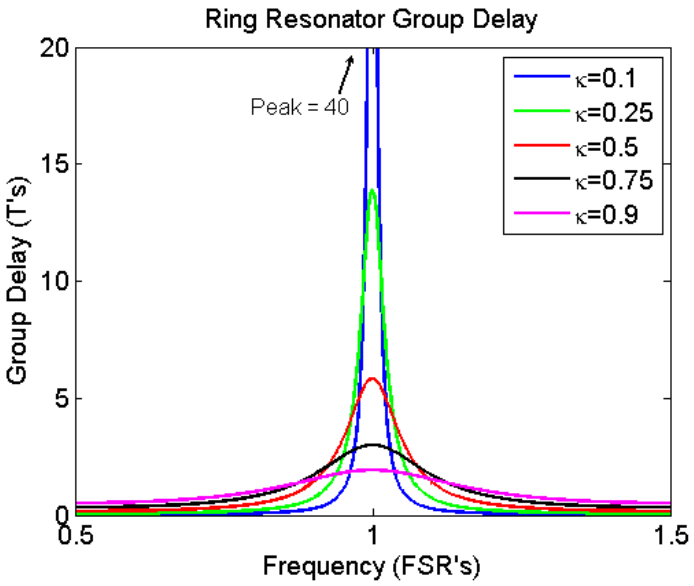

Fig. 15 The group delay response of a lossless ring resonator in an all-pass configuration with various coupling constants.

A.5 All-pass filter round trip phase variations

The phase of the optical wave upon completing a round-trip is clearly related to the round trip time T. Hence very small changes in the round-trip time can greatly affect the phase of the optical wave upon completing a round trip. This in turn will shift the phase and group delay response along the frequency axis. In the z-domain equation for the all-pass filter, phase changes come on the z term, aka:

$$z^{-1} \rightarrow e^{j\varphi} z^{-1} \qquad 4.17$$

Figs. 16 and 17 show a lossless ring with a coupling constant $\kappa = 0.5$ and various phase shifts

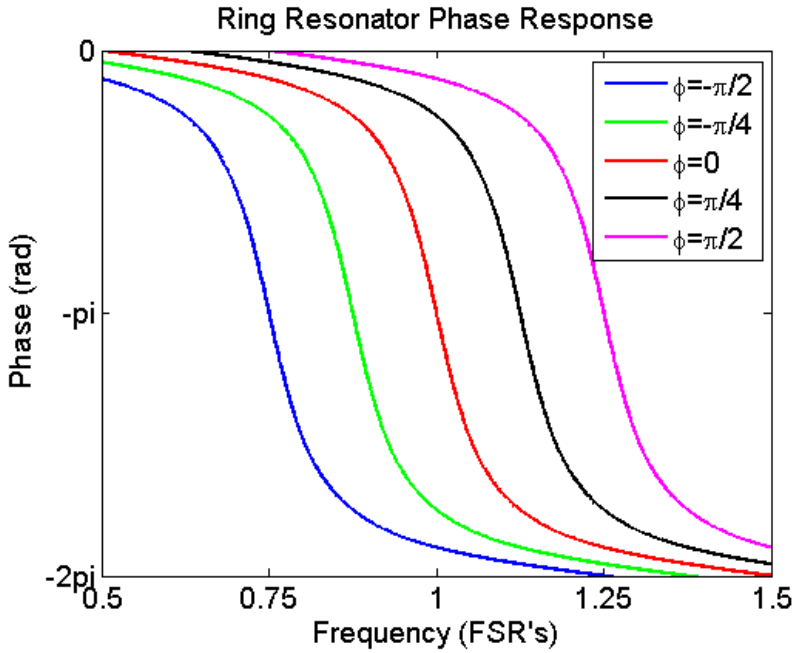

Fig. 16 The phase response of a lossless ring resonator in an all-pass configuration with a coupling constant $\kappa = 0.5$ and various round trip phase offsets.

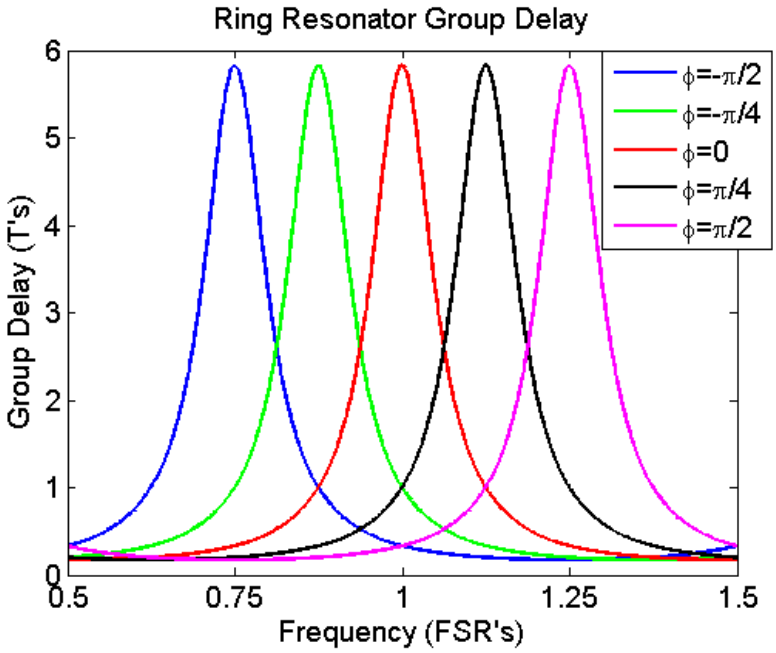

Fig. 17 The group delay response of a lossless ring resonator in an all-pass configuration with a coupling constant $\kappa = 0.5$ and various round trip phase offsets.

B. Dynamic Tunability

Dynamic tunability is a desirable characteristic for filters in many applications. It allows for adaptive filtering, time-frequency domain filtering, and a great many other signal processing capabilities. Optical ring-resonator based filters are no different, dynamic tunability is very useful particularly with regard to all-pass phase filters. Besides the application benefits, dynamic tunability also improves fabrication tolerances.

Dynamic tuning is generally sought after in the feedback delay time T and the power coupling constant κ. Optical losses that determine the round trip loss factor are generally undesirable and minimized as much as possible. While integrated optical ring resonators with dynamic gain have been demonstrated, this gain is usually introduced either to minimize round-trip loss or create some sort of lasing effect [15]-[17].

As will be seen in the chapters to follow, a cascade of integrated optical ring resonators with dynamically tunable coupling and phase responses can approximate a wide variety of group-delay and/or phase responses.

B.1 Dynamic tuning of the ring round-trip phase

Surprisingly little change is needed in the ring waveguide's refractive index to create a significant change in the spectral response. Although according to (4.10) the refractive index of a ring resonator is inversely proportional to the FSR of the ring, the larger effect is a change in the round-trip phase of the optical wave. This round-trip phase change leads to a spectral shift of the ring response:

$$\Delta\lambda = \lambda \frac{\Delta n_g}{n_g} \qquad 4.18$$

$$\Delta f = f\left(\frac{n_g}{n_g + \Delta n_g} - 1\right) \tag{4.19}$$

or if Δn_g is small:

$$\Delta f \approx -f\frac{\Delta n_g}{n_g} \tag{4.20}$$

where $\Delta n_g \approx \Delta n_e$. Therefore a small Δn_g will lead to a Δf that is a large portion of the FSR of a ring response. This effect can be seen in Figs. 18 and 19.

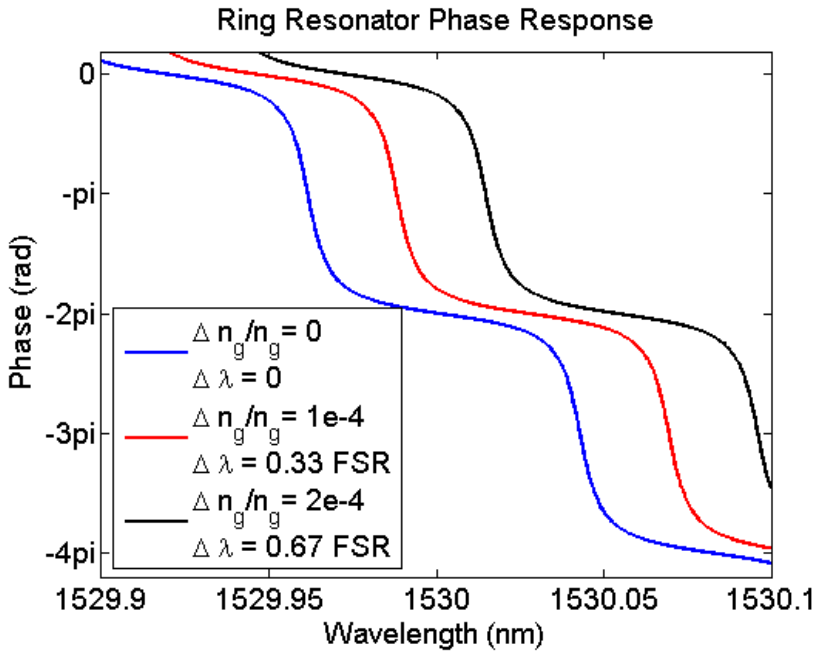

Fig. 18 Phase response of an integrated optical ring resonator with various refractive index shifts.

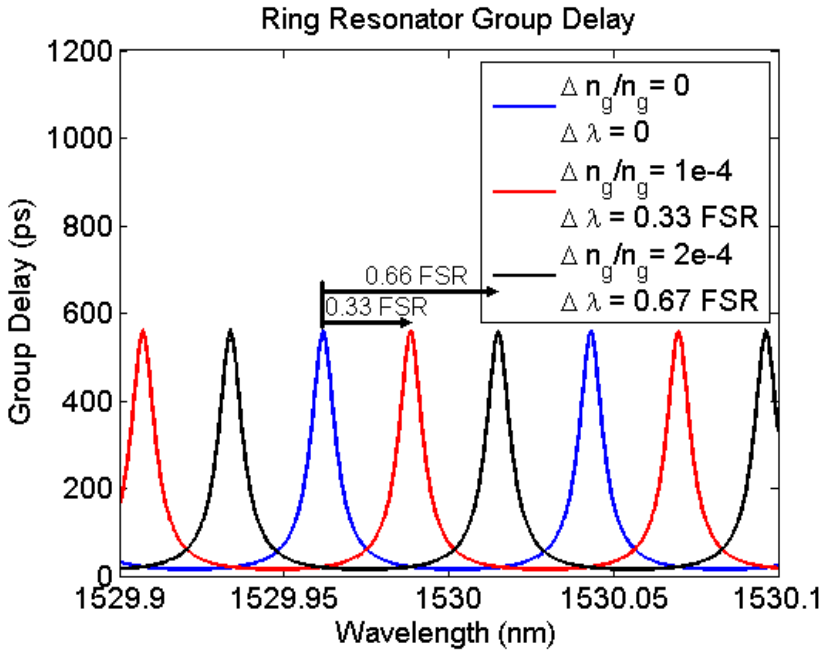

Fig. 19 Group delay response of an integrated optical ring resonator with various refractive index shifts.

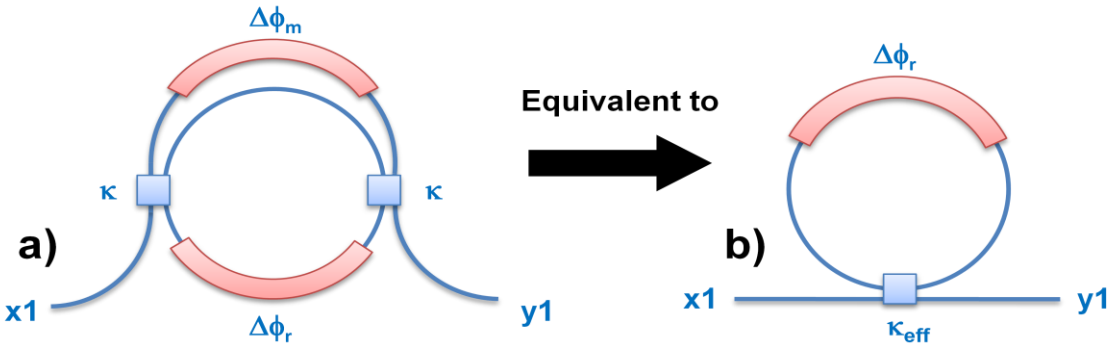

Fig. 20 a) Mach-Zehnder embedded integrated optical ring resonator in an all-pass configuration. b) Equivalent all-pass configuration with a tunable coupler.

B.2 Dynamic tuning of the ring coupling constant

Direct tuning of the power coupling constant of an integrated optical ring resonator has been shown using thermal effects [14]. This method is a bit unwieldy for most applications though.

A much more elegant way of accomplishing the same effect in all pass filters has been shown by embedding the integrated optical ring resonator within a Mach-Zehnder interferometer (see Fig. 20) [18]. The Mach-Zehnder interferometer embedded ring design enables a tunable APF by incorporating phase shifters in the ring and the Mach-Zehnder reference path. The phase shifter in the Mach-Zehnder reference path (φ_m) enables a tunable coupling ratio while the phase shifter in the ring resonator (φ_r) is for resonance tuning. The effective coupling is given by:

$$\kappa_{eff} = 4\kappa(1-\kappa)\cos^2\left(\frac{\frac{2\pi n_g \Delta L}{\lambda} + \Delta\varphi_m}{2}\right) \qquad 4.21$$

where κ is the individual coupling ratios, ΔL is the path length difference between the Mach-Zehnder paths, λ is the input optical wavelength, and $\Delta\varphi_m$ is the induced phase change in the Mach-Zehnder reference path. Because of the slight length difference between the two Mach-Zehnder paths, slight wavelength dependence will develop in κ_{eff}. A full range of $\kappa_{eff} = 0\ to\ 1$ can be achieved only when κ=0.5. Figs 21 and 22 show the phase and group delay response of the Mach-Zehnder interferometer embedded all-pass filter for a variety of values of κ_{eff}. $\Delta\varphi_m$ can be calculated as follows:

$$\Delta\varphi_{\mathrm{m}} = \frac{L_{ref}\,\Delta n_g}{\lambda} \qquad 4.22$$

where L_{ref} is the length of the MZI reference path, and Δn_g is the refractive index change.

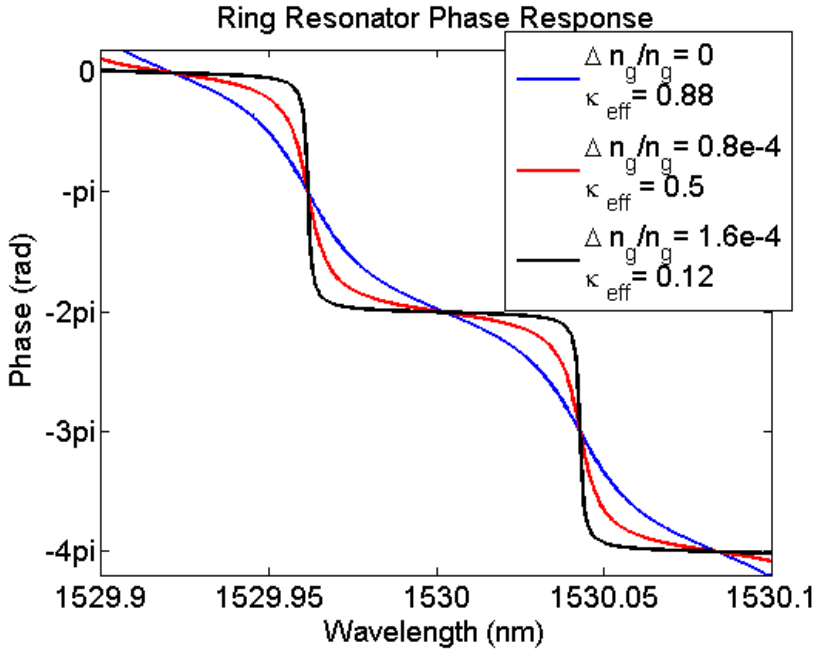

Fig. 21 Phase response of a Mach-Zehnder embedded integrated optical ring resonator with various refractive index shifts on the reference path.

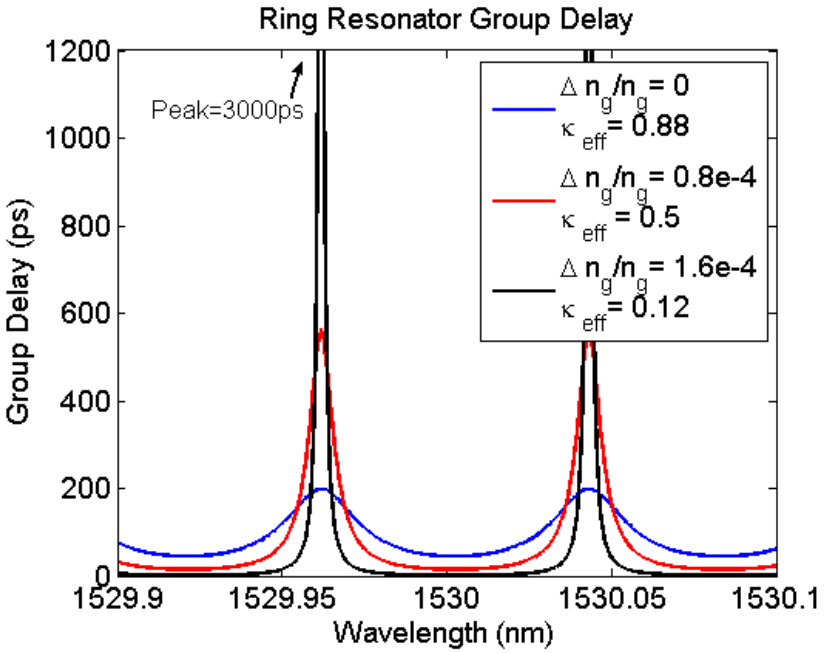

Fig. 22 Group delay response of a Mach-Zehnder embedded integrated optical ring resonator (T = 96 ps, FSR = 10.4 GHz)with various refractive index shifts on the reference path.

CHAPTER V

SPECTRAL MEASUREMENT SYSTEMS

A. Importance of Accurate Measurements

Accurate measurements are arguably the most important part of any engineering endeavor. Certainly accurate measurements are needed at every level of integrated optical research; from fabrication process parameters all the way to system level performance.

Correct estimation of integrated optical ring resonator parameters (round trip loss, coupling constant(s), and spectral phase offset) requires an accurate measurement of both the spectral amplitude response and the spectral phase response. Additionally, ring parameters may vary for TE and TM polarizations; so an accurate measure of the parameters for both polarizations is usually required as well.

Most commercially available optical measurement systems have been designed for fiber optic communication systems. Frequently, these systems do not have the bandwidth or polarization requirements needed for measuring integrated optical waveguides. Therefore, system adaptation is usually required.

This chapter covers four such measurement systems: the coherent optical spectrum analyzer, the group delay measurement system, the polarization dependent amplitude measurement system, and the interferometric Jones matrix measurement system. The coherent optical spectrum analyzer and the group delay measurement system were created in the lab from various off-the-shelf components. By contrast the polarization dependent amplitude measurement system and the interferometric Jones

matrix measurement system were complete measurement systems that merely were adapted to integrated optical waveguide measurement.

B. Coherent Optical Spectrum Analyzer

Traditionally, optical spectrum analysis is done with grating-based optical spectrum analyzers (OSA's). The basic principle is shown in Fig. 23. Incoming light is reflected off of an optical diffraction grating which reflects light at different angles based upon wavelength. The diffraction grating itself is rotated with respect to the incoming light source such that a photodetector with a fixed position and detection area will sequentially detect each wavelength.

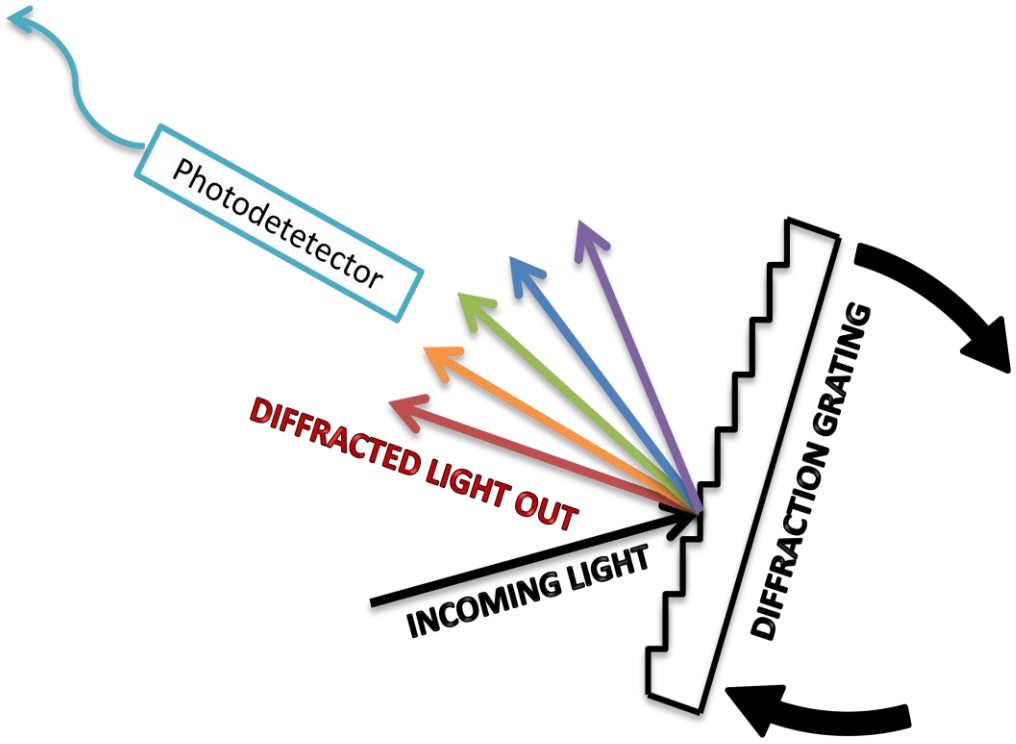

Fig. 23 Grating based OSA basic operation diagram.

Grating based OSA's are very common and useful optical measurement systems. Typical systems can exhibit wavelength resolutions of as low as 0.07 nm (~10 GHz at 1500nm).

For some applications, optical spectrum analysis is desired at much tighter wavelength resolutions. To accomplish this with grating based OSA's would require very large optical components, quickly making the system unwieldy.

In contrast to grating based OSA's, recently it has been proposed to use a swept laser source in combination with a coherent detection system to perform optical spectrum analysis [19]–[20]. This system is known as the coherent optical spectrum analyzer (COSA), and the basic diagram of the system can be seen in Fig. 24.

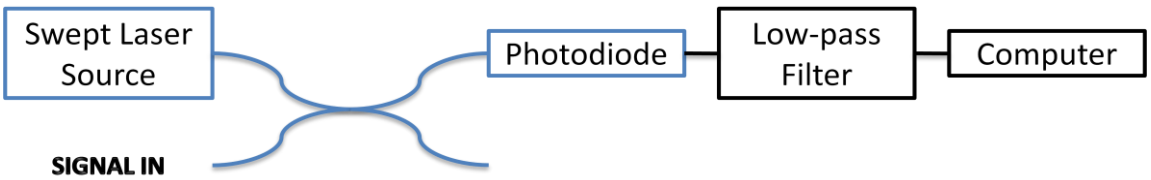

Fig. 24 Coherent optical spectrum analyzer block diagram.

The input optical signal is mixed with the swept laser source in an optical coupler (fiber-optic coupler usually), then the output is photodetected and filtered to the desired bandwidth. Interestingly, if the linewidth of the swept laser source and input signal is significantly less than the low-pass filter bandwidth, the resulting waveform exhibits clear chirping, whereas if the low-pass filter bandwidth is smaller the waveform is more chaotic (see Fig. 25)

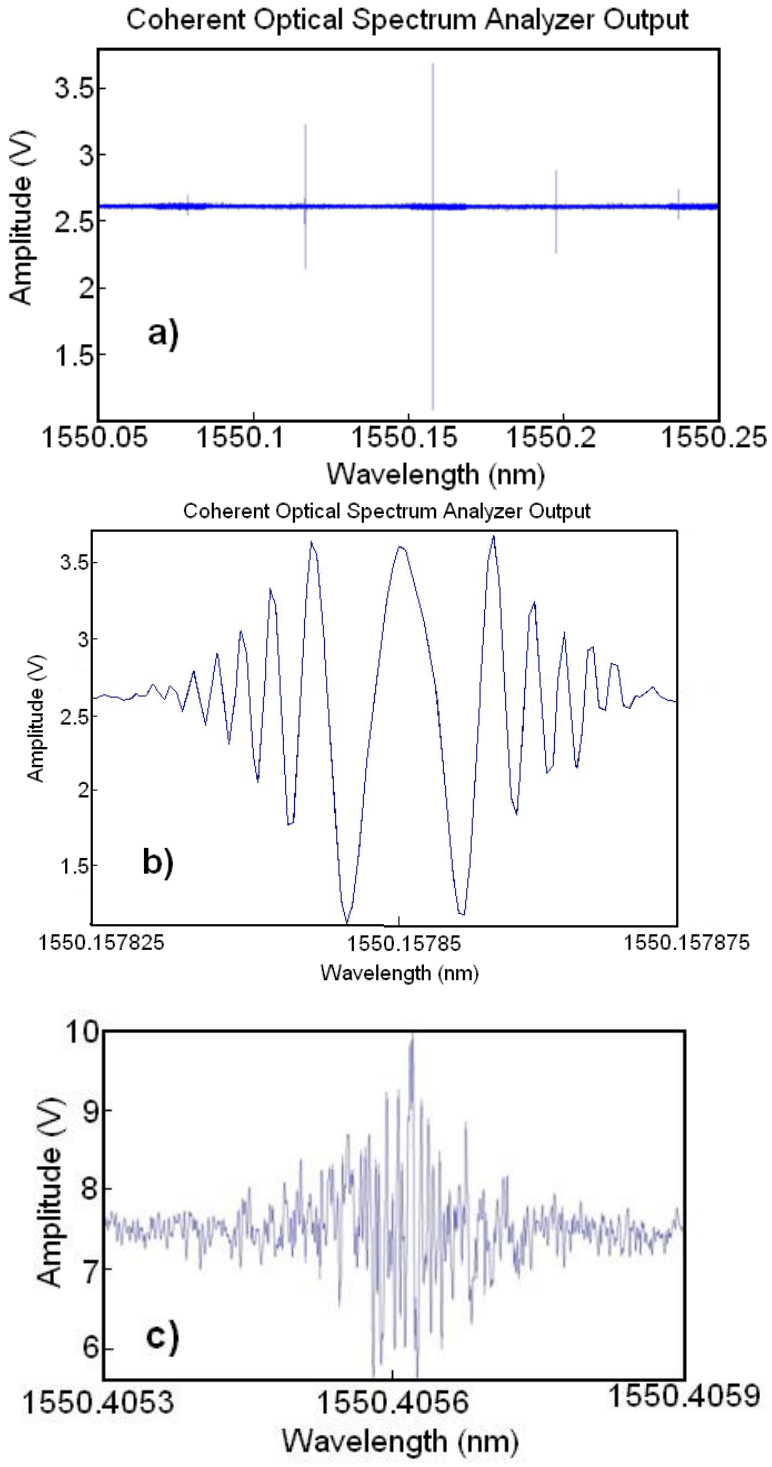

Fig. 25 Coherent optical spectrum analyzer output: a) wideband view, b) narrowband view for small linewidth lasers, c) narrowband view for large line-width lasers.

In the case shown in Fig. 25, a 5 MHz low-pass filter was used, the swept laser has a linewidth of 100-300 kHz, and the optical inputs had linewidths of 500 kHz and 25 MHz.

There were two or three issues that had to be solved in order to get accurate measurements. First, the polarization of both waves must be matched prior to mixing in the coupler. This was accomplished with a couple of paddle-style fiber polarizers.

Second, the sweeping laser didn't always exhibit a perfectly constant sweep speed; slight variations in sweep speed would cause small misalignments of the optical spectrum. This was remedied by splitting off a small portion of the swept laser and passing it through an all-fiber Mach-Zehnder interferometer and photodetector. Changes in optical frequency lead to changes in phase between the two arms of the Mach-Zehnder interferometer, which leads to changes in the output optical magnitude seen by the photodetector. Therefore the frequency change could be tracked and small variations in the sweep speed compensated for.

The third issue facing the COSA was the nature of the output. This is most easily seen in the chirp-like outputs (see Fig. 25 b). The magnitude of the optical signal is actually related to the envelope of the chirp, not the chirp itself. This can readily be accounted for in computer software. One caveat though is that if the sweep speed of the laser is too great for the sampling speed of the system (10Msps in this case) the envelope may not be fully shown. In other words there may not be enough cycles of chirp to adequately compute the chirp envelope.

As will be seen in the following chapters, the COSA became one of the principle measurements while setting up other more complex systems.

C. Group Delay Measurement System

The basic principle behind the group delay measurement system is the well-known modulation phase shift technique [21]-[22]. The basic setup is shown in Fig. 26. In operation, the output of a narrowband, tunable optical source is intensity modulated and applied to the device under test. The transmitted signal is detected and the phase of its modulation is measured relative to the electrical modulation source. The phase measurement is repeated at intervals across the wavelength range of interest.

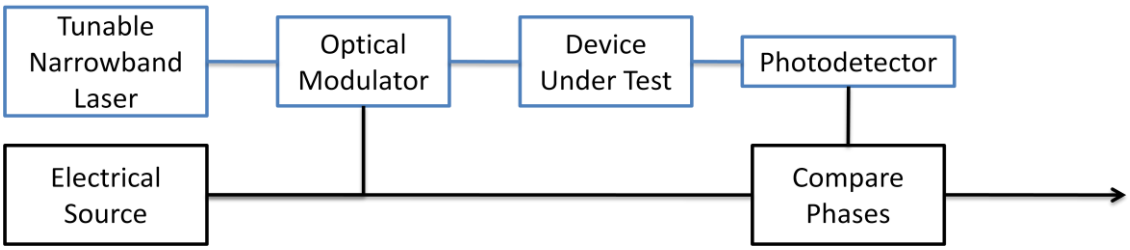

Fig. 26 Basic setup of modulation phase-shift based group delay measurement system.

Unfortunately, the modulation phase shift technique suffers from a fundamental tradeoff of modulation frequency versus resolution. Integrated optical ring resonators are particularly difficult to characterize because of the narrow spectral response. The problem with narrow spectral features in the device under test and large modulation frequencies is that the double sideband (DSB) modulation from an intensity modulator

washes out the narrow features by mixing the upper and lower sidebands to produce the detected radio frequency (RF) phase. (See Fig. 27.)

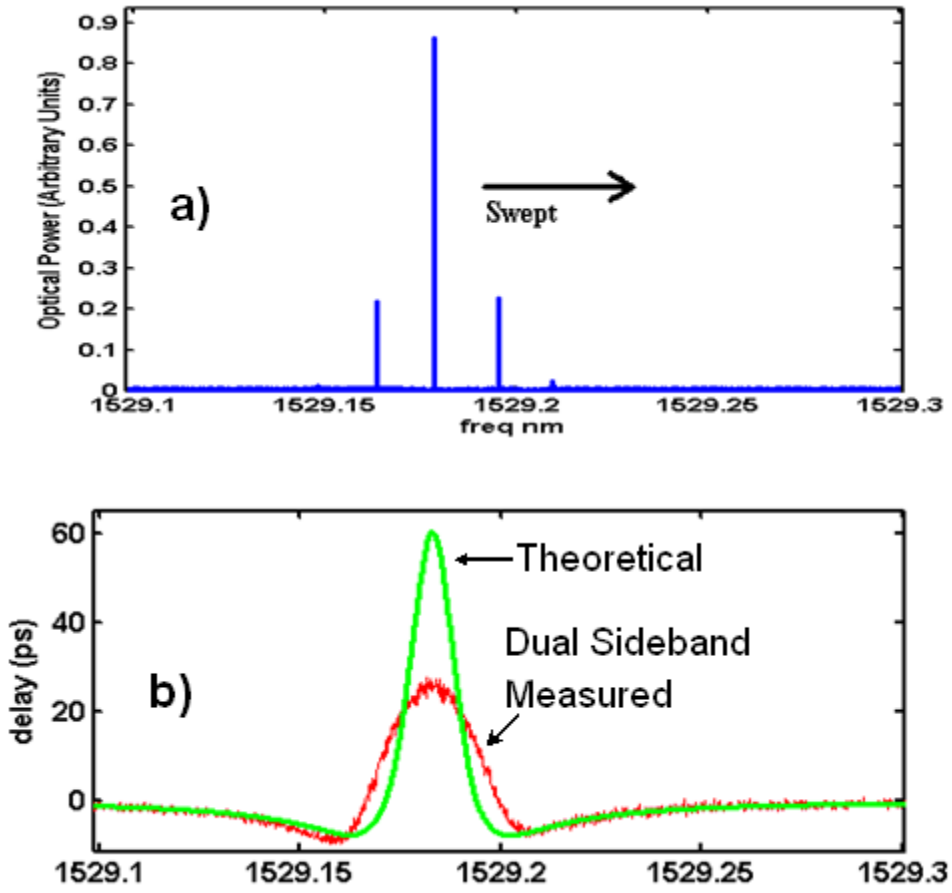

Fig. 27 Basic modulation phase-shift technique. a) Amplitude spectrum of dual sideband modulated swept signal. b) Theoretical vs. measured group delay.

In contrast, if the optical input to the device under test were modulated such that it only had one sideband, the measured group delay would more closely match the actual group delay (See fig 28).

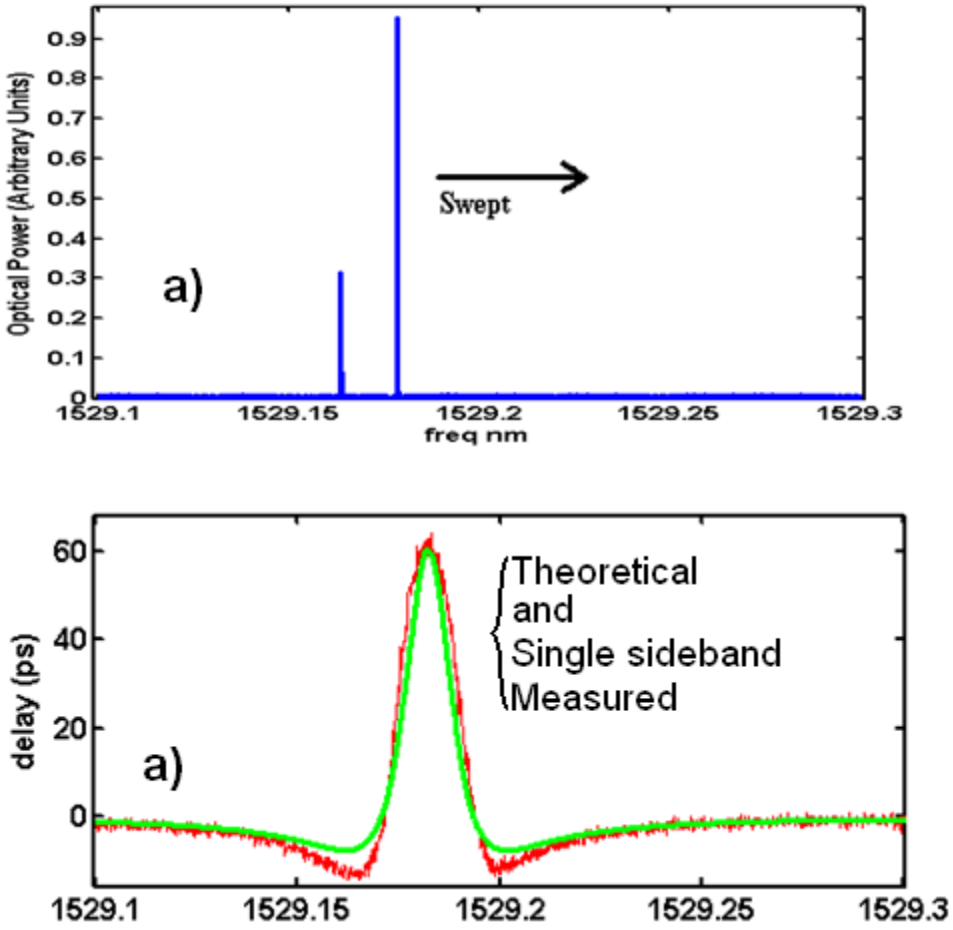

Fig. 28 Single sideband modulation phase-shift technique. a) Amplitude spectrum of single sideband modulated swept signal. b) Theoretical vs. measured group delay.

To achieve this result a Mach-Zehnder dual drive modulator was used instead of a pure optical intensity modulator. The complete experimental setup is shown in Fig. 29, and consists of a swept-wavelength source, a dual-drive modulator, a polarization controller, the device-under-test and a detector with a 3GHz bandwidth. By shifting the phase of one electrical input by 90 degrees relative to the other single sideband modulation is achieved. The detected signal is mixed with the RF modulating signal that

has been offset in frequency, and both the mixer output and the offset frequency are digitized.

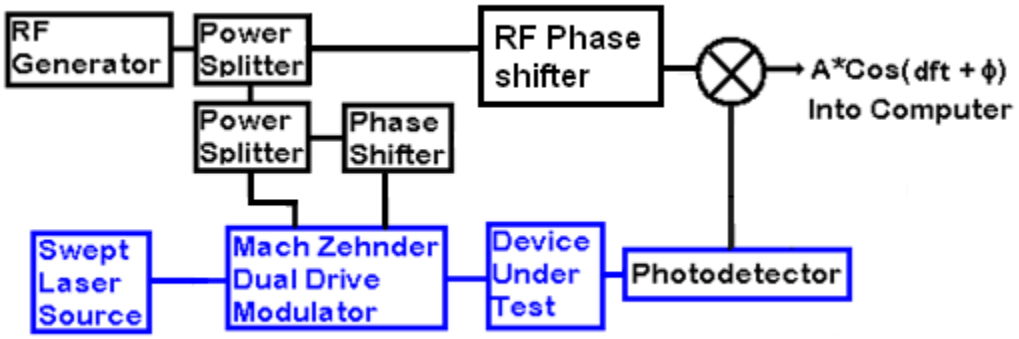

Fig. 29 Single sideband modulation phase-shift based group delay system.

Several measurements were taken on each of 3 different absorption peaks of an acetylene gas cell. The measurements were then averaged to obtain an estimate of accuracy and repeatability, and the results can be seen in Fig 30. The maximum group delay measured with a dual sideband optical modulation was less than 50% of the theoretical max; whereas the maximum group delay measured with a single sideband optical modulation was just over 100%. The width of the group delay peak using the single sideband optical modulation was still 30 % larger than theory predicts, but vastly better than the double width exhibited by the dual sideband measurement.

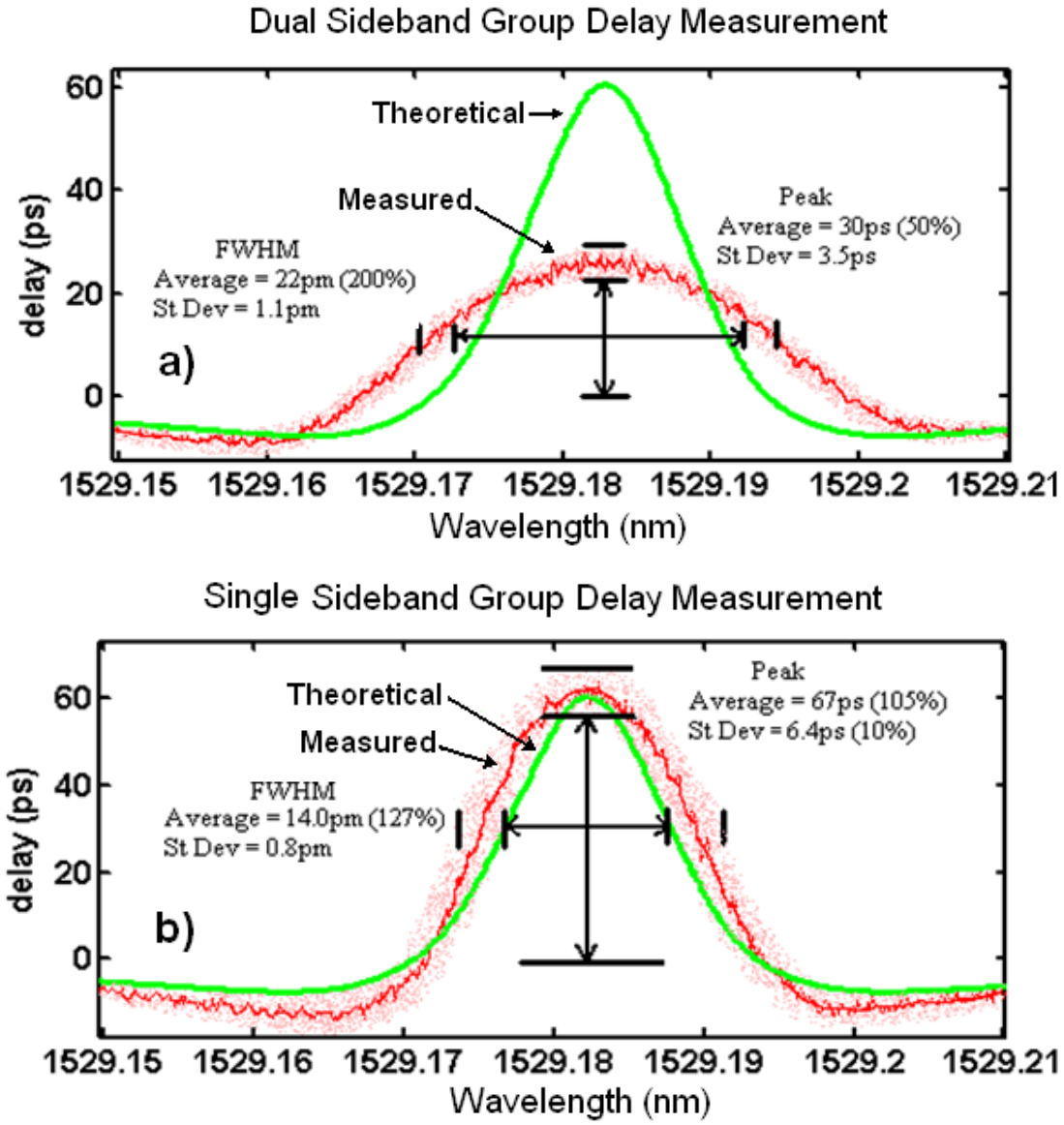

Fig. 30 a) Dual sideband group delay measurement of an acetylene gas cell and b) single sideband group delay measurement of an acetylene gas cell; both vs. theoretical curves.

D. Polarization Dependent Amplitude Measurement System

Most integrated optical waveguides, in a ring configuration or not, exhibit significantly different spectral amplitude responses for their TE and TM polarizations. In many cases, integrated optical ring resonators only function for one polarization. Therefore, complete characterization of a waveguide's amplitude response must include both polarizations.

The simplest method to measure the spectral amplitude response for both polarizations is to manually tune the polarization input to the waveguide to match one response or the other, then to sweep the wavelength spectrum and detect the output amplitude (see Fig. 31).

Due to the polarization rotating nature of fiber, a calibration step must be performed prior to measurement to ensure true TE or TM transmission into the device under test (DUT). This is done by placing a polarizer with a known orientation (TE or TM) in the place of the DUT and tuning the polarizer (POL), quarter-wave plate (QHP), and half-wave plate (HWP) such that the optical amplitude at the photodetector is maximum or minimum. A common measurement is shown in Fig. 32.

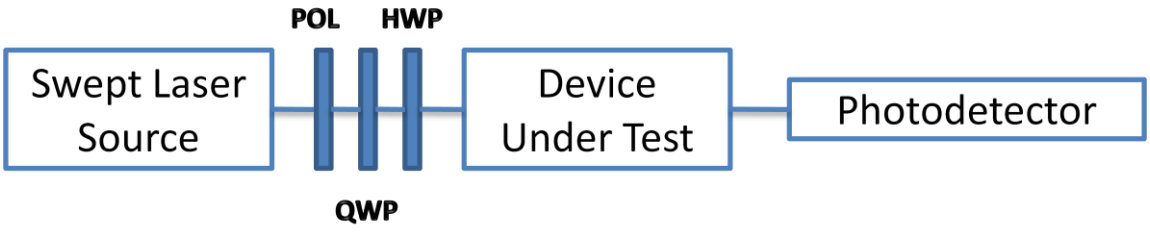

Fig. 31 Polarization dependent amplitude measurement setup.

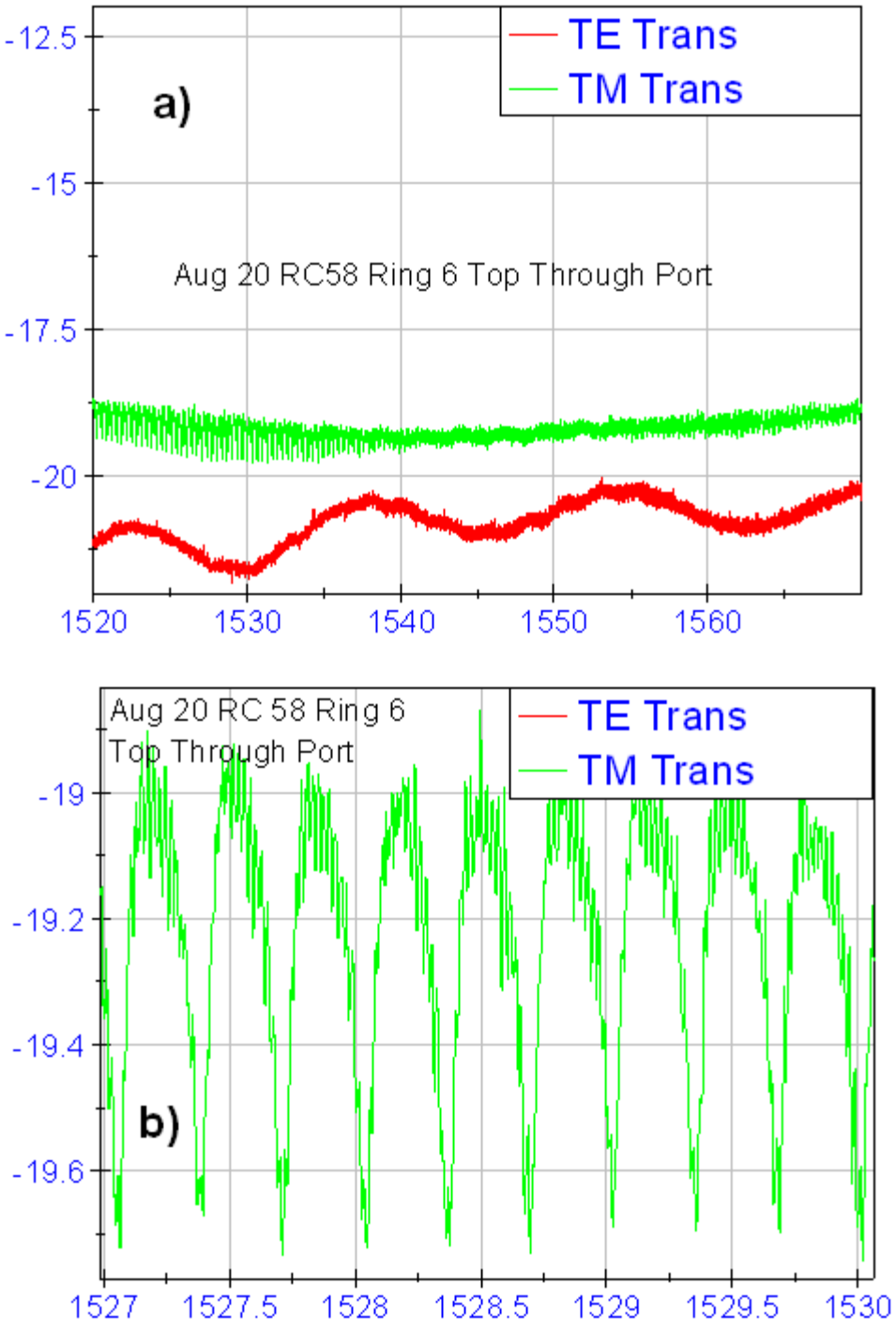

Fig. 32 A common measurement taken by the polarization dependent amplitude measurement system. a) Full spectrum. b) Zoom on TM ring response.

E. Interferometric Jones Matrix Measurement System

In contrast to a simple amplitude measurement of the DUT with TE and TM inputs, a better measurement would be to have the entire complex Jones matrix across the entire wavelength spectrum. Jones matrices stemmed out of Jones vectors: a representation of the electric field of an optical wave as a two element vector:

$$\begin{bmatrix} E_x e^{j\varphi_x} \\ E_y e^{j\varphi_y} \end{bmatrix}. \tag{5.1}$$

Each element in the vector doesn't necessarily need to lie on a principle axis (x or y) or even be a linear polarization, but the two elements must be orthogonal to one another. Whereas a Jones vector represents the electric field of an optical wave, a Jones matrix represents a device that changes the amplitude, phase, and polarization of an optical wave:

$$\begin{bmatrix} E_{xx} e^{j\varphi_{xx}} & E_{yx} e^{j\varphi_{yx}} \\ E_{xy} e^{j\varphi_{xy}} & E_{yy} e^{j\varphi_{yy}} \end{bmatrix}. \tag{5.2}$$

Here xx terms represent the x-polarized output amplitude and phase due to x-polarized inputs, yx terms represent the x-polarized output amplitude and phase due to y-polarized inputs, and so forth. Once again, these terms need not necessarily lie upon a principle axis (x or y) or even be a linear polarization of light, but they must be orthogonal to one another.

This measurement can be done with an interferometric Jones matrix measurement system, also known as an optical vector analyzer (OVA). The specific details of how the interferometric Jones matrix measurement system works is beyond the scope of this dissertation [23]. The setup of the OVA can be seen in Fig. 33.

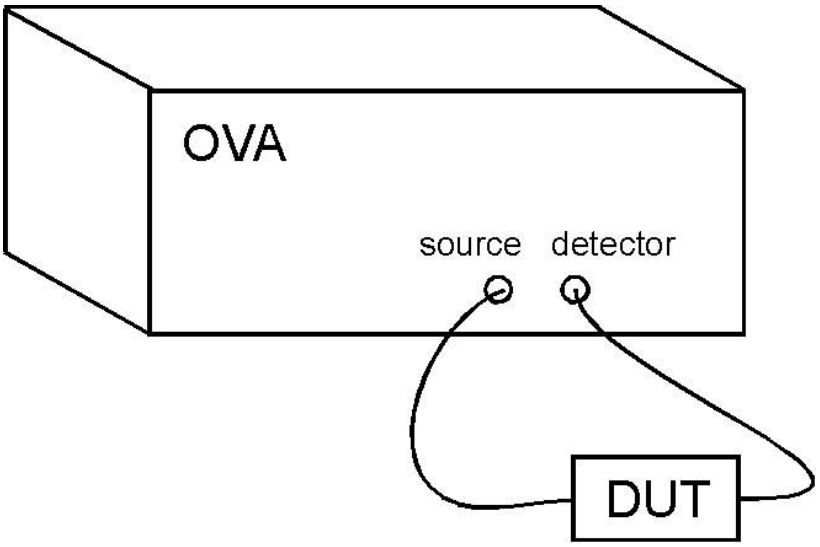

Fig. 33 Optical vector analyzer measurement setup.

One interesting issue with the OVA measurement setup is the effect of the fibers on the final measurement. Lossless fibers behave as arbitrary rotations to the Jones matrix. In addition, fibers generally exhibit a small amount of birefringence as well. Written in Jones matrix form our measurement becomes:

$$\begin{bmatrix} A & B \\ C & D \end{bmatrix} = \begin{bmatrix} \cos(\theta_d)\, e^{j\varphi_d} & -\sin(\theta_d)\, e^{j\gamma_d} \\ \sin(\theta_d)\, e^{-j\gamma_d} & \cos(\theta_d)\, e^{-j\varphi_d} \end{bmatrix} \begin{bmatrix} TE & MxE \\ ExM & TM \end{bmatrix} \begin{bmatrix} \cos(\theta_s)\, e^{j\varphi_s} & \sin(\theta_s)\, e^{-j\gamma_s} \\ -\sin(\theta_s)\, e^{j\gamma_s} & \cos(\theta_s)\, e^{-j\varphi_s} \end{bmatrix} \quad 5.3$$

where TE represents the TE input to TE output response, TM represents the TM input to TM output response, MxE and ExM represent the TM input to TE output and TE input to TM output response respectively, θ_d represents the angle of rotation due to the detector side fiber, θ_s represents the angle of rotation due to the source side fiber, φ_d,

$\gamma_d, \varphi_s, \gamma_s$ all represent birefringence terms, and A B C and D represent actual measured complex values.

There are a few different ways to correct for this fiber rotation; the first and easiest one involves use of a tunable polarizer [24]. We can establish a known reference frame by inserting a polarizer as the DUT, and then measuring the response of the system. If we represent the system in vertical and horizontal components, a horizontal polarizer looks like:

$$\begin{bmatrix} \sin(\theta_d)\, e^{j\varphi_d} & -\cos(\theta_d)\, e^{j\gamma_d} \\ \cos(\theta_d)\, e^{-j\gamma_d} & \sin(\theta_d)\, e^{-j\varphi_d} \end{bmatrix} \begin{bmatrix} 1 & 0 \\ 0 & 0 \end{bmatrix} \begin{bmatrix} \sin(\theta_s)\, e^{j\varphi_s} & \cos(\theta_s)\, e^{-j\gamma_s} \\ -\cos(\theta_s)\, e^{j\gamma_s} & \sin(\theta_s)\, e^{-j\varphi_s} \end{bmatrix}. \quad 5.4$$

Multiply the source (input) matrix by the polarizer to get:

$$\begin{bmatrix} \sin(\theta_d)\, e^{j\varphi_d} & -\cos(\theta_d)\, e^{j\gamma_d} \\ \cos(\theta_d)\, e^{-j\gamma_d} & \sin(\theta_d)\, e^{-j\varphi_d} \end{bmatrix} \begin{bmatrix} \sin(\theta_s)\, e^{j\varphi_s} & \cos(\theta_s)\, e^{-j\gamma_s} \\ 0 & 0 \end{bmatrix} \quad 5.5$$

and then multiply by the detector matrix, giving:

$$\begin{bmatrix} \sin(\theta_d)\sin(\theta_s)\, e^{j(\varphi_d+\varphi_s)} & \sin(\theta_d)\cos(\theta_s)\, e^{j(\varphi_d-\gamma_s)} \\ \cos(\theta_d)\sin(\theta_s)\, e^{-j(\gamma_d-\varphi_s)} & \cos(\theta_d)\cos(\theta_s)\, e^{-j(\gamma_d+\gamma_s)} \end{bmatrix} = \begin{bmatrix} m_{11} & m_{12} \\ m_{21} & m_{22} \end{bmatrix}. \quad 5.6$$

We can then determine some of the quantities associated with the transfer matrices. Taking ratios of the matrix entries, we find:

$$\frac{m_{11}}{m_{21}} = \frac{\sin(\theta_d)\sin(\theta_s)\, e^{j(\varphi_d+\varphi_s)}}{\cos(\theta_d)\sin(\theta_s)\, e^{-j(\gamma_d-\varphi_s)}} = \tan(\theta_d) e^{j(\varphi_d+\gamma_d)} \quad 5.7$$

and:

$$\frac{m_{11}}{m_{12}} = \frac{\sin(\theta_d)\sin(\theta_s)\, e^{j(\varphi_d+\varphi_s)}}{\sin(\theta_d)\cos(\theta_s)\, e^{j(\varphi_d-\gamma_s)}} = \tan(\theta_s)\, e^{j(\varphi_s-\gamma_s)}. \quad 5.8$$

We can then find the values for the rotation angles to be:

$$\theta_d = \arctan\left|\frac{m_{11}}{m_{21}}\right| \tag{5.9}$$

and:

$$\theta_d = \arctan\left|\frac{m_{11}}{m_{12}}\right|. \tag{5.10}$$

We can then construct two translation matrices:

$$T_d = \begin{bmatrix} \sin\left(arctan\left|\frac{m_{11}}{m_{21}}\right|\right)e^{j*angle\left(\frac{m_{11}}{m_{21}}\right)} & \cos\left(arctan\left|\frac{m_{11}}{m_{21}}\right|\right)e^{2j*angle\left(\frac{m_{11}}{m_{21}}\right)} \\ -\cos\left(arctan\left|\frac{m_{11}}{m_{21}}\right|\right)e^{-2j*angle\left(\frac{m_{11}}{m_{21}}\right)} & \sin\left(arctan\left|\frac{m_{11}}{m_{21}}\right|\right)e^{-j*angle\left(\frac{m_{11}}{m_{21}}\right)} \end{bmatrix} \tag{5.11}$$

$$T_d = \begin{bmatrix} \sin(\theta_d)e^{j(\varphi_d-\gamma_d)} & \cos(\theta_d)e^{2j(\varphi_d-\gamma_d)} \\ -\cos(\theta_d)e^{-2j(\varphi_d-\gamma_d)} & \sin(\theta_d)e^{-j(\varphi_d-\gamma_d)} \end{bmatrix} \tag{5.12}$$

and:

$$T_s = \begin{bmatrix} \sin\left(arctan\left|\frac{m_{11}}{m_{12}}\right|\right)e^{j*angle\left(\frac{m_{11}}{m_{12}}\right)} & \cos\left(arctan\left|\frac{m_{11}}{m_{12}}\right|\right)e^{2j*angle\left(\frac{m_{11}}{m_{12}}\right)} \\ -\cos\left(arctan\left|\frac{m_{11}}{m_{12}}\right|\right)e^{-2j*angle\left(\frac{m_{11}}{m_{12}}\right)} & \sin\left(arctan\left|\frac{m_{11}}{m_{12}}\right|\right)e^{-j*angle\left(\frac{m_{11}}{m_{12}}\right)} \end{bmatrix} \tag{5.13}$$

$$T_s = \begin{bmatrix} \sin(\theta_s)e^{j(\varphi_s-\gamma_s)} & -\cos(\theta_s)e^{2j(\varphi_s-\gamma_s)} \\ \cos(\theta_s)e^{-2j(\varphi_s-\gamma_s)} & \sin(\theta_s)e^{-j(\varphi_s-\gamma_s)} \end{bmatrix}. \tag{5.14}$$

Multiplying these constructed correction matrices by the arbitrary source and detector matrices gives:

$$\begin{bmatrix} \sin(\theta_d)\, e^{j(\varphi_d-\gamma_d)} & \cos(\theta_d)\, e^{2j(\varphi_d-\gamma_d)} \\ -\cos(\theta_d)\, e^{-2j(\varphi_d-\gamma_d)} & \sin(\theta_d)\, e^{-j(\varphi_d-\gamma_d)} \end{bmatrix} * \begin{bmatrix} \sin(\theta_d)\, e^{j\varphi_d} & -\cos(\theta_d)\, e^{j\gamma_d} \\ \cos(\theta_d)\, e^{-j\gamma_d} & \sin(\theta_d)\, e^{-j\varphi_d} \end{bmatrix} \quad 5.15$$

$$= \begin{bmatrix} e^{j(2\varphi_d-\gamma_d)} & 0 \\ 0 & e^{j(2\varphi_d-\gamma_d)} \end{bmatrix} \quad 5.16$$

and:

$$\begin{bmatrix} \sin(\theta_s)\, e^{j\varphi_s} & \cos(\theta_s)\, e^{-j\gamma_s} \\ -\cos(\theta_s)\, e^{j\gamma_s} & \sin(\theta_s)\, e^{-j\varphi_s} \end{bmatrix} \begin{bmatrix} \sin(\theta_s) e^{j(\varphi_s-\gamma_s)} & -\cos(\theta_s) e^{2j(\varphi_s-\gamma_s)} \\ \cos(\theta_s) e^{-2j(\varphi_s-\gamma_s)} & \sin(\theta_s) e^{-j(\varphi_s-\gamma_s)} \end{bmatrix} \quad 5.17$$

$$= \begin{bmatrix} e^{j(2\varphi_s-\gamma_s)} & 0 \\ 0 & e^{j(2\varphi_s-\gamma_s)} \end{bmatrix}. \quad 5.18$$

This confirms the mapping of the horizontal state of polarization to that of polarizer, and the vertical state of polarization to the state orthogonal to the polarizer. What is still undetermined is the phase relationship between these two orthogonal vectors. If the polarizer is rotated to some off-axis polarization θ_p:

$$\begin{bmatrix} e^{j(2\varphi_d-\gamma_d)} & 0 \\ 0 & e^{j(2\varphi_d-\gamma_d)} \end{bmatrix} \begin{bmatrix} \sin(\theta_p) & -\cos(\theta_p) \\ \cos(\theta_p) & \sin(\theta_p) \end{bmatrix} \begin{bmatrix} 1 & 0 \\ 0 & 0 \end{bmatrix} * \begin{bmatrix} \sin(\theta_p) & \cos(\theta_p) \\ -\cos(\theta_p) & \sin(\theta_p) \end{bmatrix} \begin{bmatrix} e^{j(2\varphi_s-\gamma_s)} & 0 \\ 0 & e^{j(2\varphi_s-\gamma_s)} \end{bmatrix}. \quad 5.19$$

Multiplying through gives:

$$\begin{bmatrix} e^{j(2\varphi_d-\gamma_d)} & 0 \\ 0 & e^{j(2\varphi_d-\gamma_d)} \end{bmatrix} \begin{bmatrix} \sin^2(\theta_p) & \sin(\theta_p)\cos(\theta_p) \\ \sin(\theta_p)\cos(\theta_p) & \cos^2(\theta_p) \end{bmatrix} * \begin{bmatrix} e^{j(2\varphi_s-\gamma_s)} & 0 \\ 0 & e^{j(2\varphi_s-\gamma_s)} \end{bmatrix} \quad 5.20$$

and finally:

$$\begin{bmatrix} \sin^2(\theta_p)\, e^{j(2\varphi_d-\gamma_d+2\varphi_s-\gamma_s)} & \sin(\theta_p)\cos(\theta_p) e^{-j(2\varphi_d-\gamma_d+2\varphi_s-\gamma_s)} \\ \sin(\theta_p)\cos(\theta_p)\, e^{j(2\varphi_d-\gamma_d+2\varphi_s-\gamma_s)} & \cos^2(\theta_p)\, e^{-j(2\varphi_d-\gamma_d+2\varphi_s-\gamma_s)} \end{bmatrix} = \begin{bmatrix} r_{11} & r_{12} \\ r_{21} & r_{22} \end{bmatrix}. \quad 5.21$$

From (5.21) we can obtain the final correction matrices, thus establishing the required phase relationships to correctly read a linear polarizer at any angle. These final correction matrices take the form of:

$$P_d = \begin{bmatrix} 1 & 0 \\ 0 & e^{j*phase\left(\frac{r_{11}}{r_{21}}\right)} \end{bmatrix} \quad 5.22$$

and:

$$P_s = \begin{bmatrix} 1 & 0 \\ 0 & e^{j*phase\left(\frac{r_{11}}{r_{12}}\right)} \end{bmatrix}. \quad 5.23$$

The total transformation is then given by:

$$\begin{bmatrix} TE & MxE \\ ExM & TM \end{bmatrix} = P_d T_d \begin{bmatrix} A & B \\ C & D \end{bmatrix} T_s P_s. \quad 5.24$$

This is not the only technique for correcting for fiber rotation matrices, other techniques include the min-max eigenvector method, the principle states of polarization method, and others.

The min-max eigenvector works as follows: a Jones matrix is multiplied by its conjugate transpose; the eigenvectors of this matrix correspond to the maximum and minimum transmitting vectors through the original Jones matrix. Therefore if our DUT has one polarization (TE or TM) that has a significantly higher transmission than the other, we can approximately calculate the TE and TM response using this method.

The principle states of polarization method was first introduced in [25]. It requires a series of sampled Jones matrices. A single sample Jones matrix is multiplied by the inverse of the previous sampled Jones matrix, the eigenvectors of this matrix correspond to the vectors with the greatest and least group delay in the device. Therefore if our DUT is significantly birefringent for TE vs. TM we can assume the principle states are the TE and TM response.

Using the tunable-polarizer method, many measurements have been made with the optical vector analyzer. A sample measurement is shown in Fig. 34.

Fig. 34 A sample optical vector analyzer measurement.

One unresolved issue with this method stems from the average group delay subtraction that the measurement system performs. When measuring birefringent materials, once the measurement system has subtracted the average group delay, the Jones terms experience major phase shifts relative to one another as well as relative to subsequent Jones matrix spectral samples. This problem is then compounded by the fact that the arctan function only gives a value between 0 and pi/2. Effectively what this does to the algorithm is cause the Jones matrix terms to all switch places periodically. This problem also showed itself in different forms in the min-max eigenvalue method and the principle states of polarization method. In the end all of the methods work well on one single Jones matrix sample (or two samples for the PSP method), but have major issues with the entire spectrum; especially when there is noise in the system.

CHAPTER VI

SIGNAL PROCESSING APPLICATION 1: COMPLEX OPTICAL SPECTRUM ANALYZER*

A. Introduction

For advanced optical communication and sensing systems and photonic processing of radio-frequency (RF) and microwave signals, both the amplitude and phase of an optical waveform must be characterized. The phase and amplitude measurement of high bandwidth signals presents many challenges, particularly with respect to cost. This experiment proposes a new method to obtain the relative phase and amplitude of a periodic optical waveform in a cost-effective manner. The required major test equipment is reduced to a tunable dispersive device with a known dispersion, a photodetector and bandpass filter, a method of complex RF detection, and a computer.

Several techniques for determining the complex optical field have been proposed. In [26], the complex optical field is detected by combining the input signal with a modulated optical local oscillator, and detecting the phase from the heterodyne beat pattern produced thereby. Although this technique removes optical phase noise, it requires the use of a swept-wavelength laser source and secondary modulation source. Optical dispersion has also been used to characterize femtosecond optical pulses [27]-[28], and the complex spectral information can be extracted from the measurements.

Another modulation-based technique [29] requires a secondary modulation to interfere adjacent sidebands in combination with a tunable bandpass filter. In [30]-[31], the complex field is characterized by tuning the narrowband resonance of an all-pass filter across the signal spectrum. This experiment proposes to make use of the general approach in [30]-[31] with the variable dispersion provided by a series of thermally controlled silicon-nitride integrated optical ring resonators. The experiment will demonstrate the proposed technique on a range of test signals from phase modulation to double- and single-sideband amplitude modulation.

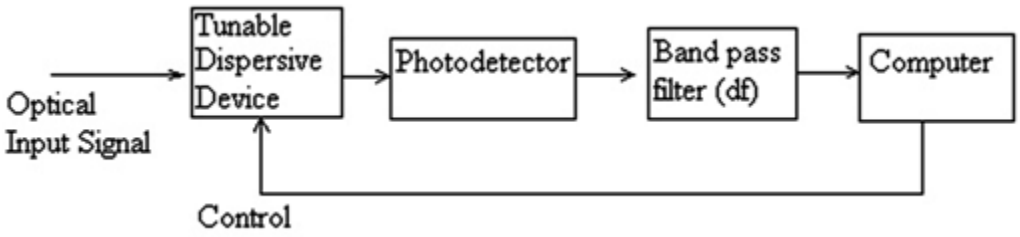

Fig. 35 Simplified complex optical spectrum analyzer block diagram.

B. Theoretical Background

The primary goal of our proposed system, shown in Fig.35, is to obtain the relative phase between adjacent tones of a periodic optical signal. It also provides the amplitudes of the tones once information is obtained on the amplitude for a single tone. For the mathematical analysis, we assume that there are N equally spaced tones as shown in Fig. 36, represented by their complex values $h_n = A_n e^{j\varphi_n}$ for $n = 1 \dots N$ where A_n is the tone amplitude and φ_n is the tone phase.

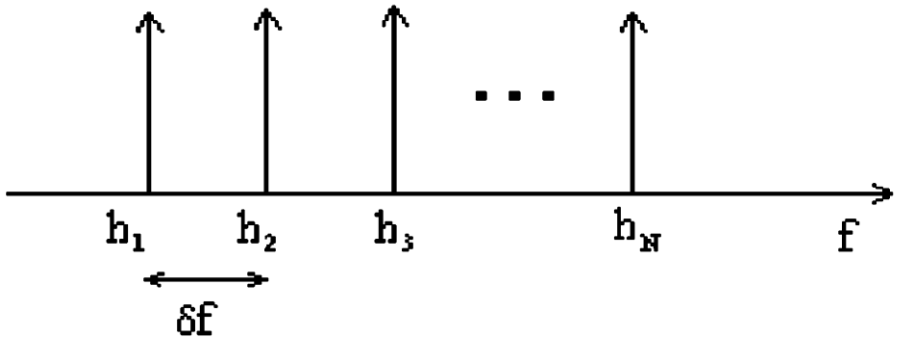

Fig. 36 The spectrum of an optical signal with N equally spaced tones.

Without any dispersion or filtering, the photodetector senses every tone mixing with every other tone. We only want the terms involving adjacent tones, so after photodetection we filter out the DC and higher frequency terms with an RF bandpass filter. The output of the filter then becomes:

$$e_{out}(t) = \sum_{n=1}^{N-1} (h_n^* h_{n+1} e^{j(\delta f)t} + h_n h_{n+1}^* e^{j(-\delta f)t}) \qquad 6.1$$

Heterodyne detection is then applied to the sum of first-harmonic terms to obtain a complex value, which we call "y", containing the magnitude and phase. The principle idea is to obtain several "y" readings at different dispersion values. In matrix form, the measurements create a "y"-vector as follows:

$$\begin{bmatrix} y_1 \\ y_2 \\ \vdots \\ y_{N-1} \end{bmatrix} = \begin{bmatrix} e^{j\Delta\varphi_{11}} & e^{j\Delta\varphi_{12}} & \cdots & e^{j\Delta\varphi_{1(N-1)}} \\ e^{j\Delta\varphi_{21}} & e^{j\Delta\varphi_{22}} & \cdots & e^{j\Delta\varphi_{2(N-1)}} \\ \vdots & \vdots & \ddots & \vdots \\ e^{j\Delta\varphi_{(N-1)1}} & e^{j\Delta\varphi_{(N-1)2}} & \cdots & e^{j\Delta\varphi_{(N-1)(N-1)}} \end{bmatrix} \begin{bmatrix} h_1^* h_2 \\ h_2^* h_3 \\ \vdots \\ h_{(N-1)}^* h_N \end{bmatrix} \qquad 6.2$$

where each of the phase terms in the matrix is obtained from the quadratic phase term given by:

$$\Delta\varphi_{mn} = 2\beta_{2m}\pi^2(\delta f)^2(2n-1) \quad 6.3$$

and the quadratic dispersion term β_{2m} is determined according to:

$$\beta_{2m} = -D_m\lambda^2/2\pi c \quad 6.4$$

where D_m is the dispersion value for the mth test, δf is the tone frequency spacing, λ is the wavelength, and c is the speed of light. By inverting the dispersion matrix, values for the relative phase between tones as well as the product of adjacent tone amplitudes is obtained. By measuring the magnitude for any single tone through a secondary measurement, we can obtain the magnitude and relative phase for all of the tones. This technique can theoretically be extended to a large number of tones, so long as the matrix remains invertible. If the rows have different dispersion values, they will not be linear combinations of one another. Additionally, the matrix terms of each row must enable a detectable difference for the measurement system.

C. Experimental Results

The complete experimental setup is shown in Fig. 37. The test signal uses an HP8168F laser source, operated at a fixed wavelength, and a dual-drive Mach–Zehnder optical modulator. By controlling the relative phase of the two RF drive signals controlling the modulator, a range of modulation formats is created for low modulation indices (i.e., low-power RF drive signals). Dual sideband (DSB) amplitude modulation is created when $\Delta\varphi = 180°$. Single sideband (SSB) amplitude modulation is created when $\Delta\varphi = 90°$. Phase modulation (PM) is created when $\Delta\varphi = 0°$. The linear

combinations of the magnitudes and relative phases of the tone pairs composing the modulated spectra are then detected and compared to theory.

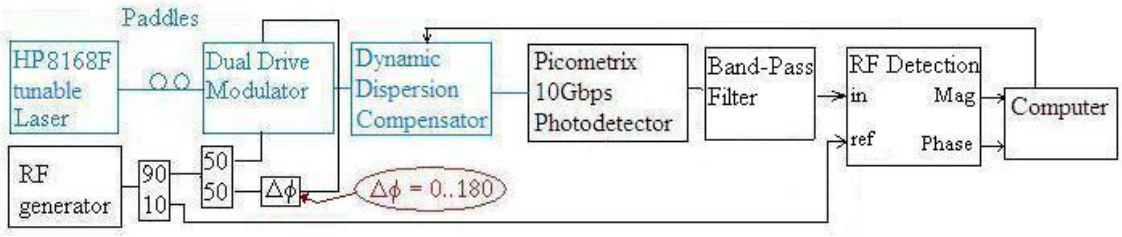

Fig. 37 Complete experimental setup of complex optical spectrum analyzer.

The tunable dispersive filter used in our experiment is a dynamic dispersion compensator (DDC) [32] manufactured by Little Optics. The DDC is comprised of 12 silicon-nitride optical ring resonators embedded within a polarization beam splitter to allow for independent control of both TE and TM polarizations (see Fig 38). Each ring is in an all-pass configuration, embedded within a Mach-Zehnder interferometer as described in Chapter IV (see Fig 20). Each ring has been equipped with thermal controllers in the ring feedback path and Mach-Zehnder reference path to allow for dynamic tuning of both the coupling constant and round-trip phase. As an off-the-shelf component, a computer controller allows for automatic setting of all the rings to proved dispersion between +1500 and -2500 ps/nm. Additionally each ring can be tuned independently, though such is not necessary for this experiment.

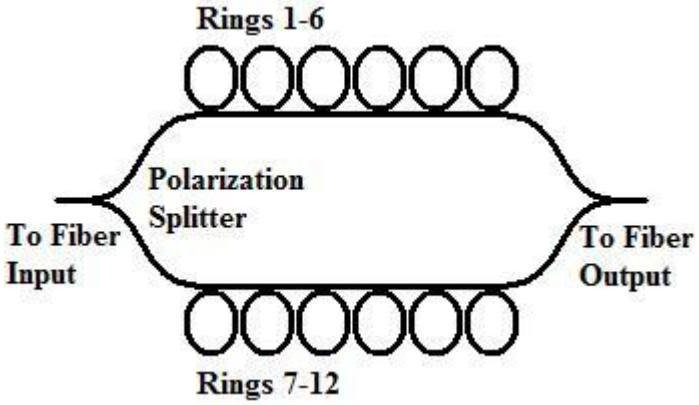

Fig. 38 Waveguide and ring structure of Dynamic Dispersion Compensator.

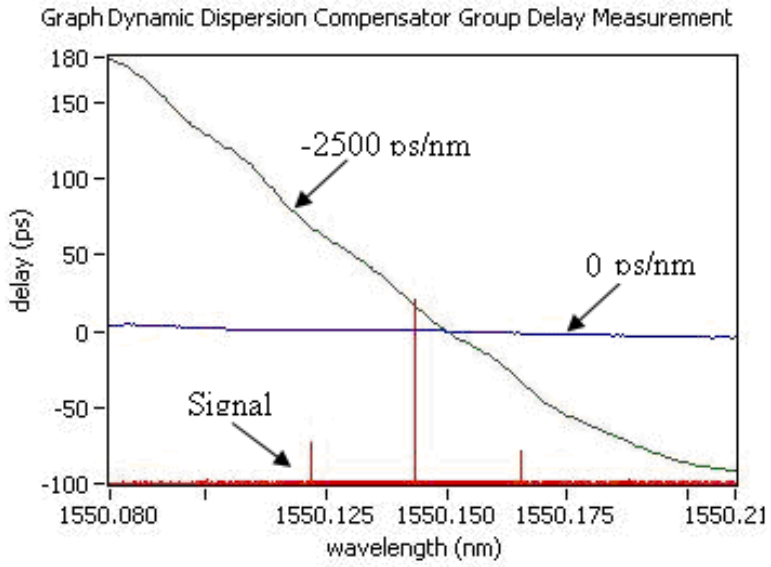

Fig. 39 Group delay measurement of the DDC, along with the relative location of the carrier and sidebands for 2.7-GHz modulation.

For this experiment, the DDC was first set to 0 ps/nm and then to -2500 ps/nm. The response of the DDC at these settings was characterized using the group delay measurement system described in Chapter V. The group delay is shown in Fig. 39 along

with an overlay of the modulated signal amplitude spectrum measured with the coherent optical spectrum analyzer, also described in Chapter V.

The experimental results as well as the theoretical predictions for a 2.7-GHz modulation frequency are shown in Figs. 40 and 41. As the modulation changes from amplitude to phase, one of the sidebands disappears near the 90 drive condition, and the relative phase of that sideband then switches rapidly by 180 just like the theory predicts.

We were able to measure waveforms from 2 to 5 GHz with this setup, with good comparison of the measurements to the predicted results. It should be noted that the 2- to 5-GHz tone spacing range is not a fundamental limit to the technique, but merely a limitation of our hardware. Tone spacing of less than 2 GHz can be measured, provided sufficient dispersion is available to make a detectable difference in the RF signal. Tone spacing above 5 GHz requires that the bandwidth of the optical and RF components increase correspondingly.

Several sources of error were present in the system. First a manual RF phase shifter, which introduced experimental uncertainty of a few degrees, was used to vary the drive condition to the modulator. There are also nonidealities in the RF amplitude and phase detection, which was accomplished with an Analog Devices AD8302 chip for frequencies less than 2.7 GHz (including Fig. 40 and 41) and with a combination of other RF components for frequencies greater than 2.7 GHz. Non-idealities in the dispersion were not a major source of error due to the narrow linewidth of each tone, but minor drifting of the entire dispersion curve (effectively the β_{1m} term) did require adjustment of the inverse matrix math to avoid large errors.

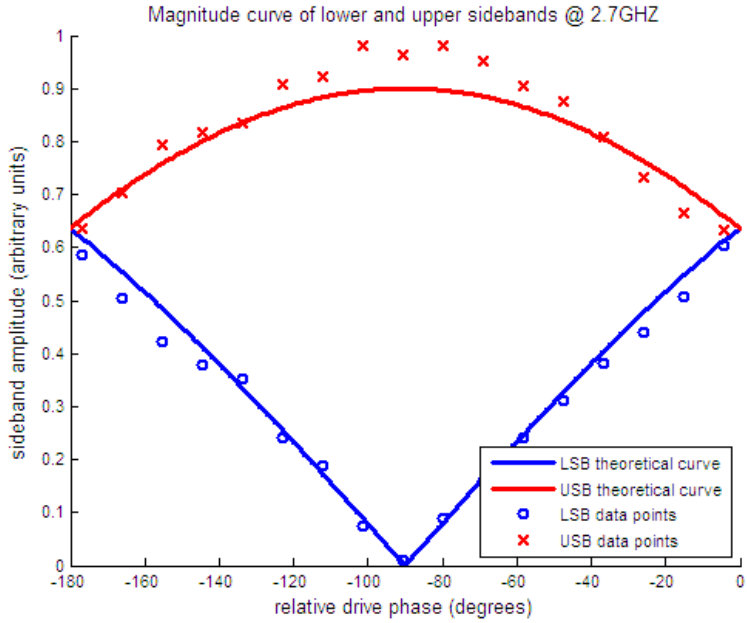

Fig. 40 Measured upper and lower sideband amplitudes and theoretical values as a function of the relative RF phase applied to the dual-drive modulator for 2.7-GHz modulation.

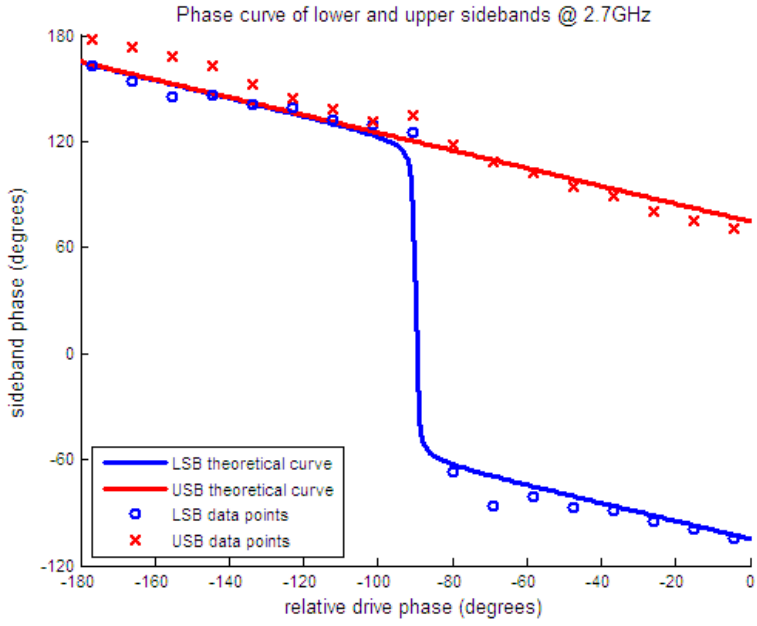

Fig. 41 Relative sideband phases (compared to an RF reference)and theoretical values as a function of the relative RF phase applied to the dual-drive modulator for 2.7-GHz modulation.

The relative power in a first-order tone was only 15%. We did not have enough RF power to overdrive the modulator to create significant power in the second-order modulation tones for a five-tone experiment.

In conclusion, a simple new technique was demonstrated for characterizing the complex optical field of an input waveform, without the use of a swept-wavelength source or secondary modulation. The underlying principles allow for extension of the detection system to larger signal bandwidths without requiring a higher bandwidth detector, on the condition that there are multiple tones and spacing between any two tones must be within the bandwidth of the detector. The relatively low modulation frequencies used in our experiment are a harder test than larger modulation frequencies since the dispersion entering the measurement matrix scales quadratically with modulation frequency.

CHAPTER VII

SIGNAL PROCESSING APPLICATION 2: DYNAMIC RF PHASE SHIFTER*

A. Introduction

A critical need for advancing the state-of-the-art for RF and microwave processing is wideband and lightweight beamformers. Wideband systems can be used to support multiple functionalities such as radar and communications. Current transmit and receive systems are limited by the beamforming network. Important factors for beam forming and steering systems that will merit practical deployment are achieving light weight, compact, and low cost designs while maintaining the desired performance parameters. Recently, optical RF phase shifters employing single-sideband (SSB) modulation with suppressed carrier and combined with a phase-shifted carrier from a separate path have been demonstrated [33]. These results show the potential for integrated optical circuits using broadband optical modulators. The architecture requires many crossing waveguide paths to combine the modulated signal and appropriately phased-carrier for each channel. The opportunity for extensive scaling is limited and this approach alone does not include delay tunability for beam steering.

True time delay approaches are required for sideband optical beam steering [33]. True time delay optical approaches have relied on dispersive optical fiber in the path of the beamforming elements and widely tunable lasers [34]–[35]. Lengths of fiber on the order of a kilometer have been employed, leading to a lack of compactness and ease of

---

fabrication, stability challenges, and related issues for scaling the number of elements. Bragg grating prisms have also been explored for the dispersive elements [36]. A continuous true time delay beam former has also been demonstrated using tunable chirped fiber Bragg gratings [37]-[38]. The use of fiber Bragg gratings does not scale particularly well either due to the large number of required array elements. From this brief summary, it is clear that new advancements are needed.

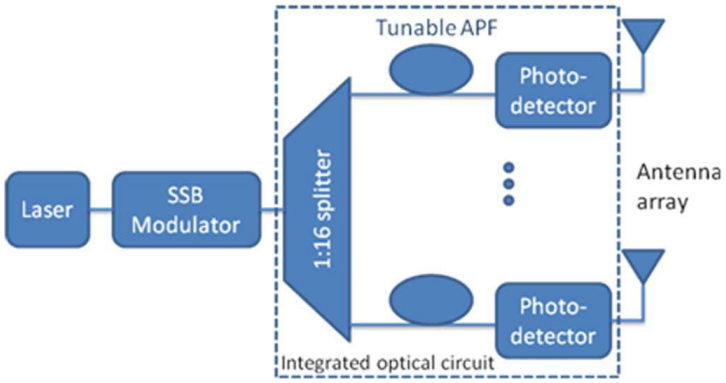

Fig. 42 Schematic of a new, simplified approach to realizing a photonic RF phase shifting array.

B. Proposed Setup

B.1 Broadband phase shifter architecture

A new approach for an optical RF phase shifting array employs optical filters to change the phase of the narrowband carrier without impacting the modulated signal. This approach requires SSB modulation of the wide bandwidth signal. Optical allpass filters (APFs), which can easily be made tunable, are used to vary the phase of the narrowband carrier with respect to the modulated SSB. A generic system for broadband RF phase shifting is shown schematically in Fig. 42. It dramatically reduces the

complexity of the required modulation and recombination optical circuits. In addition, it can easily be incorporated as part of a true time delay beamformer setup. For example, the tunable APFs' frequency response may be easily shifted across the frequency spectrum in systems employing tunable lasers and dispersive delays for beam steering. In addition, the APFs offer an integrated technology capable of tunable delays themselves.

Continuously variable delay lines that have a periodic frequency dependence – and thus can delay many channels simultaneously in contrast to typical Bragg gratings– can be realized using integrated optical ring resonators in an allpass configuration. This allows the full delay range to be tuned continuously when properly designed [39]-[41]. The RF magnitude may be changed for each channel in either the optical or electrical domains. In the optical domain, a simple attenuator suffices and can easily be integrated with the optical allpass filters. Alternatively, a variable-gain RF amplifier may be used in the electronic domain.

B.2 Modulator and filter implementation

Electro-optic, lithium niobate modulators are the preferred candidate for SSB modulation because of the large bandwidths that have been demonstrated. As described in previous chapters, SSB modulation is achieved by connecting a dual-drive Mach–Zehnder interferometer (MZI) modulator to quadrature inputs. The challenge with this approach is making a broadband hybrid RF splitter where the outputs differ in phase by 90 degrees over a wide RF bandwidth. Various approaches to achieving SSB modulation without relying solely on a near-perfect hybrid RF splitter may be pursued.

An example is to use double-sideband (DSB) modulation and eliminate one sideband via optical filtering, as depicted in Fig. 43.

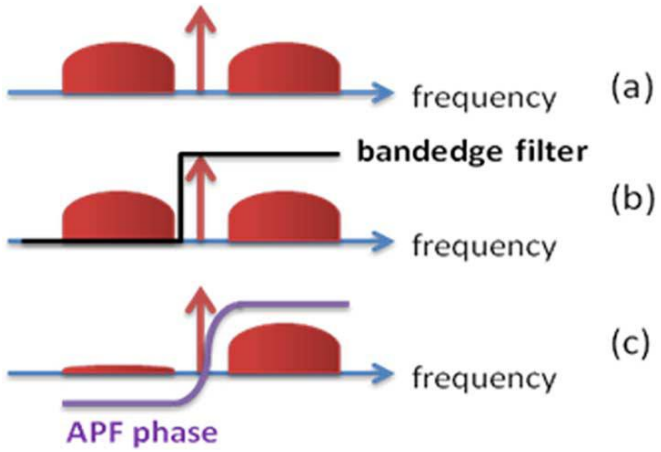

Fig. 43 (a) DSB modulated signal about the carrier. (b) Bandedge optical filter to eliminate one sideband. (c) Phase response of tunable optical allpass filter for phase shifting the narrowband carrier frequency.

Compact and continuously-tunable variable delays lines can be made and integrated on a chip using optical filters. The optical allpass filter is particularly well-suited to be used as a variable true time delay or phase shift device. By shifting the frequency response around the carrier, different phase shifts can be introduced on the narrowband carrier without impacting the modulated sidebands. When the carrier and modulated sideband are mixed at the photodetector, the modulated signal is shifted by the carrier phase. Although the phase response changes linearly near resonance, it flattens out further away from resonance. Thus, a control circuit that compensates for this nonlinear behavior and shifts the APF center wavelength accordingly to achieve the desired RF phase shift will be required in practical applications.

By cascading single ring APFs, any desired phase response can be approximated. The bandwidth over which the group delay is approximately constant becomes smaller for the larger group delays. As a result, it is practical to use the continuously tunable APF delay over a limited delay range and fixed delays with switches to choose the desired fixed path lengths for realizing longer overall delays. Thus, true time delay operation can be achieved with the proposed RF phase shifter.

C. Experimental Demonstration

C.1 Measurement setup

We used a commercially available dual-drive modulator, although a quadrature modulator [42] could also be used, to perform the SSB modulation for a narrowband RF signal. The experimental setup is shown in Fig. 44. A Mach–Zehnder dual drive optical modulator was used with a manual RF phase shifter in one drive arm to achieve accurate SSB modulation conditions. Drift in the DC bias for the optical modulator had to be compensated manually during warm up.

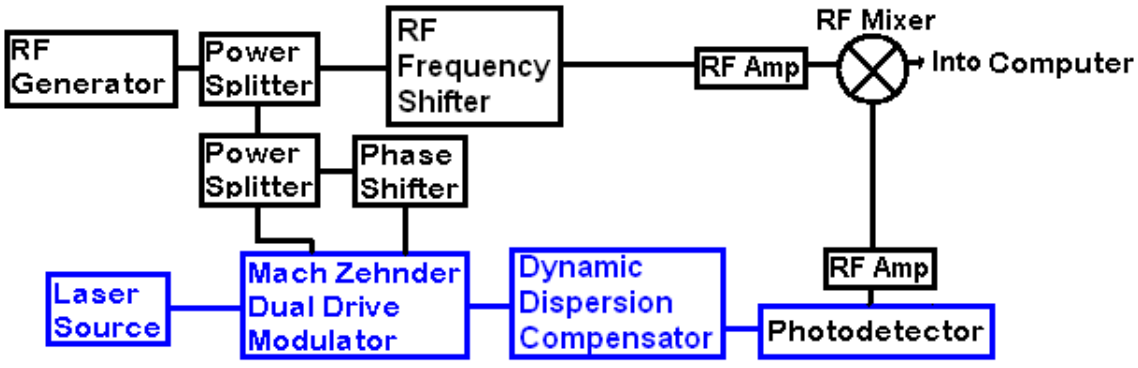

Fig. 44 RF phase shifter experimental setup employing single-sideband modulation.

On the detection side, RF mixers were employed for quadrature mixing of the received signal with a frequency-shifted RF reference (by 20 MHz) and subsequent phase detection. Because of their sensitivity to input power levels, the input powers to the mixers were consistently set.

Although the photodetector and amplifier used in the experimental setup only have listed bandwidths of 3 GHz and 1.5 GHz respectively, the RF phase shifter setup was able to work at an RF modulation frequency of 4.2 GHz. This required that the optical power of the laser be turned up to +3 dBm and the RF output power of the RF generator be turned up to +17 dBm. Getting 4.2 GHz to work from components not rated for those frequencies was worth the relatively high power.

The optical SSB modulator output was monitored with the coherent optical spectrum analyzer described in Chapter V to evaluate the frequency content of the signal. Results are shown in Figs. 45 and 46 for a typical SSB modulated spectrum.

For demonstrating RF phase shifting, the dynamic dispersion compensator (DDC) as described in Chapter VI was used again. In this experiment, rings were tuned individually rather than being set to create a constant dispersion. Only the tunable response of two rings was needed, so the other rings were set for minimum phase variation across our modulated signal's spectrum. A manual polarization controller in front of the DDC was used to tune the incoming polarization to only one arm of the DDC.

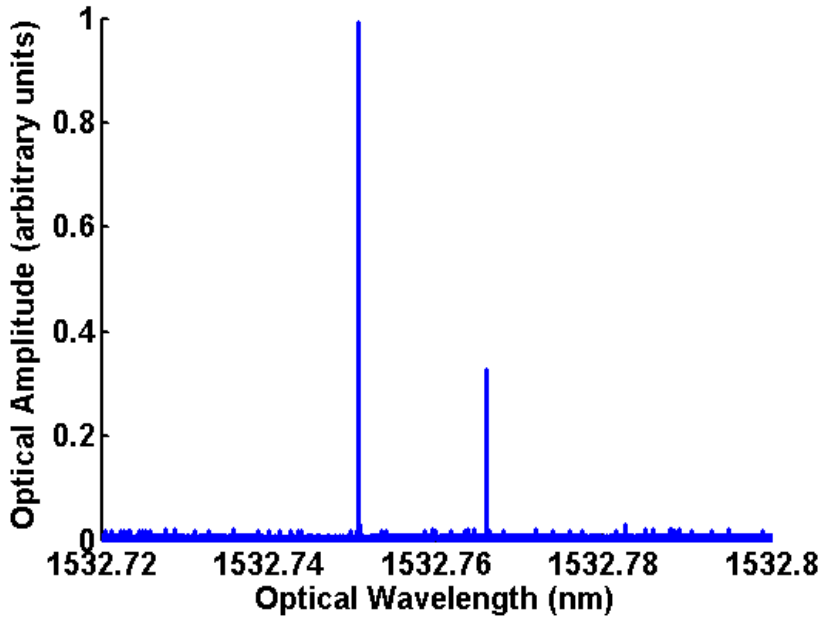

Fig. 45 Optical spectrums of SSB modulator output with modulation frequencies of 2.1 GHz.

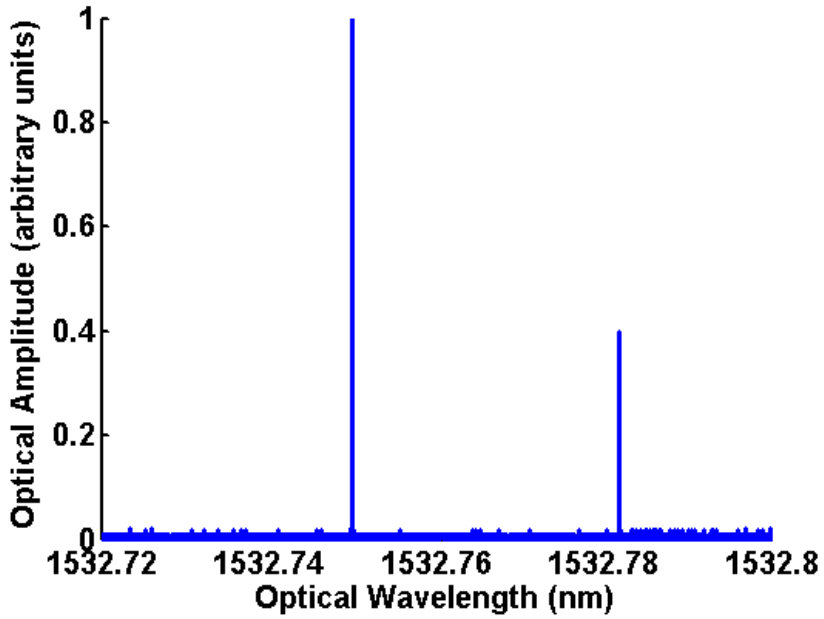

Fig. 46 Optical spectrums of SSB modulator output with modulation frequencies of 4.2 GHz.

For our first results, only one ring was used, whose resonance was centered at about 1532.78 nm. Because the phase change is only 360 degrees over one full FSR for a single ring, a minimum of two rings is needed to achieve an RF phase tuning range greater than 360 degrees. The measured RF phase is shown in Fig. 47 for two modulation frequencies, 2.1 and 4.2 GHz. Higher modulation frequencies could easily be accommodated by the optical filter; however, our RF components did not allow us to explore higher RF modulation frequencies.

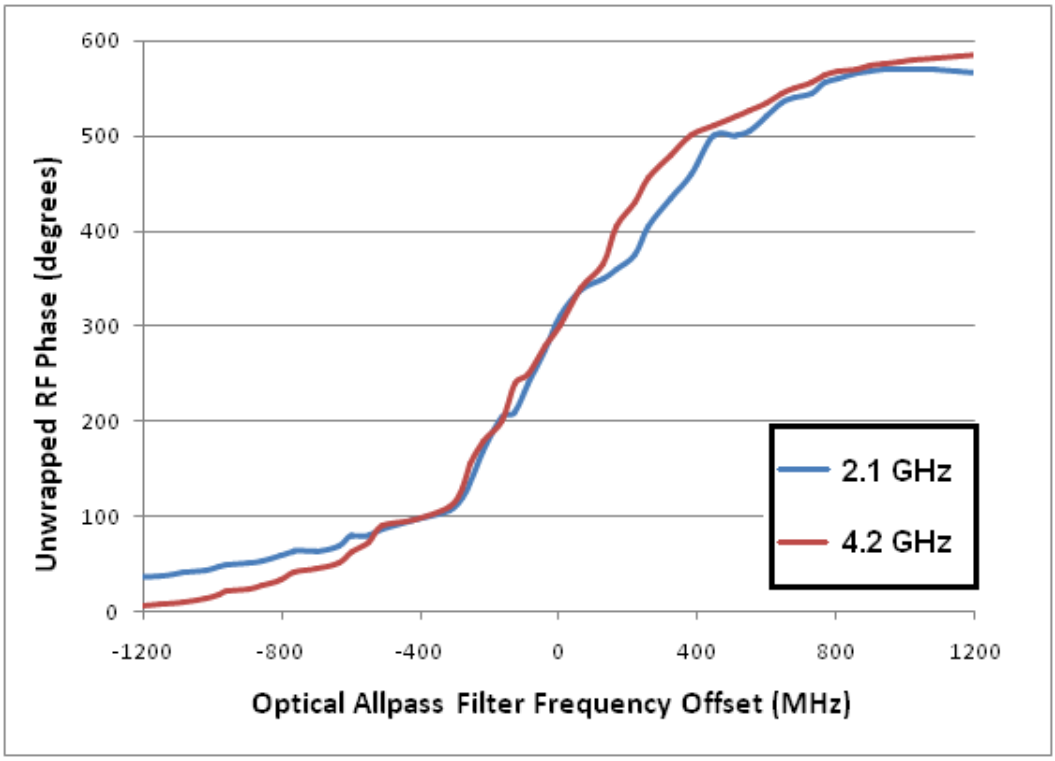

Fig. 47 Measurement results of RF phase change versus DDC setting.

The results are very close to the theoretical curves for the optical APF phase response for two cascaded rings with the same resonant frequency. Sources of uncertainty include the relative offset between the two rings as their resonant frequency is shifted; the precision of the frequency shifting; and drifts in input polarization for the SSB modulator and DDC device. Any changes of the remaining cascaded rings during the measurement, including the possibility of thermal crosstalk, may also impact this measurement result.

C.2 Optical filter response

Measurements of the insertion loss and phase over a couple FSRs for the nominal DDC settings are shown in Figs. 48 and 49. These measurements were taken with an Agilent swept laser source. Because we used 2 GHz as a minimum modulation frequency, it was necessary to set the allpass filter pole magnitudes close to unity to get a sharp phase response with respect to frequency. As a result, any losses in the ring feedback paths are resonantly enhanced and the loss spike will also be sharp. This very sharpness though will cause resonant loss spikes to affect the optical carrier only, leaving the sidebands relatively unaffected. If the minimum modulation frequency is larger, then a more gradual phase response can be employed and there will be a smaller amplitude variation of the ring response since the ring is set to a less resonant condition, even though round-trip ring loss remains unchanged.

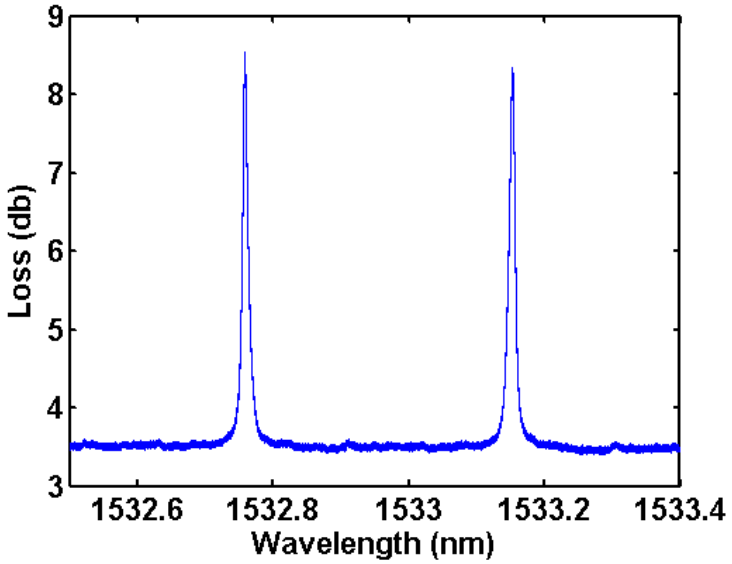

Fig. 48 Measured loss versus wavelength over two free spectral ranges of DDC for nominal settings (2 rings equally tuned).

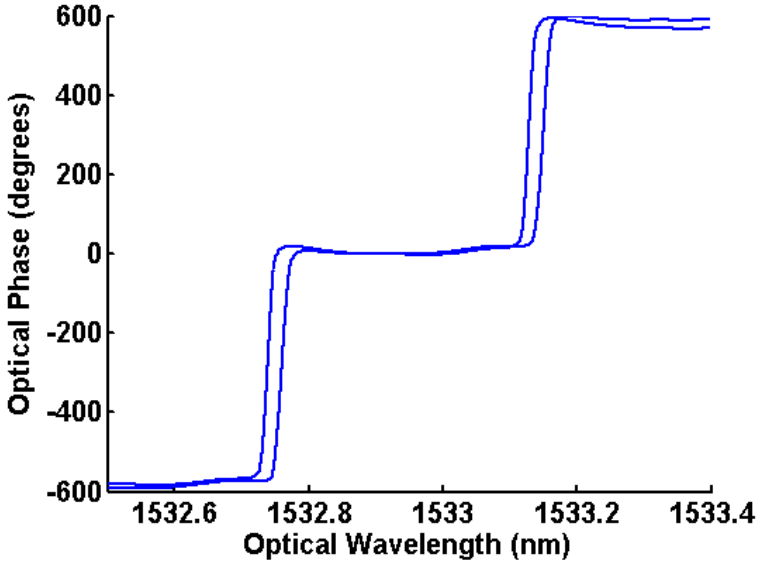

Fig. 49 Measured optical phase response versus wavelength over two free spectral ranges of DDC for nominal DDC settings (2 rings equally tuned). Two frequency offset conditions corresponding to the minimum and maximum shift used for the RF phase experimental data are shown.

A lossless APF is the ideal solution to eliminate the frequency dependent loss. In practice, we must accommodate a finite loss in the feedback path. A flat magnitude response can be achieved by balancing the pole and zero at reciprocal locations about the unit circle. A single APF embedded in one arm of a Mach–Zehnder interferometer where at least one of the MZI couplers is tunable allows us to tune both the pole and zero location, even in the presence of loss, and achieve this operating condition at the expense of some tradeoff in flat loss [7]. Another narrowband solution is proposed in [43] by optimizing group delay with bandwidth and amplitude variation.

Additionally a variable gain RF amplifier may be used to compensate for the frequency dependent loss if an optical solution is undesirable. This is because most modulation indices will be relatively small, so some carrier loss should not affect the final RF signal structure, only its amplitude.

The loss of the carrier and a 2 GHz sideband was measured using a coherent optical spectrum analyzer for various settings of the DDC and plotted versus the RF phase of the output in Fig. 50. No appreciable loss versus RF phase was found for the 2 GHz sideband.

Optical phase measurements for the DDC settings at the maximum and minimum frequency shift are shown in Figs 51 and 52. The challenge is to have the phase response rolloff to a gradual phase change region before the lowest modulation frequency.

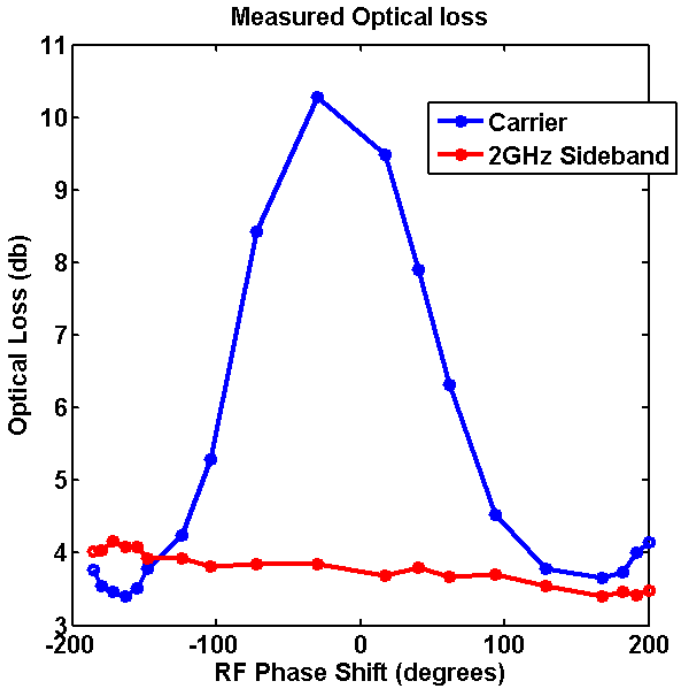

Fig. 50 Measured optical band loss versus RF phase shift for various DDC frequency shift settings.

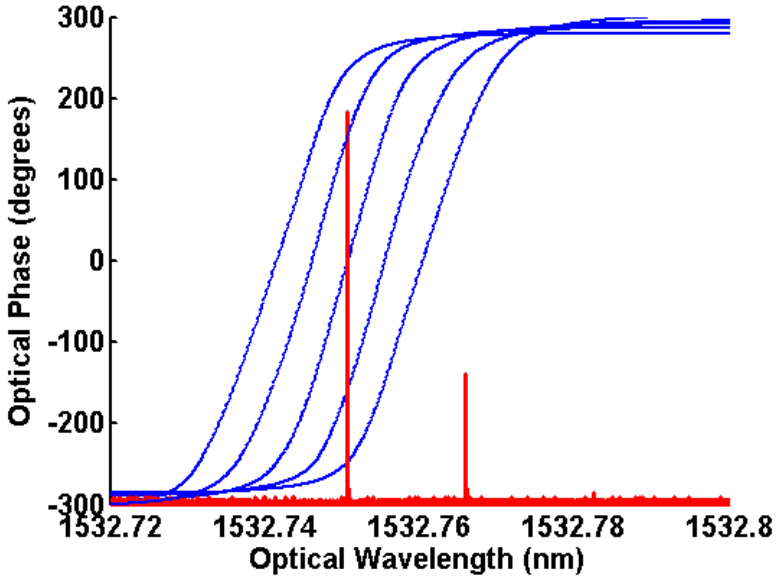

Fig. 51 Overlay of optical phase spectrum from the tunable allpass filter with the optical amplitude spectrum from the Mach–Zehnder modulator for a 2.1 GHz modulation frequency.

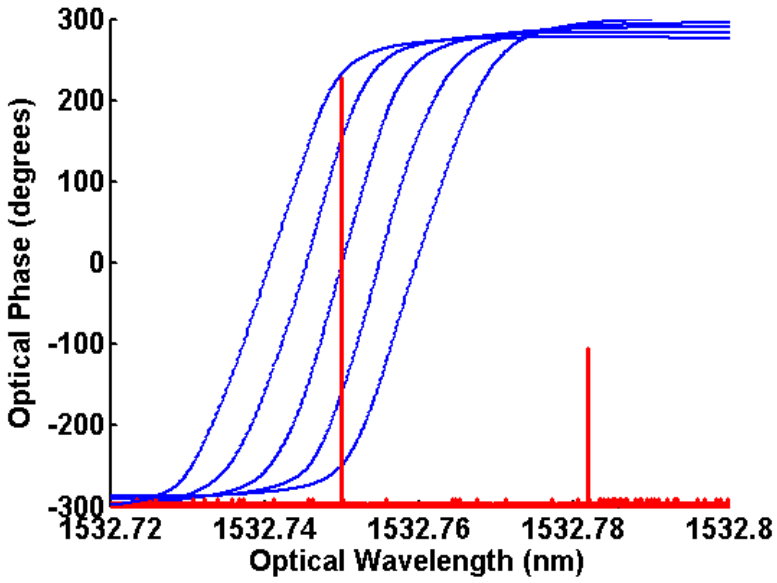

Fig. 52 Overlay of optical phase spectrum from the tunable allpass filter with the optical amplitude spectrum from the Mach–Zehnder modulator for a 4.2 GHz modulation frequency.

This technique lends itself to deployment in arrays with the cost of a DFB laser and RF SSB modulator split amongst many channels. By using a multi-stage allpass filter, a large range of RF phase shifts can be achieved. The DDC used in this experiment allowed for tuning of both the pole magnitude as well as the resonance frequency of each ring. For the RF phase shifter application, it is only necessary to tune the frequency shift in practice. So, the pole magnitude can be designed to achieve the fast change in the phase response, dictated by the minimum modulated frequency condition. By simplifying the ring design, such as eliminating the ability to tune the pole magnitude, lower round-trip losses can be achieved and the magnitude response will vary substantially less across the FSR of the optical allpass filter.

CHAPTER VIII

SIGNAL PROCESSING APPLICATION 3: LADAR WAVEFORM GENERATION*

A. LADAR Background

Two characteristics of great importance in LAser Detection And Ranging (LADAR) systems are long range performance and fine range resolution. The long range performance implies a good carrier to noise ratio (CNR), therefore matched filters are generally used during detection to maximize the CNR. The point target matched filter response for an arbitrary waveform is the autocorrelation function (ACF) which forms a Fourier transform pair with the energy spectrum of the signal. However, most real world targets have multiple reflection points, and the sidelobes generated by the matched filter for any one reflection point will contribute to the noise for all the other reflection points. Therefore reducing the waveform's ACF sidelobe levels can greatly improve the overall CNR and thus the long range performance.

Fine range resolution stems from the ability to temporally distinguish reflections generated by adjacent points. Therefore reducing the temporal width of the mainlobe of a waveform's ACF will improve fine range resolution.

With this in mind it becomes clear that choosing the correct waveform is of great importance in a LADAR system. Over the years many different waveforms have been proposed including linear frequency modulation (LFM) chirped waveforms [44], pseudo-random phase modulated waveforms [45], poly-phase (P4) waveforms [46], and others.

The conventional method used most often to reduce the sidelobes of a waveform's ACF is to pulse carve the waveform's amplitude window. By choosing a suitable window function (e.g. Hamming, Blackman, Taylor etc.) the range sidelobes can be suppressed to the level required. There are, however, two drawbacks to this technique. Pulse carving always results in a significantly larger main lobe width. Also, if the peak transmission power is limited, a windowed pulse will inevitably contain less energy than a rectangular one of the same duration, leading to a corresponding loss in CNR at the receiver.

In contrast to pulse carving a waveform's amplitude window, sidelobe reduction can be accomplished by distorting the frequency modulation function, i.e. creating a non-linear frequency modulated (NLFM) chirp [47]-[48]. Recently significant improvements in long-range performance and fine range resolution have been shown using a specific NLFM chirp called the tangent frequency modulation (tan-FM) chirp. It was first introduced for SONAR applications [49] but quickly was adopted for RADAR [50] and LADAR [51] applications as well. In [51] the waveform was compared via simulation to several of the aforementioned waveforms for LADAR systems and was found to have better characteristics overall.

Not much literature exists about hardware implementations of NLFM chirped waveforms for LADAR or otherwise. In [52] the authors propose a non-linearly stepped frequency waveform, mimicking a NLFM chirped waveform. In [53] the authors show how a series of integrators can create a polynomial phase chirp.

This experiment proposes a new method for implementing an NLFM chirped optical waveform using integrated optical ring resonators. First there will be a review the tan-FM function and its benefits. How tunable integrated optical ring resonators can create a NLFM chirped waveform similar in structure to the tan-FM waveform will be explored next. Finally a simple proof-of-concept experiment to verify the integrated optical ring resonator's capability of generating NLFM chirped waveforms will be performed.

B. Previous Waveforms

B.1 NLFM vs. LFM

The optimal design of any NLFM chirped waveform has the greatest amount of non-linearity near the ends of the chirp pulse. To aid in understanding consider the two chirped waveforms shown in Fig. 53, and their corresponding ACF's shown in Fig. 54. Both chirps have a bandwidth of $\frac{10}{T}$. The linear chirp has a uniform frequency slope throughout the pulse. Correspondingly its ACF has -13.8 db sidelobe and a full width half maximum (FWHM) time of $0.05 \times T$ (5% of the waveform period). On the other hand the non-linear chirp has a steeper frequency slope at the beginning and end of the pulse, which causes the sidelobe level of its ACF to decrease to -27.5 db while its FWHM time increases to $0.072 \times T$ for this particular NLFM chirped waveform.

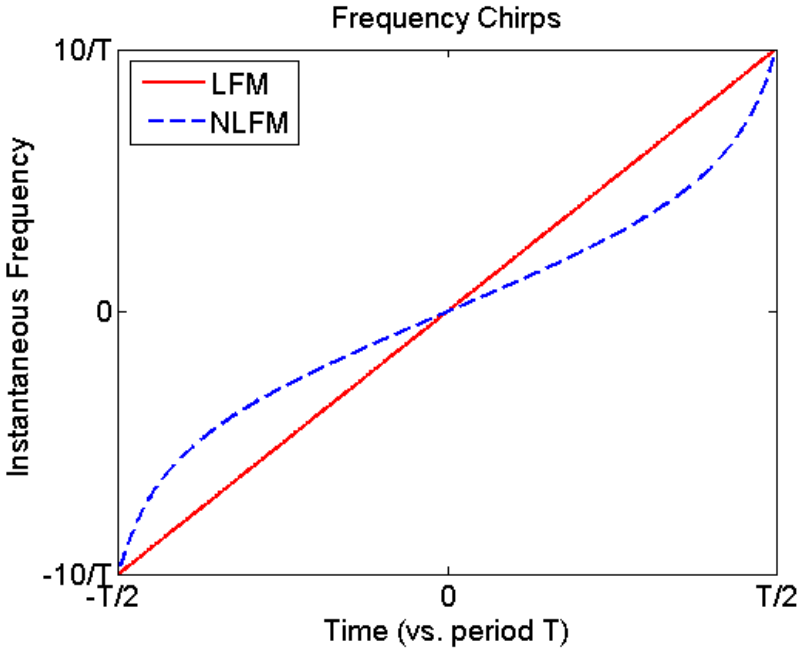

Fig. 53 The instantaneous frequency of an LFM chirped waveform and an NLFM chirped waveform.

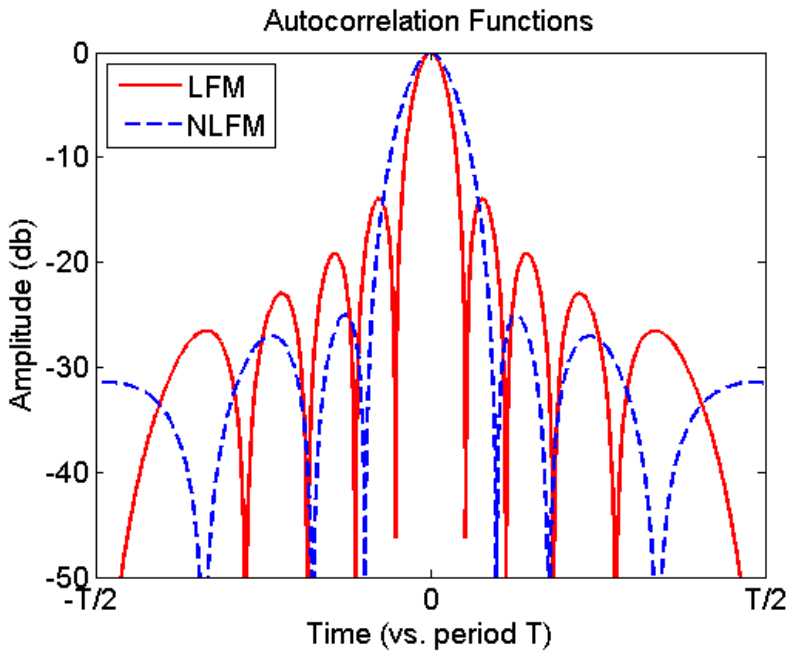

Fig. 54 The ACF of the LFM chirped waveform and an NLFM chirped waveform. The NLFM signal exhibits much lower sidelobes, but a somewhat wider FWHM.

B.2 Tan-FM settings

The tan-FM function yields instantaneous frequency as a function of time. Shown as a first derivative of phase with respect to time:

$$\varphi'(t) = \pi B \left[\frac{\alpha \tan\left(\frac{2\gamma t}{T}\right)}{\tan(\gamma)} + \frac{2(1-\alpha)t}{T} \right] \quad 8.1$$

where the 4 principle variables to describe the tan-FM chirped waveform are: γ, the portion of the tan(x) curve that is used; α, the balance between tan-FM and LFM; *B*, the bandwidth of the chirp; and T, the period of the chirp i.e.

$$\frac{-T}{2} \leq t \leq \frac{T}{2}. \quad 8.2$$

Not all tan-FM settings are equally beneficial, for example, setting alpha or gamma equal to zero is equivalent to a LFM signal. To discover the optimal settings we simulated the tan-FM chirped waveform and its ACF for the following range of values

$$0.8 \leq \gamma \leq 1.56 \quad 8.3$$

$$0.25 \leq \alpha \leq 1 \quad 8.4$$

$$B = \frac{10}{T}. \quad 8.5$$

The FWHM times (as a fraction of the period T) vs. sidelobe levels (in db) were plotted on a scatter plot (see Fig. 55 a). Optimally the sidelobes and FWHM times should be as small as possible (which corresponds to the bottom left corner of the scatter plot). Therefore removing results with large FWHM times and/or high maximum

sidelobe levels, the narrowed tan-FM chirped waveform settings fall into one of two ranges:

$$0.6 \leq \gamma \leq 1.08 \tag{8.6}$$

$$0.85 \leq \alpha \leq 1 \tag{8.7}$$

or:

$$1.12 \leq \gamma \leq 1.44 \tag{8.8}$$

$$0.66 \leq \alpha \leq 0.84 \tag{8.9}$$

and these can be seen in Fig. 55b.

It should be remarked that the tan-FM function is capable of achieving sidelobe levels of less than -40 db. This requires a greater bandwidth though. For larger bandwidths a third range of tan-FM chirped settings becomes useful:

$$B \geq \frac{35}{T}. \tag{8.10}$$

$$1.42 \leq \gamma \leq 1.52 \tag{8.11}$$

$$0.88 \leq \alpha \leq 0.94. \tag{8.12}$$

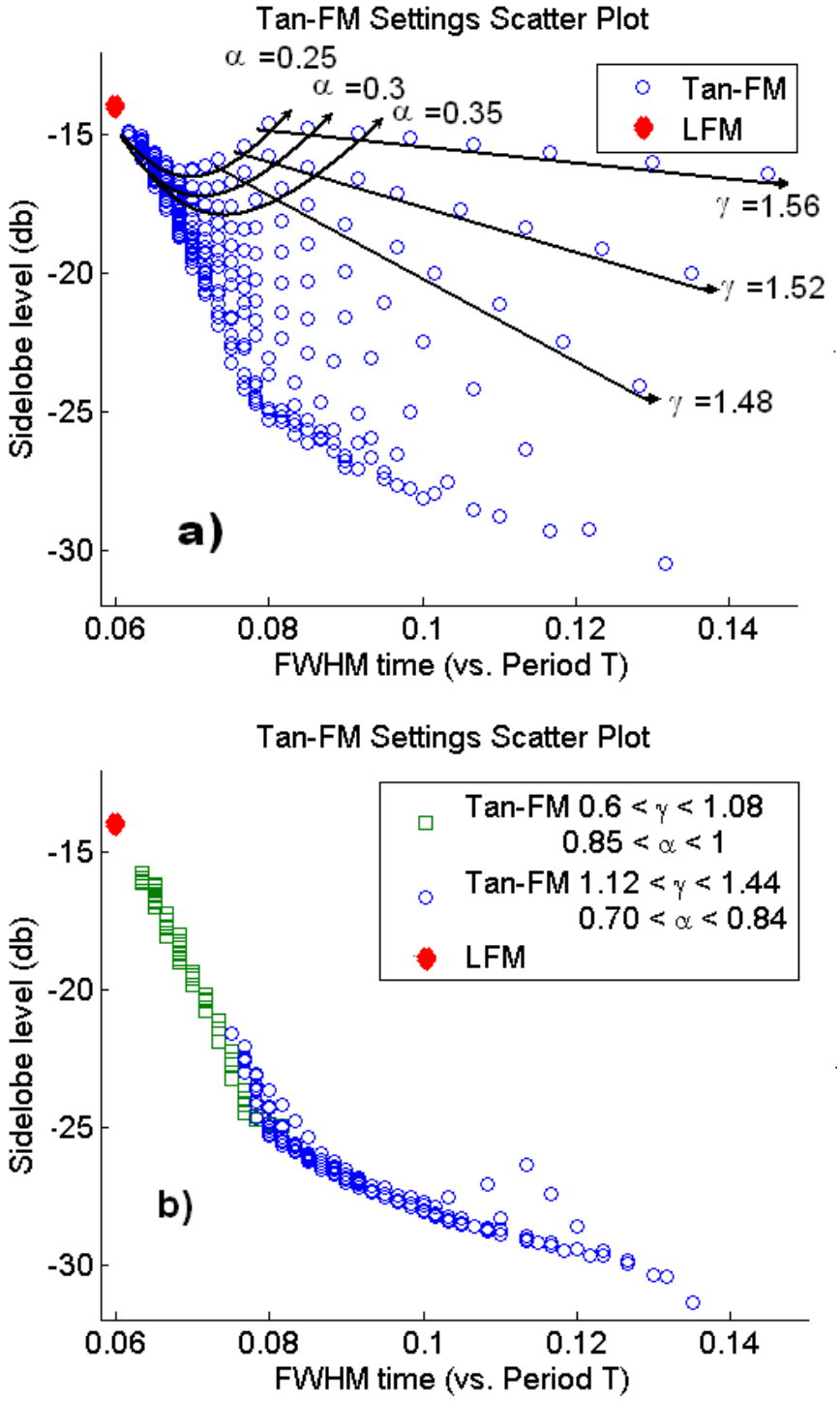

Fig. 55 Scatter plots of the tan-FM chirped waveform with a variety of settings. Each circle represents the maximum sidelobe level and FWHM time of the ACF of a tan-FM chirped waveform. a) Broad tan-FM settings. b) Narrowed, more optimal tan-FM settings.

C. Ring Resonator Simulations

C.1 Basic setup

The primary tool to generate NLFM chirped waveforms for consideration here is the tunable integrated optical ring resonator in an all-pass configuration. By shifting the ring's frequency response around the carrier, non-linear phase shifts can be introduced on the narrowband carrier which will then in turn lead to non-linear frequency chirps. For example, a 16.67 MHz sine wave modulation introduced to a ring with a transmission coefficient of $\theta = \frac{\pi}{3}$ will yield a NLFM chirped waveform as shown in Fig. 56a. Clearly the frequency chirps are evenly spaced, and these correspond to the time at which the filter's resonance point passes over the carrier wavelength.

In addition to the ring resonator a phase modulator along a straight waveguide external to the ring is added such that approximately linear chirps can be added to the non-linear frequency modulated chirped waveform generated by the ring. This simulation assumes a sinusoidal input to the external phase modulator, which actually generates sinusoidal frequency modulated chirps (see Fig. 56 b). This is acceptable though since the chirps are approximately linear over the region of interest, i.e. their ramp falls off at the same time that the rings frequency ramp increases dramatically.

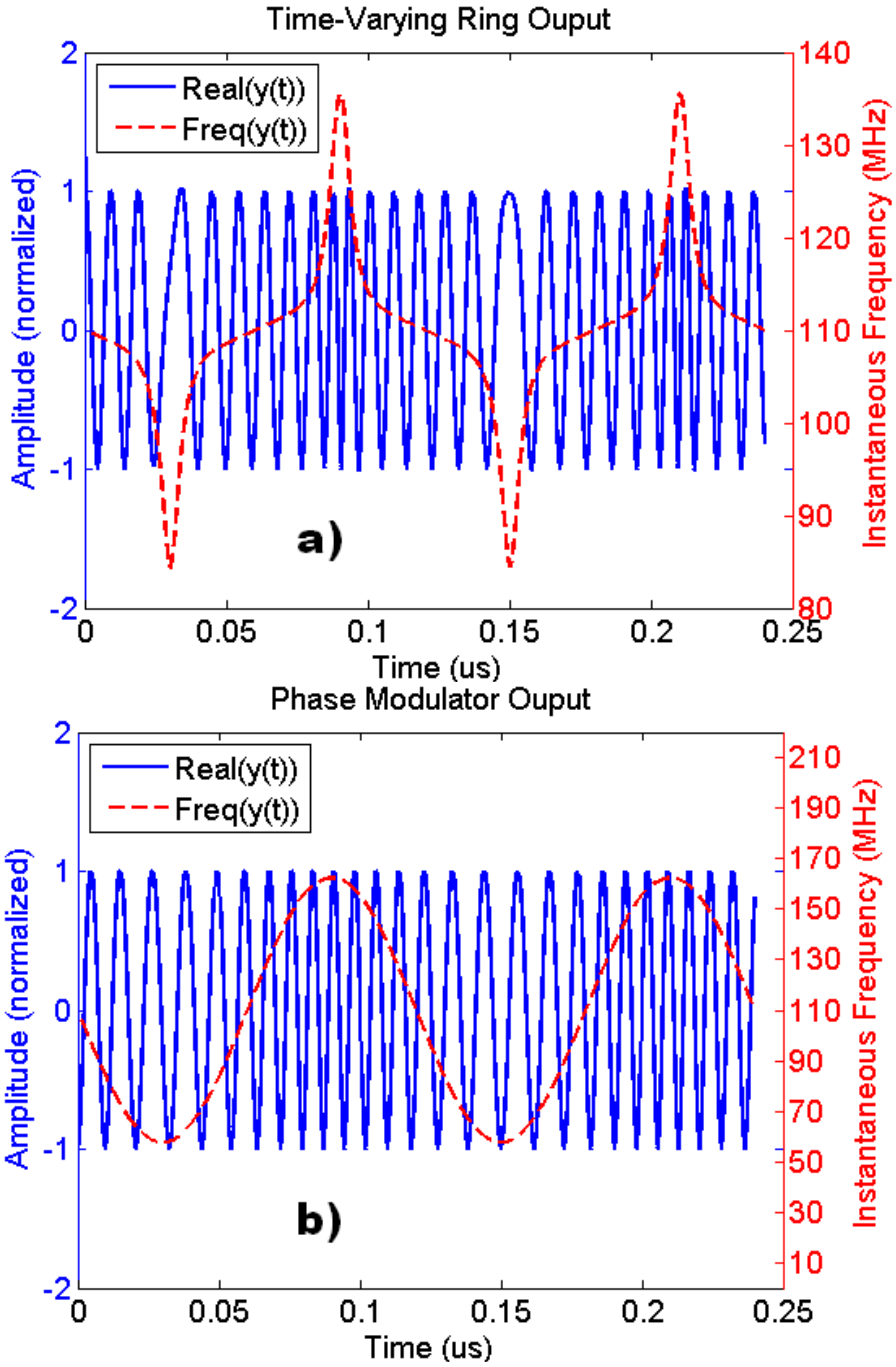

Fig. 56 a) The time and frequency output of a ring resonator with a coupling constant of 0.5 whose refractive index is modulated with a 16.67 MHz cosine wave. Here a 110 MHz carrier was used as the narrow-band ring input for graphical purposes. b) The output wave and instantaneous frequency of a straight waveguide refractive index modulator, modulated with the 16.67 MHz cosine wave.

C.2 Tan-FM chirp vs. ring chirp

Evaluation of the performance of the non-linear frequency modulated chirped waveform generated by a ring resonator and phase modulator begins by comparing their NLFM chirps to a similar tan-FM chirp. The following simulations assume two identical rings so that the ACF's will show multiple sidelobes. The transmission coefficient of the two identical rings is set to $0.37*\pi$, and the phase modulator is set to add $\frac{2.73}{T}$ Hz of approximately linear chirp. The tan-FM settings are $\gamma = 1.25$ and $\alpha = 0.75$. Both signals have a bandwidth $B = \frac{10}{T}$.

These two chirps have strikingly similar ACF's (see Fig. 57). With identical FWHM times, the ring generated NLFM chirped waveform has slighly lower sidelobes (29db vs. 26db). Later it will be shown that this result is fairly representative of many ring generated NLFM chirped waveforms (with a bandwidth of $\frac{10}{T}$); they can be 3db lower than a comperable tan-FM chirp or more.

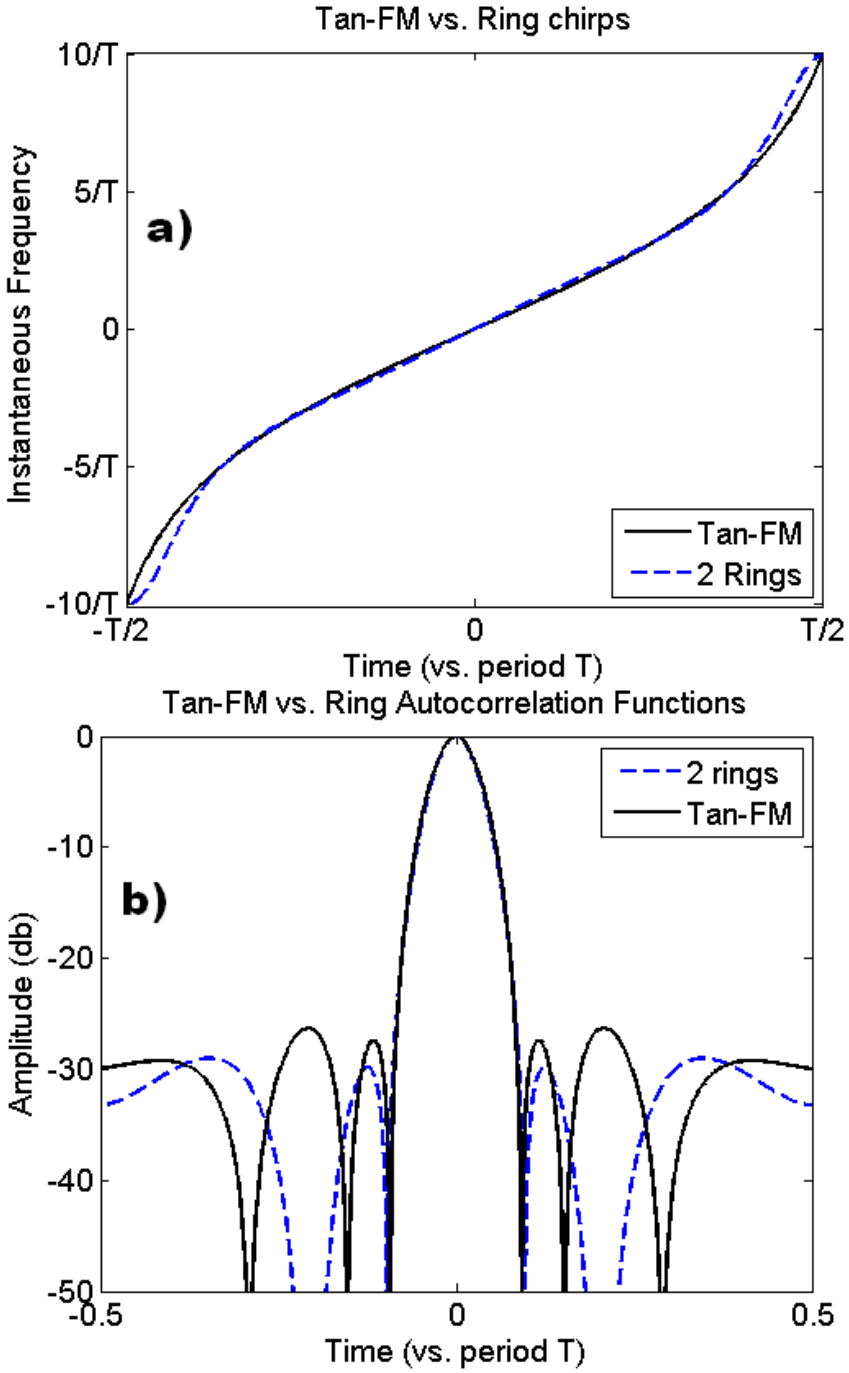

Fig. 57 a) Instantaneous frequency chirp of a tan-FM signal (with a bandwidth $B = \frac{10}{T}$, $\gamma = 1.25$ and $\alpha = 0.75$) versus two identical rings with coupling of theta = 0.37*pi and 0 round-trip loss as well as a phase modulator given $\frac{2.73}{T}$ Hz of approximately linear chirp. b) The matched filter output corresponding to an input of a tan-FM chirped waveform and 2 time varying ring resonators and phase modulator.

C.3 Effect of ring coupling

In this simulation the transmission coefficient of two identical rings was varied from 0.25π to 0.375π. From feedback filter theory as more power is transmitted into the ring the spectral phase response of the ring becomes less sharp, which will result in smaller and more spread out NLFM chirped waveforms. In Fig. 58a we see just this effect: the higher transmission coefficients have smaller bandwidths but smoother frequency ramping.

One would expect that the NLFM chirped waveforms with the largest bandwidths would have the best ACF characteristics (see Fig. 58 b). Surprisingly though the sidelobe levels and FWHM times decrease as the transmission coefficients increase despite the lower bandwidths. Upon closer examination it becomes apparent that increasing the transmission coefficients increases the portion of the chirp that has a non-linear frequency ramp.

This trend doesn't continue indefinitely though; for the case where the phase modulator is set to add $\frac{2.73}{T}$ Hz of approximately linear chirp the optimal transmission coefficient for two rings is near $\theta = 0.35\pi$. Fig. 58b shows that when $\theta = 0.375\pi$ the sidelobe levels have increased as compared to $\theta = 0.35\pi$. This value of the transmission coefficient isn't optimal generally; the optimal value is dependent on how much linear chirp is added and how many rings are used.

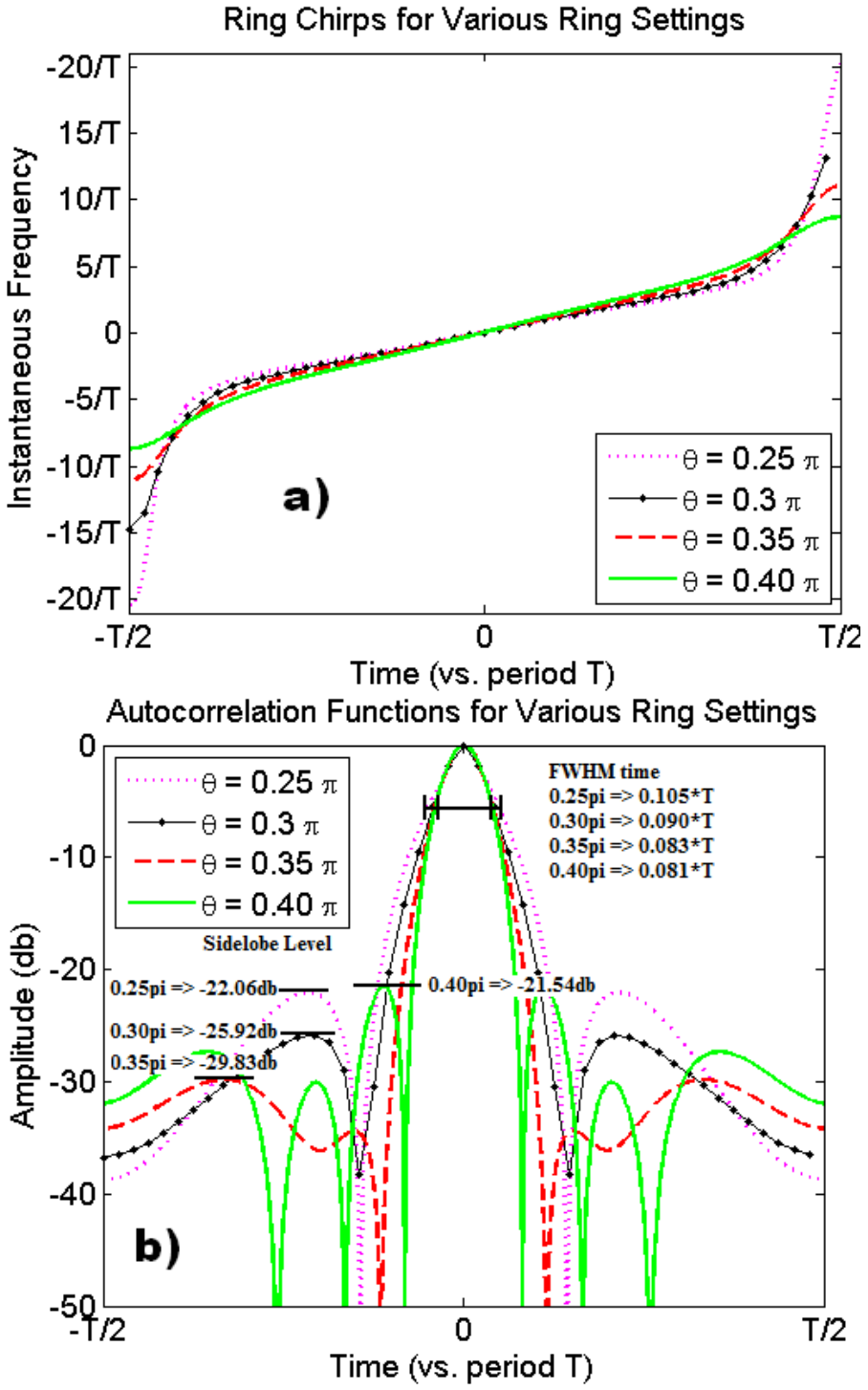

Fig. 58 a) Instantaneous chirp of two identical rings with various transmission coefficients. The output of the two rings in all cases was passed through a phase modulator given $\frac{2.73}{T}$ Hz of aproximately linear chirp. b) The ACF corresponding to the waveforms shown in a.

C.4 Optimal ring settings vs. tan-FM function

Just like the tan-FM chirped waveform, the ring-generated NLFM waveform has four variables, or rather four controlling quantities, the number of rings, the ring transmission coefficients (may be different for each ring), the approximately linear frequency chirp contribution from the external phase modulator, and the period of the chirp. Other than the period of the chirp, these quantities don't have a one-to-one correspondence to the tan-FM function variables, i.e. the bandwidth of the waveform is a mixed function of the number of rings, their transmission coefficients and the amount of approximately linear frequency chirp.

This simulation measures the sidelobe level and FWHM time of the autocorrelation of the ring generated NLFM waveform for multiple rings with a variety of coupling constants and plots them on a scatter plot once again. To make a fair comparison to the tan-FM chirped waveform sufficient linear chirp is added such that:

$$B = \frac{10}{T} \qquad 8.13$$

where B = the chirp bandwidth. Fig. 59 a) shows the results assuming two rings which may have different coupling constants and Fig. 59 b) shows the results assuming three rings which may have different coupling constants. Comparing only the optimal settings for the rings and the tan-FM function, the two ring case had autocorrelation sidelobes 0-3 db lower than the tan-FM waveform's autocorrelation sidelobes of equal FWHM. The three ring case on the other hand showed autocorrelation sidelobes 3-7 db lower than the tan-FM waveform's autocorrelation sidelobes of equal FWHM.

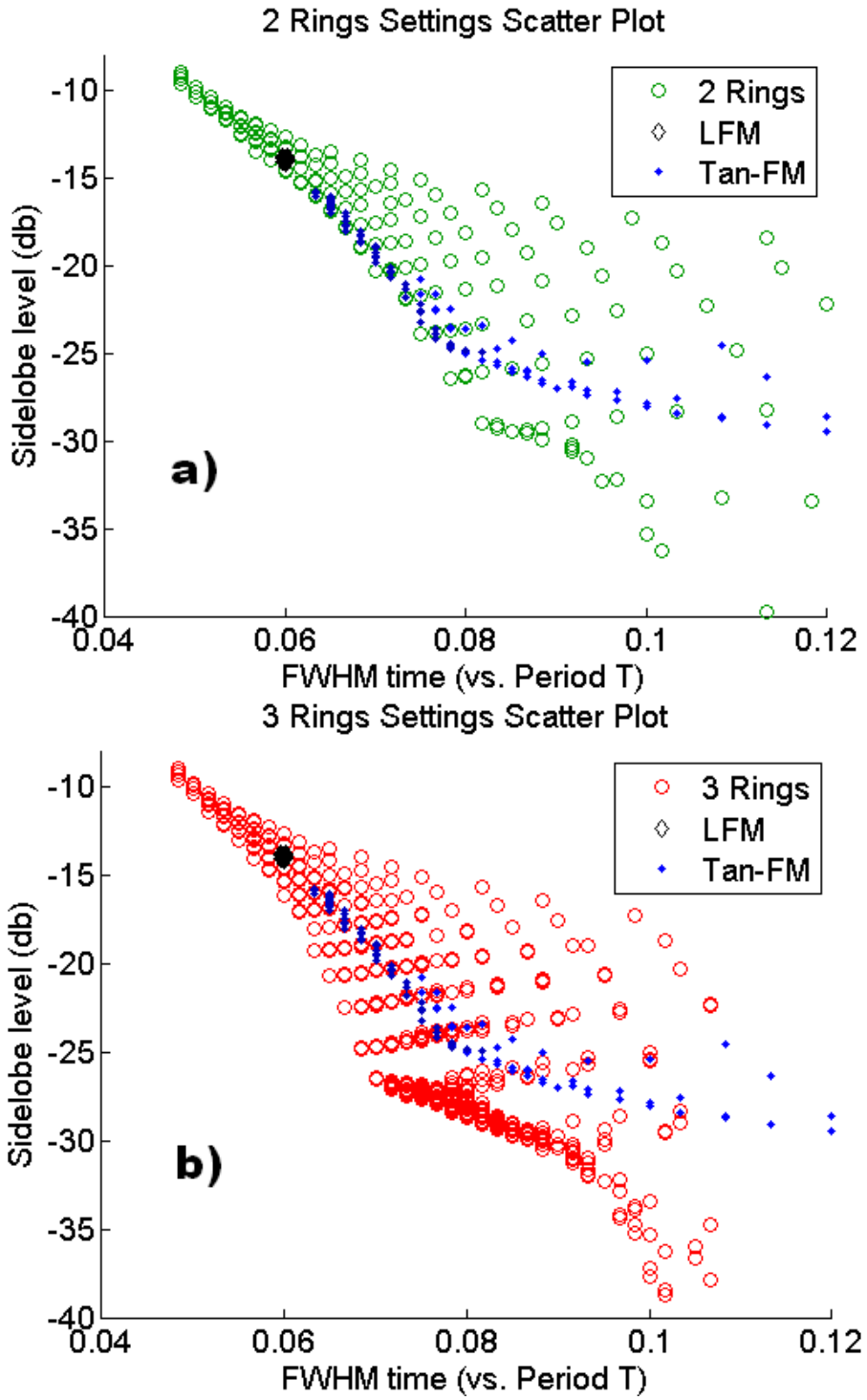

Fig. 59 Scatter plots of the ring generated NLFM chirped waveform's ACF sidelobe levels and FWHM times, plotted against the tan-FM scatter plot from the preceding section for a) 2 rings b) 3 rings. Each ring may have a different transmission coefficient.

C.5 Optimal ring settings including phase difference

The previous section focused on achieving minimum ACF mainlobe width and sidelobe level for a fixed bandwidth through optimization of the ring coupling constant only. One important factor that was neglected was the analysis of chirps generated by rings with different round-trip phases. Phase offset can come not only due to fabrication processes, but also by application of a constant offset to the ring round-trip modulator.

As it turns out, variations in ring round-trip phase can lead to much better optimized performance of an NLFM chirp with a fixed bandwidth. Fig. 60 shows the mainlobe widths and sidelobe levels of ring generated NLFM chirped waveforms under a wide variety of settings, all with a fixed chirp bandwidth $= 10/T$. As can be seen, NLFM chirps generated with rings with identical coupling constants but different phase offsets exhibit lower ACF mainlobe widths and sidelobe levels.

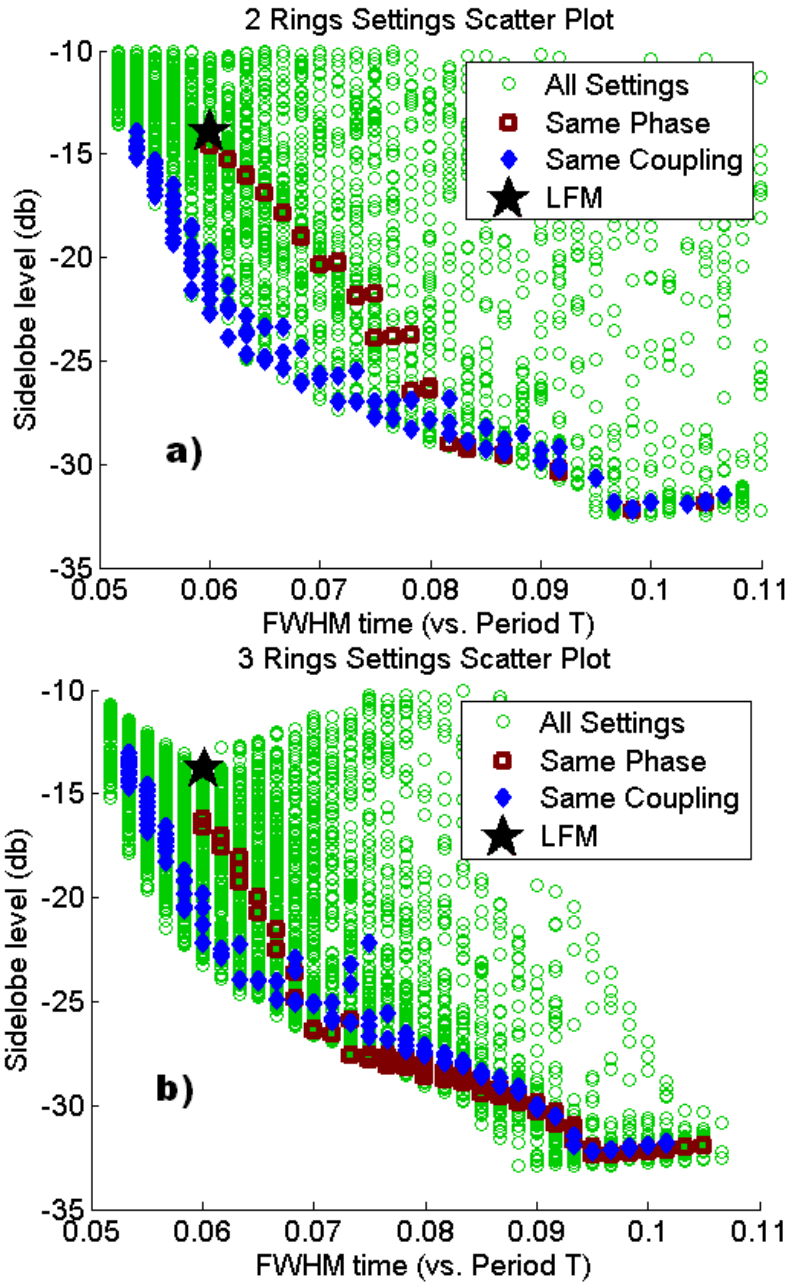

Fig. 60 Scatter plots of the mainlobe widths and sidelobe levels of simulated ACF's of NLFM chirped waveforms generated by rings with a variety of coupling constants and phase offsets. In all cases bandwidth $B = \frac{10}{T}$ a) Green circles: two different rings $\theta = 0.3\pi \ldots 0.47\pi \ \partial\varphi = 0 \ldots \pi$; blue diamonds: two identical rings $\theta = 0.335\pi \ldots 0.365\pi \ \partial\varphi = 0 \ldots 0.7\pi$, and ; red circles: two different rings $\theta = 0.35\pi \ldots 0.42\pi$ and no phase variation. b) Green circles: three different rings $\theta = 0.3\pi \ldots 0.47\pi \ \partial\varphi = 0 \ldots 0.45$; blue diamonds: three identical rings $\theta = 0.3775\pi \ldots 0.4025\pi$ and $\partial\varphi = 0 \ldots 0.75\pi$; red circles three different rings $\theta = 0.415\pi \ldots 0.44\pi$ and no phase variation.

C.6 Optimization of fixed-coupling constant rings

The previous section showed how changing the relative phase between the ring round-trip phases can lead to significant improvements in NLFM chirp ACF mainlobe widths and sidelobe levels. Although in Chapter IV it was shown that tuning of the coupling constant is possible by embedding the ring resonator within a Mach-Zehnder interferometer, in some cases it may be desirable to fabricate rings with a fixed coupling. The question this simulation seeks to answer is how assuming 2 identical ring resonators with fixed coupling constants, how much improvement to the mainlobe width and sidelobe level can be obtained by varying the relative round-trip phase between the rings as well as the linear chirp bandwidth contribution.

Scatter plots showing the simulated ACF mainlobe widths and sidelobe levels of NLFM chirp generated by two ring resonators with a coupling constants of 0.65 and 0.85 are shown in Figs. 61 a and b respectively. For the case where the ring coupling $\kappa = 0.65$ sidelobe levels decreased by about $-5db$ per $0.01 * T$ FWHM increase, up to $-24db$ (as shown in Fig. 60 a); whereas for the case where the ring coupling $\kappa = 0.65$ sidelobe levels decreased by about $-3db$ per $0.01 * T$ FWHM increase, up to $-31db$ (as shown in Fig. 60 b). It is important to remember that this simulation did not assume a fixed bandwidth like the previous simulations, but rather fixed coupling constant rings.

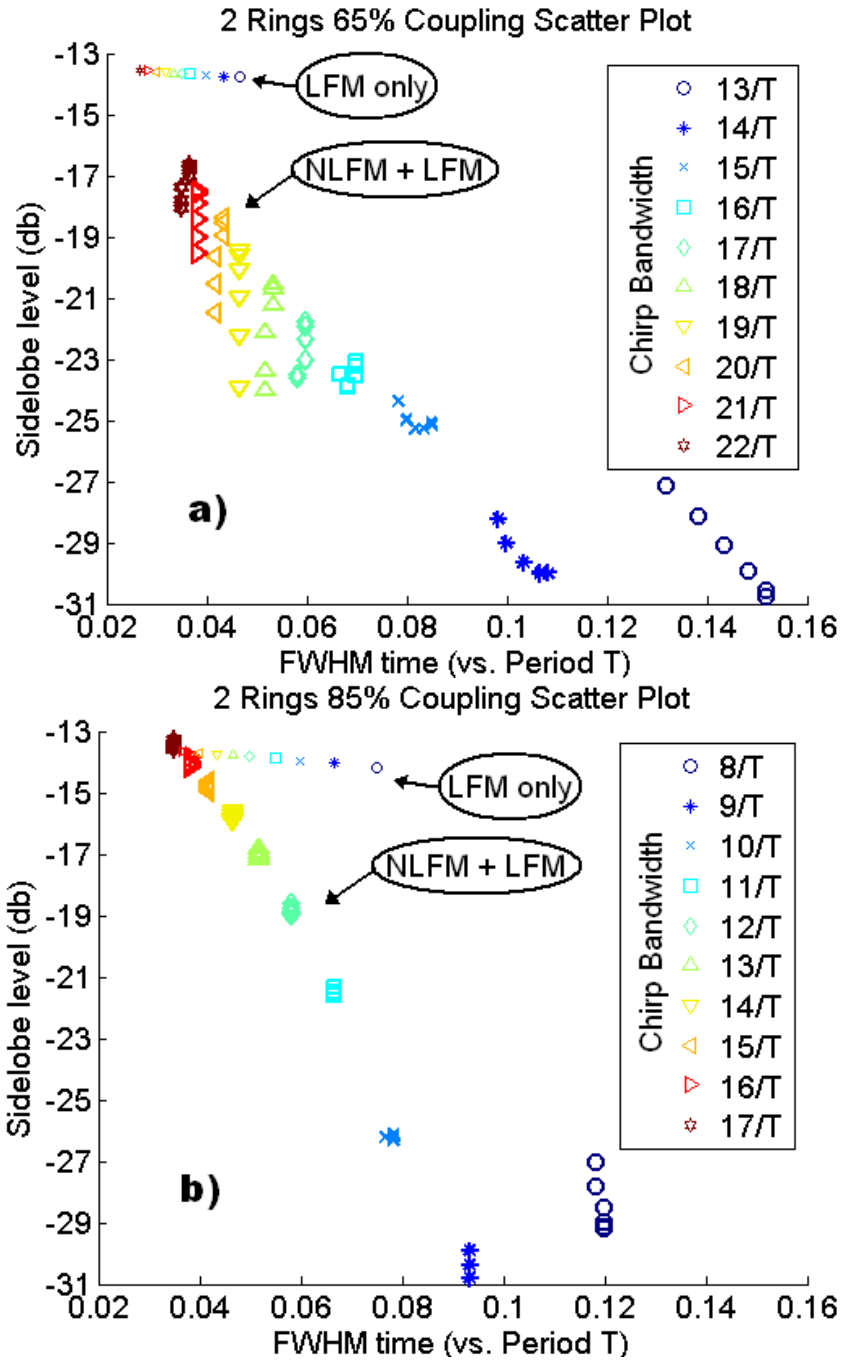

Fig. 61 The simulated ACF mainlobe widths and sidelobe levels of NLFM chirped waveforms generated by two lossless rings a) with identical coupling constants $\kappa = 0.65$, $\partial\varphi = 0 \ldots 0.25\pi$ phase variation, and $1/T \ldots 10/T$ bandwidth of additional linear chirp b) with identical coupling constants $\kappa = 0.85$, $\partial\varphi = 0 \ldots 0.25\pi$ phase variation, and $1/T \ldots 10/T$ bandwidth of additional linear chirp.

C.7 Effect of ring loss

The preceding simulations assumed no round-trip ring loss which all real-world integrated optical ring resonators will have. Not surprisingly as the round-trip ring loss increases, both the sidelobe levels and the FWHM times increase (see Fig. 62). For these simulations it was assumed two identical rings with transmission coefficients of $\theta = 0.33\pi$ and a linear phase modulator contribution of $\frac{3.14}{T}$ Hz of chirp.

Although the best solution is to minimize round trip loss, the side-lobe levels and FWHM times may be benefitted by increasing the transmission coefficient when loss is present. Feedback theory can show that increasing the transmission coefficient spreads the ring's phase and amplitude spectrum, which will spread and reduce the loss over a larger time portion of the NLFM chirped waveform.

Fig. 62 shows that increasing the transmission coefficient from $\theta = 0.33\pi$ to $\theta = 0.385\pi$ reduces the sidelobe levels and FWHM times of two identical rings with 1db of roundtrip loss. Once again, the optimal transmission coefficient depends on how much linear frequency chirp is added to the signal via the external phase modulator.

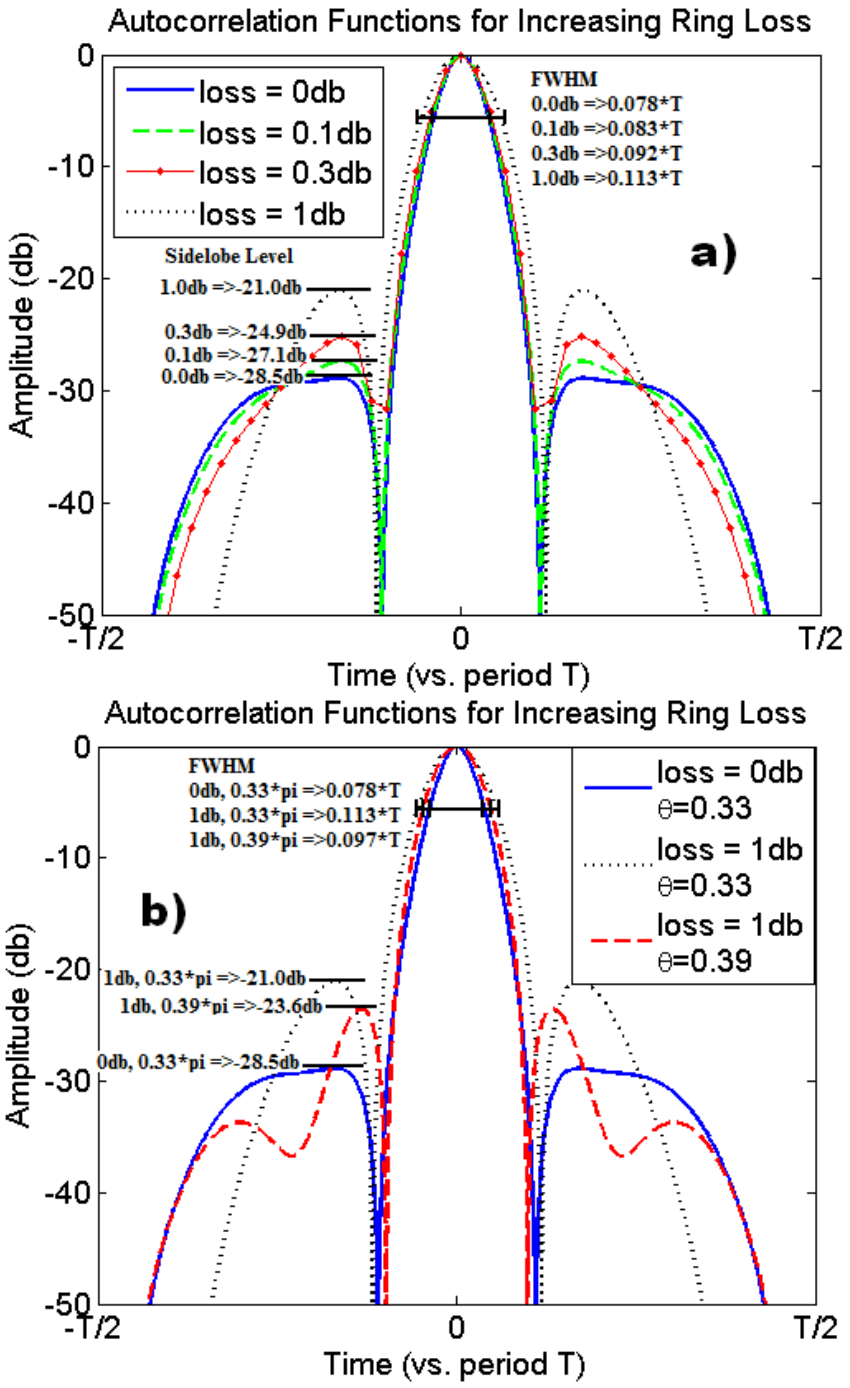

Fig. 62 a) The autocorrelation function of a ring generated NLFM chirped waveform with two identical ring resonators each having a coupling coefficient of $\theta = \frac{\pi}{3}$ and various amounts of round-trip loss. b) The negative effects of roundtrip loss on the FWHM time and sidelobe level can be mitigated by increasing the transmission coefficient.

C.8 Chirp pattern and ACF characteristics

The above results were all computed for a single isolated chirp; a series of chirps will generate ACF's with higher sidelobes, and this applies to the tan-FM chirped waveform as well as the ring generated NLFM chirped waveform. If the chirp series follows a sawtooth pattern, each successive chirp being identical to the last, the chirp ACF's sidelobes will only be slightly higher (≈3db). On the other hand if the chirps have a triangular pattern, alternating between frequency increasing chirps and frequency decreasing chirps (like Fig 56 a), the chirp ACF's sidelobes will be significantly higher (≈10db). If the modulators in the proposed system are given a sine wave input the chirped output will follow a triangular pattern. However a fully rectified sine wave input will generate chirps in a sawtooth pattern.

D. Proof of Concept Experiment

This experiment is designed to simply prove that tunable integrated optical ring resonators will indeed produce chirps when their refractive index is tuned sufficiently rapidly. This experiment will use a thermally controlled silicon-nitride ring found in the DDC (see Chapter VII). These will be placed within a fiber Mach-Zehnder interferometer (see Fig. 63), to effectively allow for detection of the frequency chirps at baseband. A fiber polarizer will also be used to tune the polarization to the principle polarization of the ring.

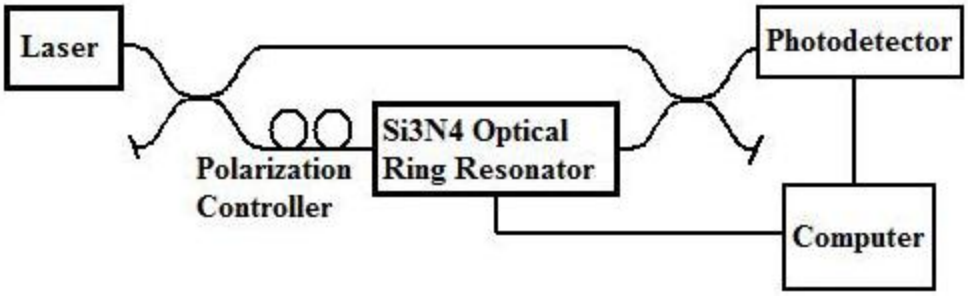

Fig. 63 Basic setup of the proof of concept experiment. The Si3N4 tunable integrated ring resonator is placed within a fiber MZI such that the output waveform can be measured at baseband.

The rings in the DDC have been equipped with a thermal controller such that the refractive index can be controlled by the thermo-optic effect. For most real-world applications we will want a faster index changing effect than the thermo-optic effect (such as charge carrier injection, or the electro-optic effect). Because the refractive index is directly related to temperature, the refractive index can only be dynamically tuned on an order of milliseconds. This means that at best only kilohertz frequency chirps will be possible, but such will suffice for this simple proof of concept experiment.

Furthermore, as stated before these rings were designed for dispersion compensation. Therefore direct control of the ring temperature is not possible, aka. The rings have been designed to simply ramp up or down to a given temperature. Consequently, the refractive index will be modulated by a ramp function rather than the sine wave function used in the preceding simulations. This means only half of the NLFM chirp can be generated with this setup. Despite all of these draw-backs, several optical frequency chirped waveforms were obtained. The instantaneous frequency of these five waveforms was averaged, showing that this one thermally controlled ring was

able to achieve about 28 kHz of chirp as shown in Fig. 64. Comparison of Fig. 64 with Fig 56a shows that this chirp is similar in form to half of one simulated NLFM waveform.

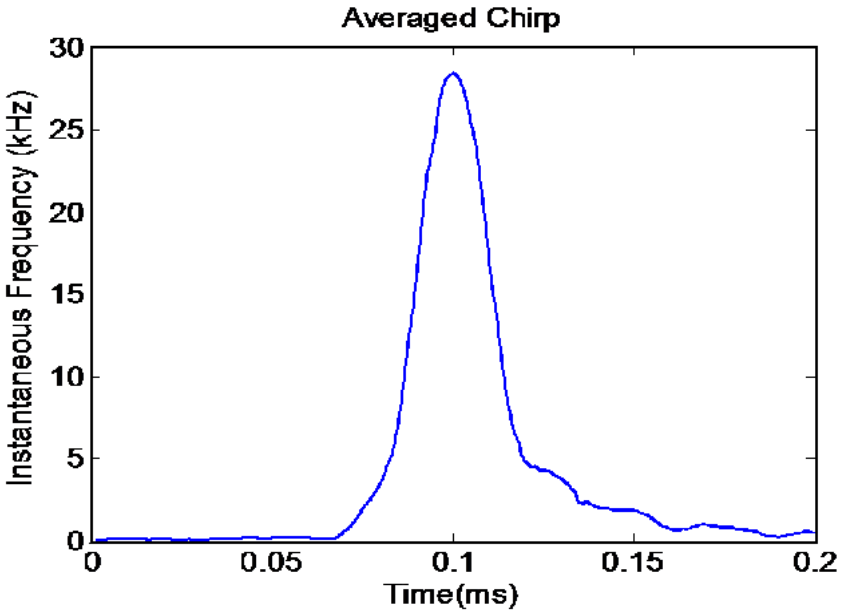

Fig. 64 Instantaneous frequency chirp created by the Si3N4 tunable integrated ring resonator. A peak frequency of 28kHz was achieved.

CHAPTER IX

SIGNAL PROCESSING APPLICATION 4:

PULSE COMPRESSION VIA GROUP DELAY FILTERING

A. Introduction

The use of frequency chirped waveforms in laser radar (ladar) systems has been a common practice for many years now [44]-[51]. Chirped waveforms allow for greater temporal localization of the return waveform leading to a better range resolution in the system. This improved range resolution is achieved by compressing the waveform, either in the optical domain or electrical domain. For power limited systems, waveform compression also gives the added benefit of improving the signal-to-noise ratio (SNR) of the system by spreading the signal energy over a greater temporal width.

In order to maximize SNR generally matched filters are used. Frequently these are employed in the electrical domain, after coherent detection and analog-to-digital conversion. Although this method is quite functional, it requires the use of a coherent detector, which may not be desirable for some systems.

As opposed to matched filtering, it has been suggested to use frequency-delay or group-delay filters to compress chirped waveforms. Delay filters for pulse compression have been used in other non-ladar optical systems and also for radar.

Optical group-delay filtering may be accomplished by a variety of techniques including, chirped fiber-bragg gratings, dispersive fiber, optical ring resonators, and so forth. Integrated optical ring resonators in particular allow for a compact platform with a great deal of dynamic capability. As an added benefit, other ladar system elements

could also be incorporated into the same integrated chip. In this paper we explore how integrated optical ring resonators could be used to create group delay filters that will compress frequency chirped optical waveforms.

B. Theoretical Review

With the proper adjustment of coupling constants and feedback phase of several rings, many different group delay responses can be approximated. The principle concept of the group delay compression filter is to match the group delay response to the original chirp, aka. cause each frequency to delay such that all the energy of the signal compresses temporally. Figs. 65 and 66 show this process. In Fig. 65 a we see a constant amplitude linear chirp; the arrows show how much group delay each part of the signal requires for ideal compression. In fig. 65 b we see the corresponding group delay filter response to optimally compress this waveform. Fig. 66 a shows how such a filter could be approximated with 6 ideal 2.1 GHz FSR ring resonators. The specific ring coupling constants and round-trip phase offsets are listed in Table 1. And Fig. 66 b shows the chirped waveform amplitude before and after the approximately ideal group delay filter. Notice that there is an average delay of 4 ns between the peak amplitude of the compressed waveform as compared with the center of the original linear chirp. This is due to the requirement that the filter remain causal, i.e. group delays must be positive.

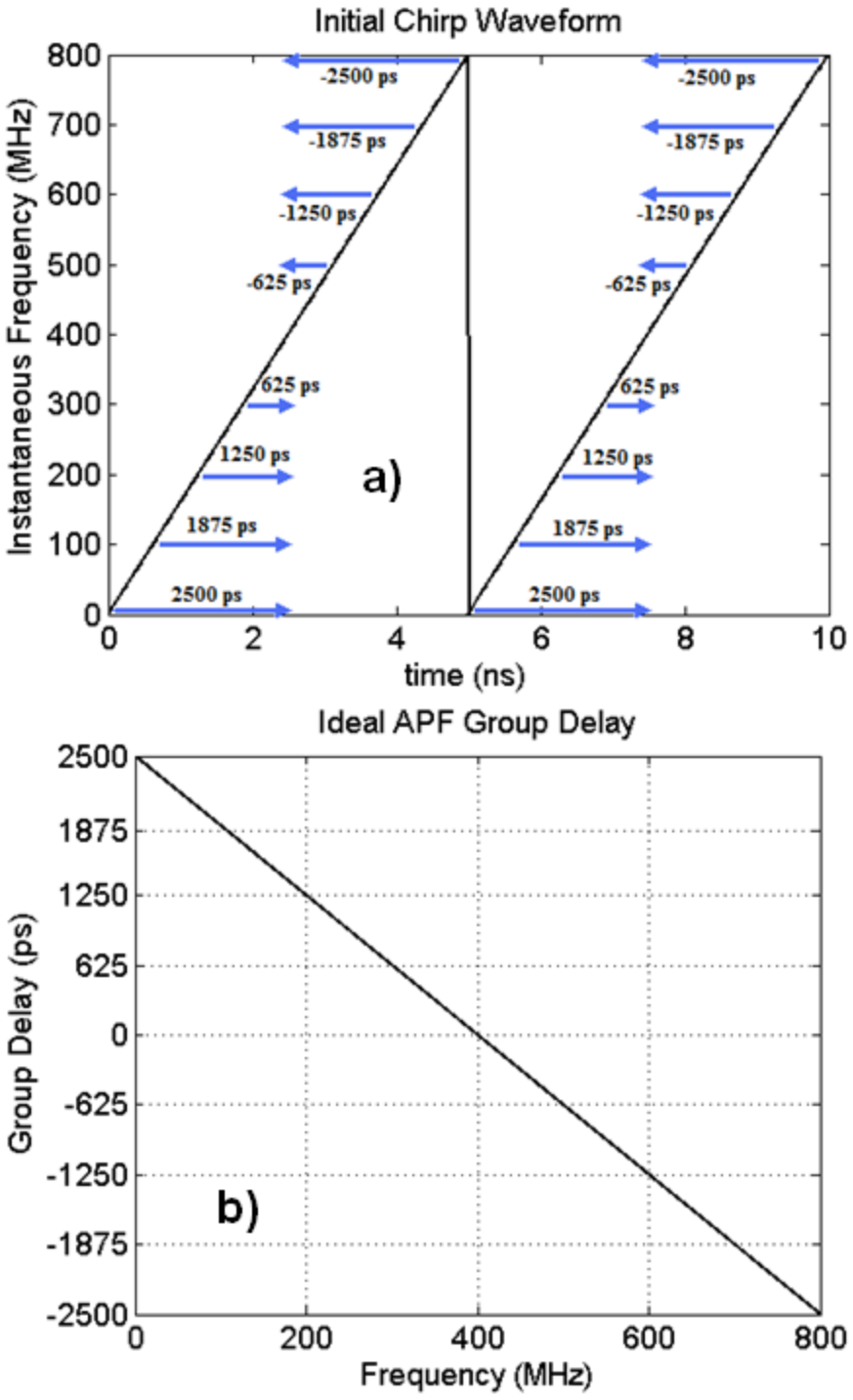

Fig. 65 Group delay compression principle. a) An ideal linear chirp. b) The corresponding ideal group delay filter to compress the linear chirp.

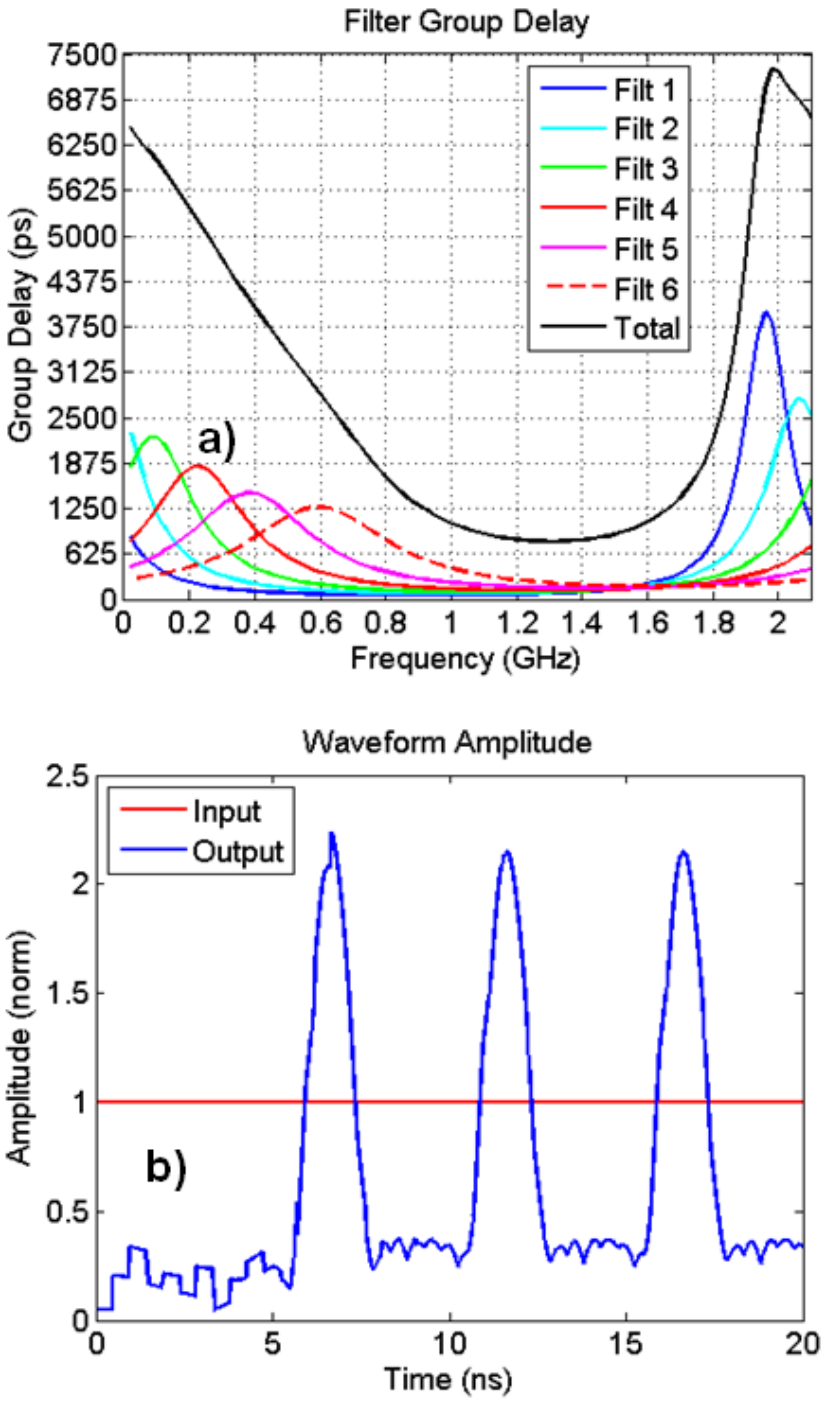

Fig. 66 a) Group delay response of six ideal 2.1GHz FSR rings with coupling constants and feedback phase adjusted to approximate the ideal group delay filter shown in Fig. 65 b. b) The amplitude response both before and after the group delay filter.

Table 1. Coupling constants and Phase offsets of ring resonators shown in Fig. 65 a.

Filter #	Coupling κ=	Phase Offset
1	0.382	-0.120*pi
2	0.500	-0.023*pi
3	0.578	0.095*pi
4	0.655	0.225*pi
5	0.741	0.375*pi
6	0.794	0.575*pi

C. Simulations

The following simulations all used (4.15) as the description of each ring and assumed no loss ($\gamma = 1$). The principle idea is to take a given chirp and approximate the group delay filter to it using optimization.

C.1 Chirp pattern and filtering solutions

One important consideration is the pattern of chirps as this filtering process is usually done on a series of chirps. The chirps may follow a sawtooth pattern or a triangular pattern depending on the system and application (see Fig. 67). Interestingly when a triangular patter of chirps is passed through the group delay filter, only half of the chirps are compressed; the other half are spread temporally (see Fig 68).

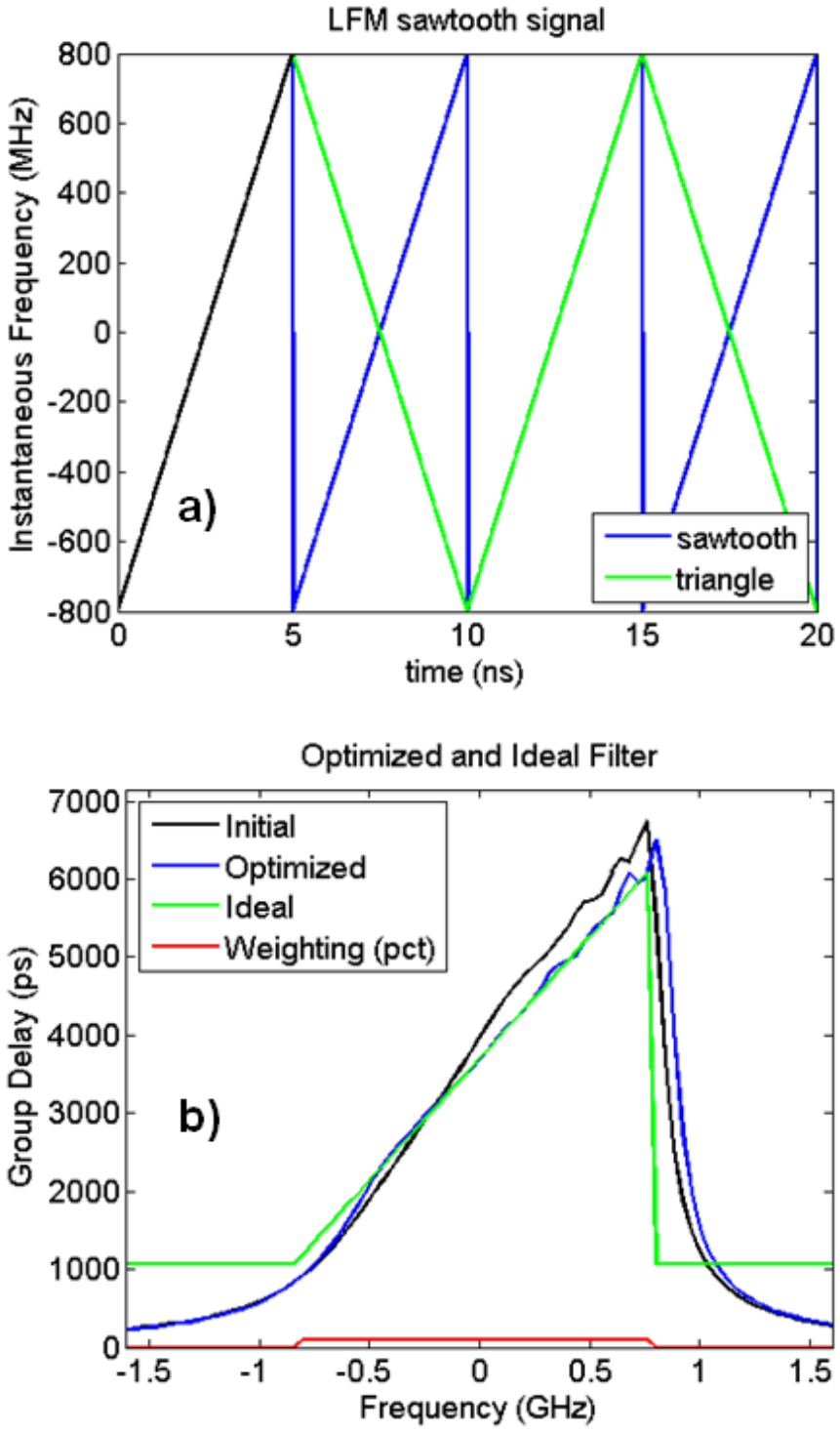

Fig. 67 a) Triangle vs. sawtooth chirp pattern. b) Optimized group delay filter response.

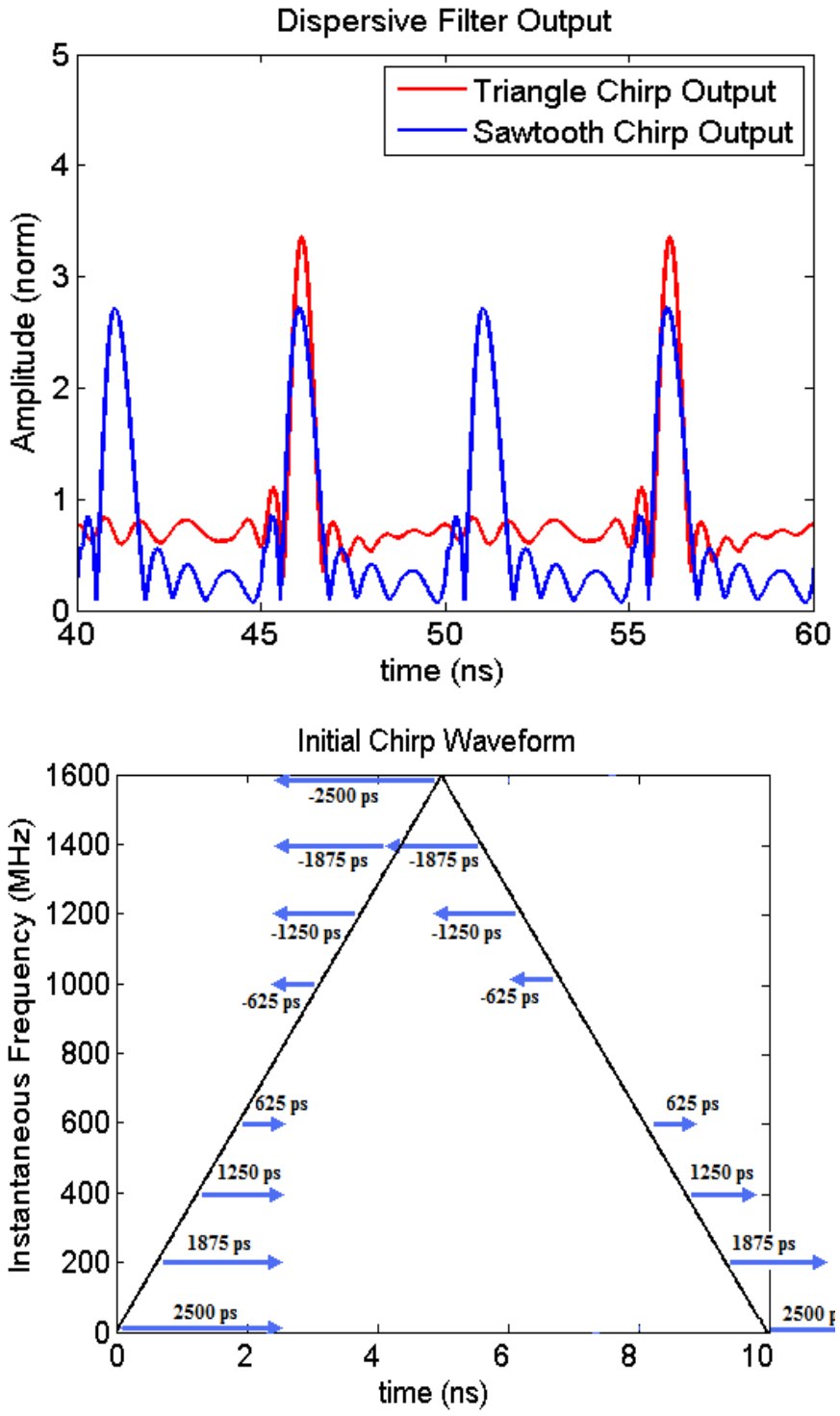

Fig. 68 a) Group delay filter output. b) Illustration of triangle chirp response.

There are two main methods to adjust for this temporal spreading. The first obvious solution is to only use the system with sawtooth chirp patterns. The second method is to design two separate optical filters, one for the positively sloped chirps and one for the negatively sloped chirps, and perform subtraction after photodetection (see Fig. 69). As we shall see this second method seems to reduce sidelobe levels in the detected signal, but comes at a cost of reducing the optical signal power by half (one half for each filter). For systems that are noise limited by sidelobe level this is acceptable however.

C.2 Linear chirp compression

The current standard technique for pulse compression is matched filtering; therefore the output of the group delay filter will be compared against an ideal matched filter. Figs. 70 and 71 show the results for a linear chirp with a bandwidth $B = \pm\frac{4}{T}$ where T is the time taken for one chirp. Six rings were used in this simulation; and as a general rule of thumb, for good results:

$$N_{rings} \geq 0.75 * BT \qquad 9.1$$

although fair results can be still be achieved if one ring is used per 2 units of time-bandwidth product.

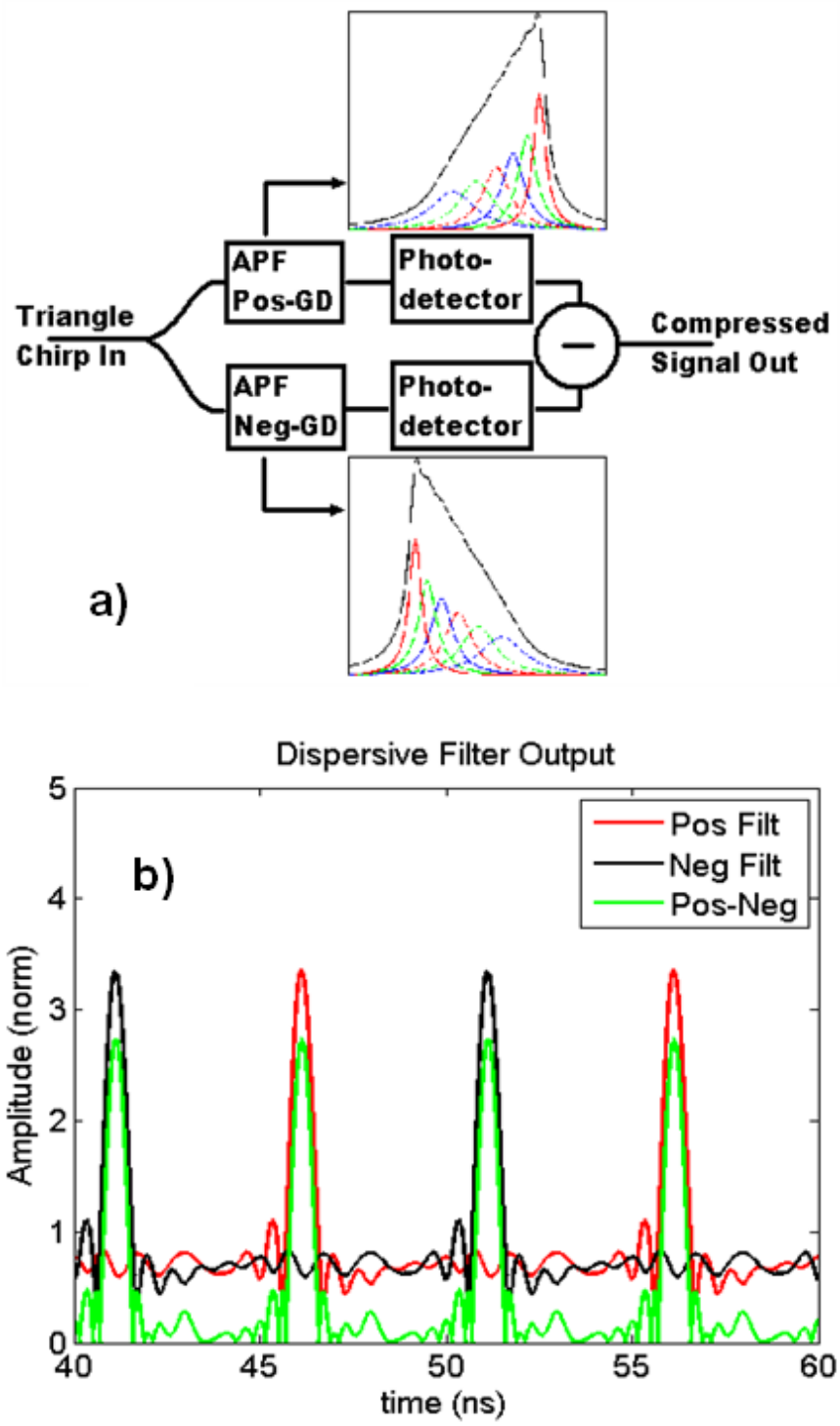

Fig. 69 a) Schematic of triangle chirp group delay filters one with a positive slope and one with a negative slope. b) Output of triangle chirp compression filters alone and after subtraction.

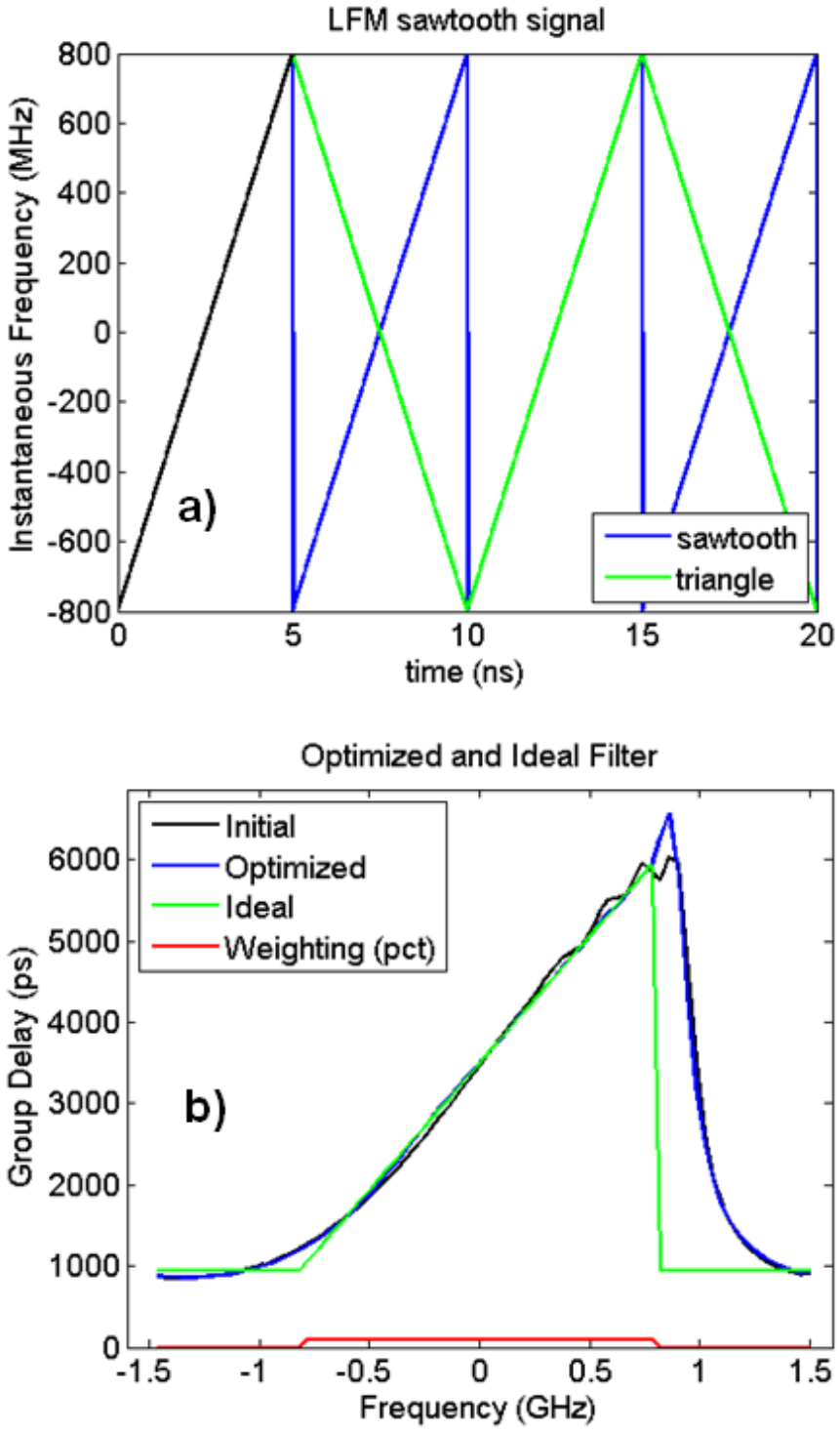

Fig. 70 Group delay filter response for a linear chirp with a bandwidth B=±4/T where T is the duration of a single chirp. a) Chirp waveform. b) Group delay filter response.

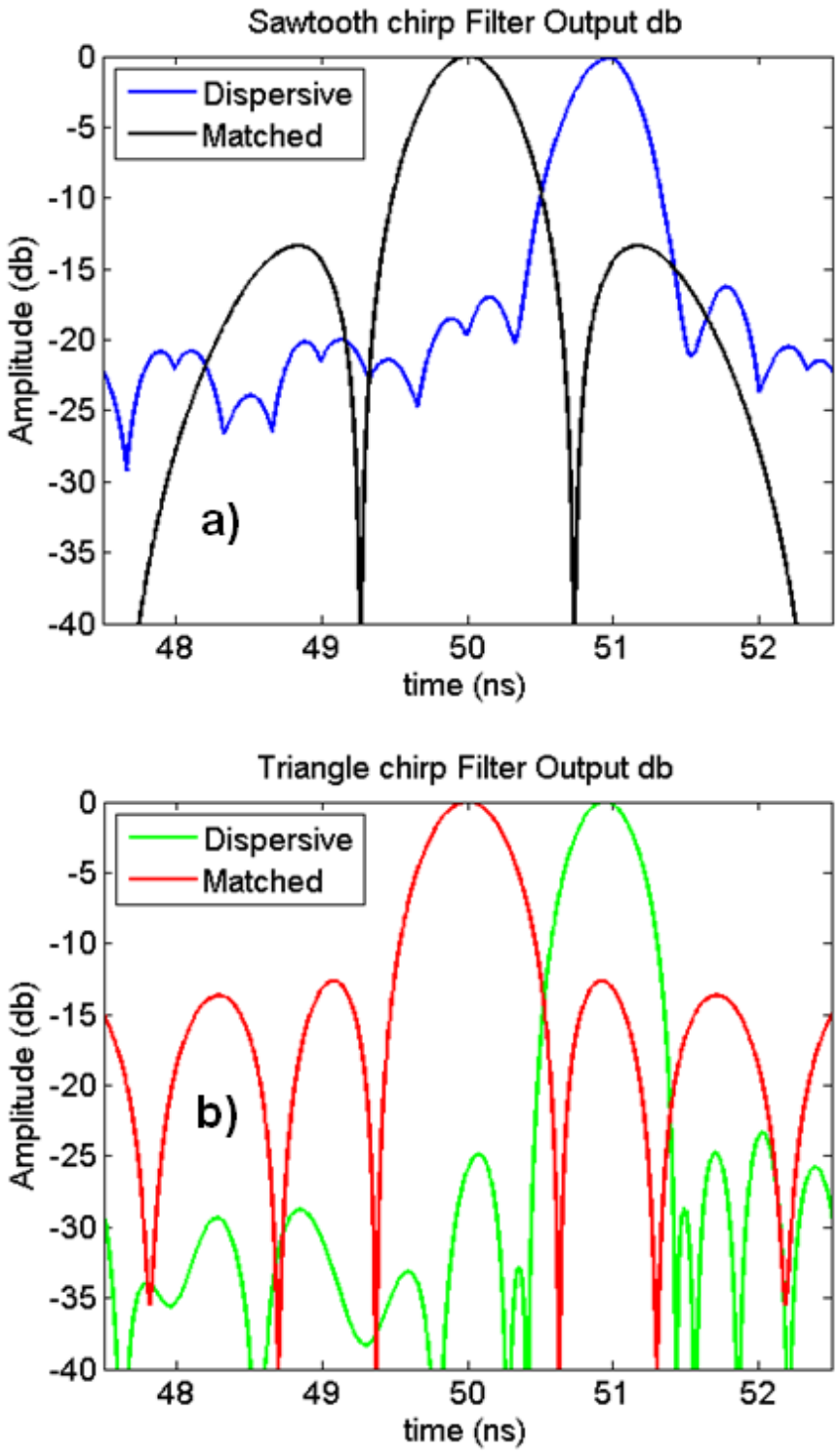

Fig. 71 Group delay filter output for a linear chirp with a bandwidth B=±4/T where T is the duration of a single chirp vs. an ideal matched filter output in decibles for: a) a sawtooth chirp pattern, b) a triangle chirp pattern.

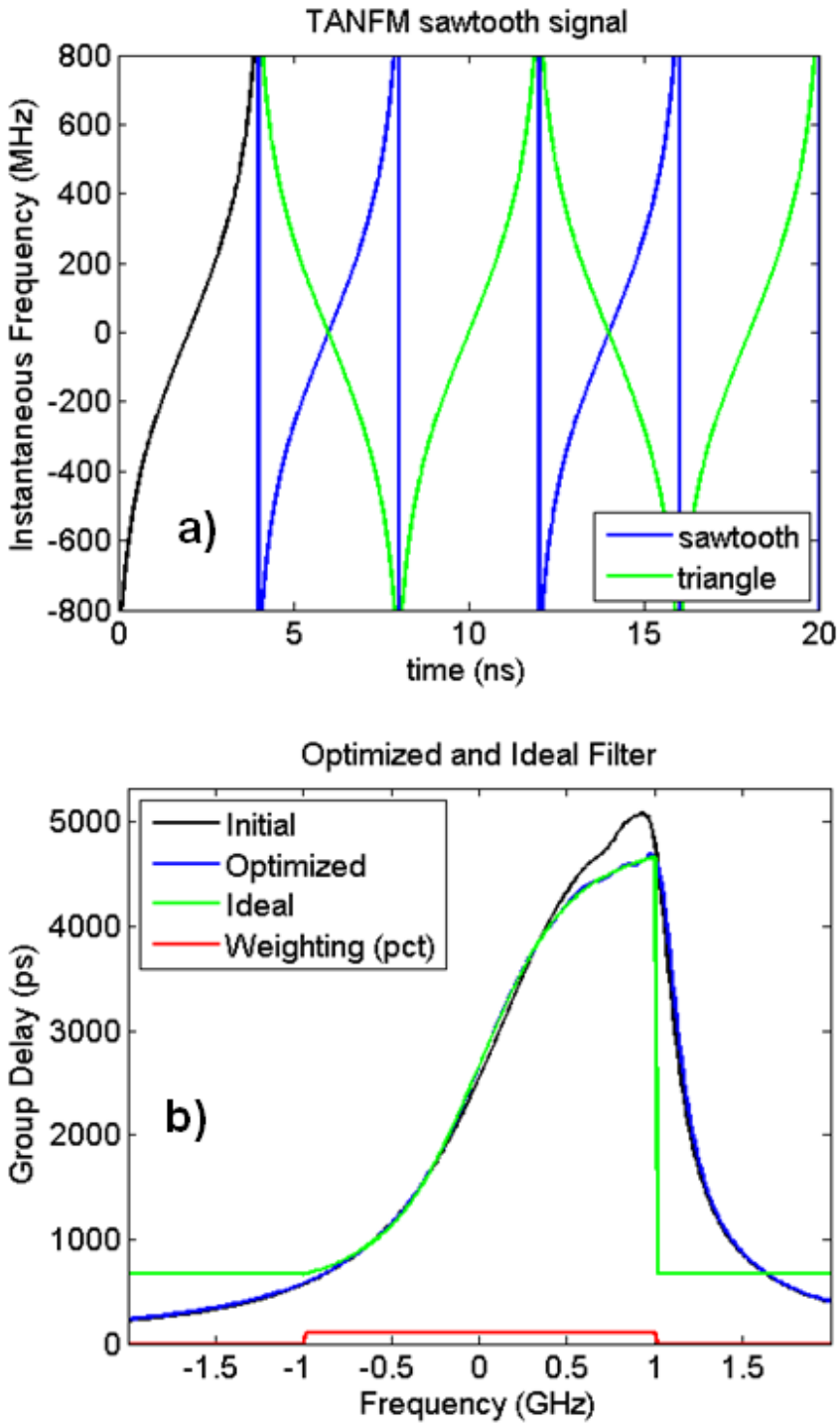

Fig. 72 Group delay filter response for a non-linear chirp with a bandwidth B=±4/T where T is the duration of a single chirp. a) Chirp waveform. b) Group delay filter response.

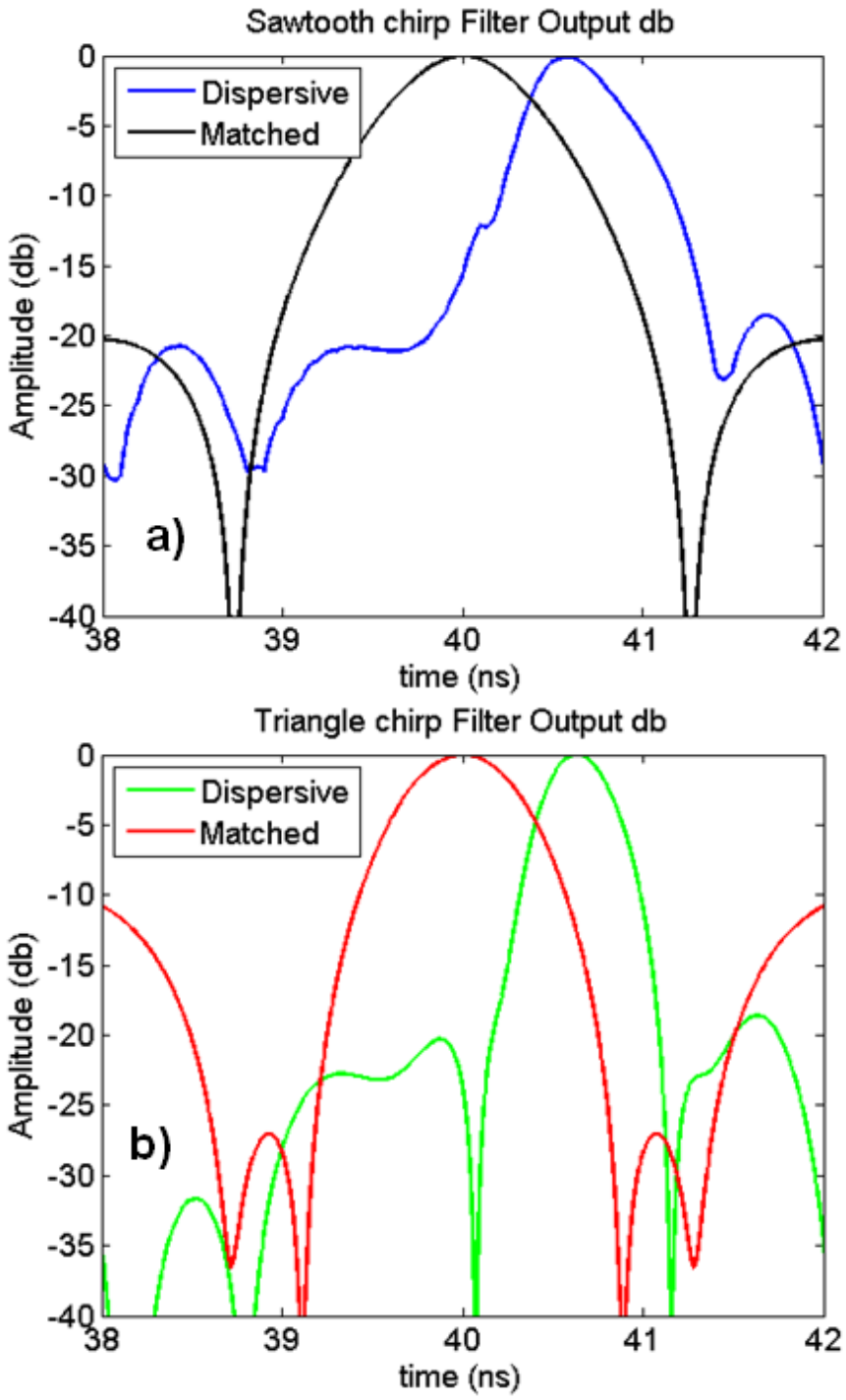

Fig. 73 Group delay filter output for a non-linear chirp with a bandwidth B=±4/T where T is the duration of a single chirp vs. an ideal matched filter output in decibles for: a) a sawtooth chirp pattern, b) a triangle chirp pattern.

C.3 Non-linear chirp compression

Some research lately has explored the possibility of non-linear chirps for laser radar systems, with encouraging results [44]-[51]. Chirp linearity is not a requirement for group delay based pulse compression. Figs. 72 and 73 show the group delay pulse compression results for the tan-FM chirped waveform [49]. Again the chirp patterns passed through a group delay filter exhibited narrower mainlobes and lower or equivalent sidelobes as compared to chirp patterns passed through ideal matched filters.

C.4 Larger bandwidth chirp compression

The same principle works for chirps with larger bandwidths. In this simulation a non-linear chirp with a bandwidth $B = \pm\frac{10}{T}$ was used, and 15 rings were used to approximate the ideal group-delay response. This time the benefit to the sidelobes is readily apparent (see Figs. 74–75). For both the sawtooth and triangular chirp patterns the sidelobe levels of the group delay filter outputs were equivalent or lower than the equivalent matched filter outputs. And once again, the mainlobe width is smaller.

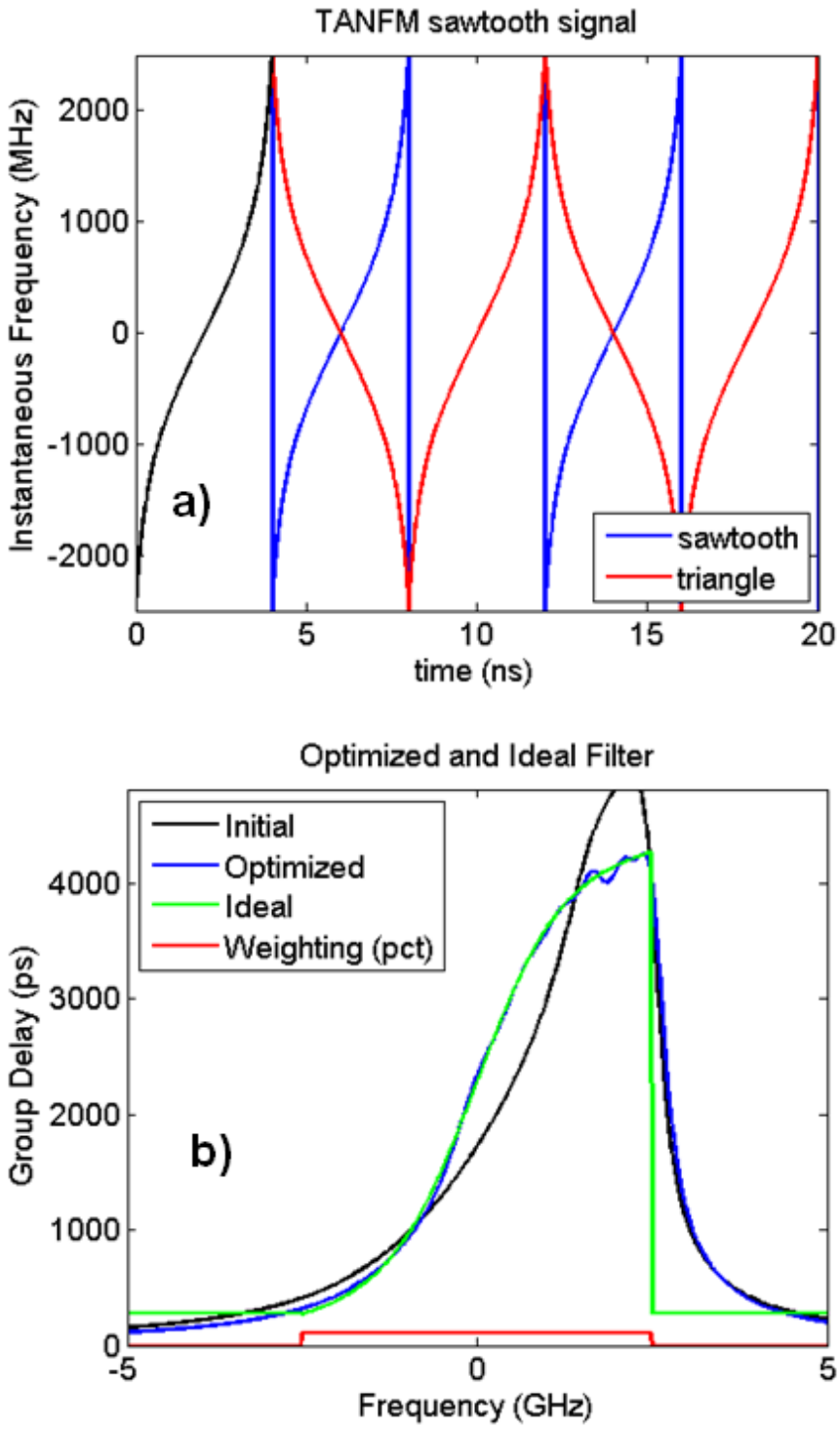

Fig. 74 Group delay filter response for a non-linear chirp with a bandwidth B=±10/T where T is the duration of a single chirp. a) Chirp waveform. b) Group delay filter response.

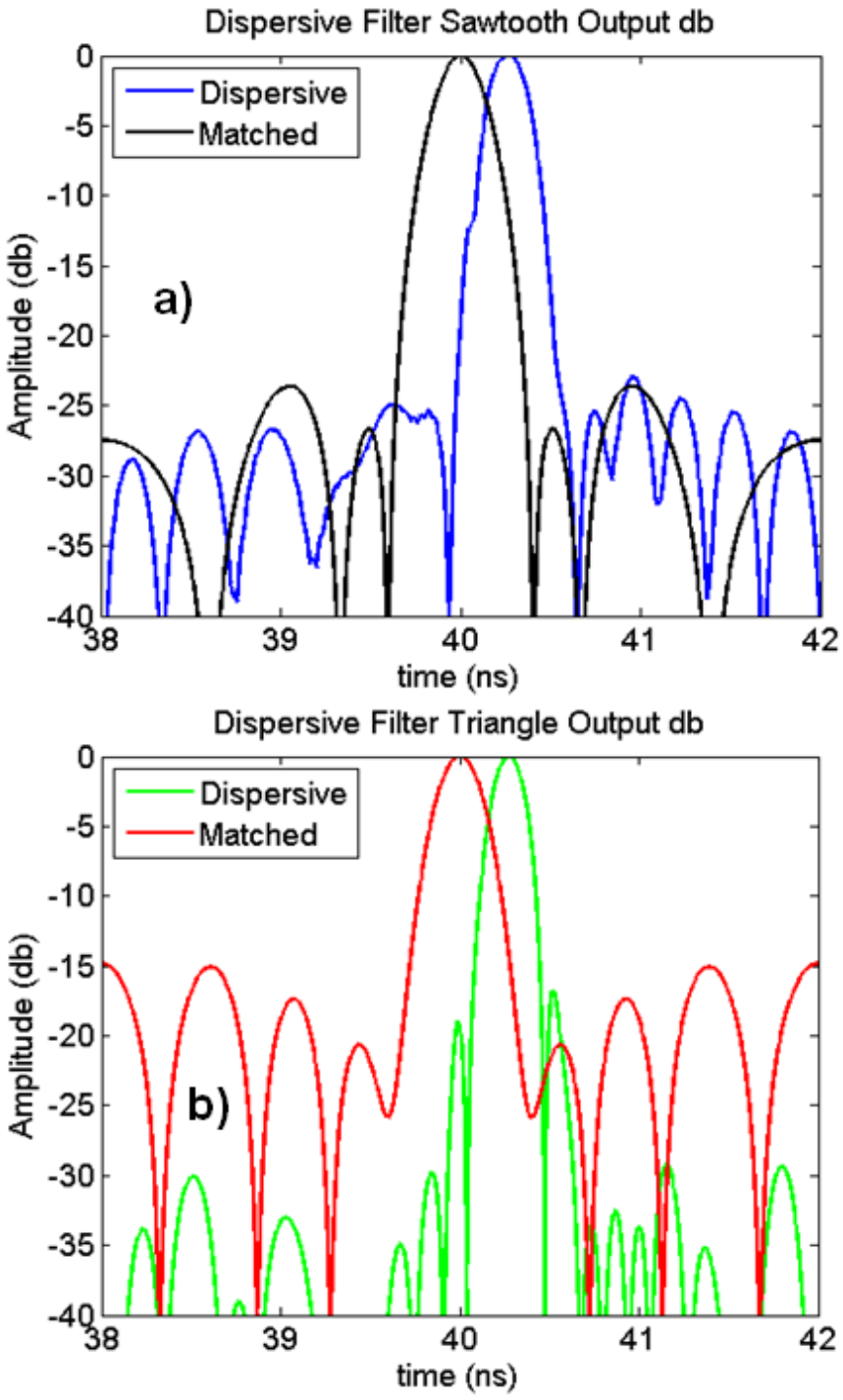

Fig. 75 Group delay filter output for a non-linear chirp with a bandwidth B=±10/T where T is the duration of a single chirp vs. an ideal matched filter output in decibles for: a) a sawtooth chirp pattern, b) a triangle chirp pattern.

C.5 Coupling and phase tolerance simulation

Close examination of the optimized group delay filters begs the question, how closely do the coupling constants and phase offsets need to be to their optimized values to allow for good compression? These simulations aim to answer this question. Each rings coupling constant and phase offset will be slightly offset in a random manner, and the resulting mainlobe width and sidelobe level of the output wave will be plotted on a scatter plot. The results for 1000 runs with offsets of 0.1%, 0.5%, and 1% can be seen in Figs. 76 and 77 for LFM and NLFM optimized group delay filters, all with a bandwidth of 4/T.

Clearly the mainlobe widths and sidelobe levels remain accurate for 0.1% and 0.5% random offset to the coupling constants and phase offsets. At 1% however the output signal performance degrades for the most part. Therefore it can be reasonably concluded that both the coupling constant and phase offset of each ring needs to be controlled to within 0.5% of its optimized value for acceptable system performance.

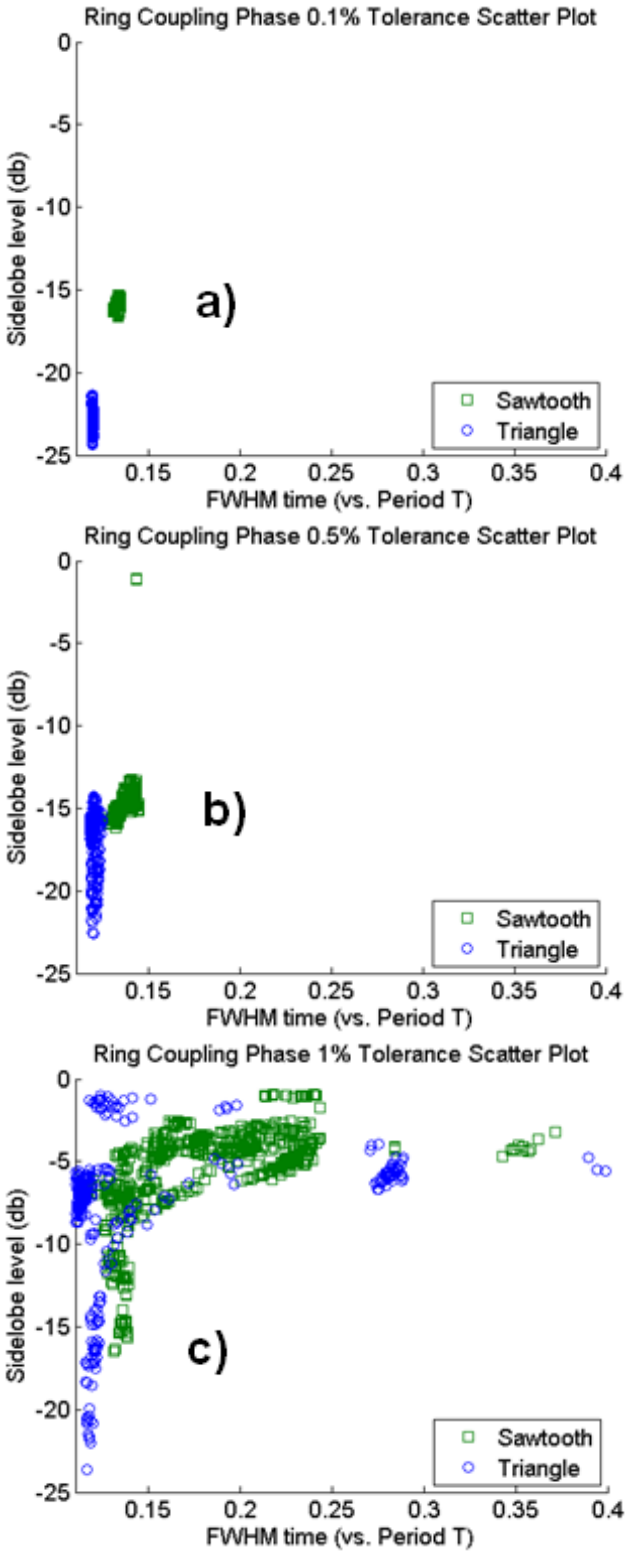

Fig. 76 LFM optimized group delay filter tolerance scatter plots for random coupling and phase offsets of: a) 0.1% b) 0.5% c) 1%.

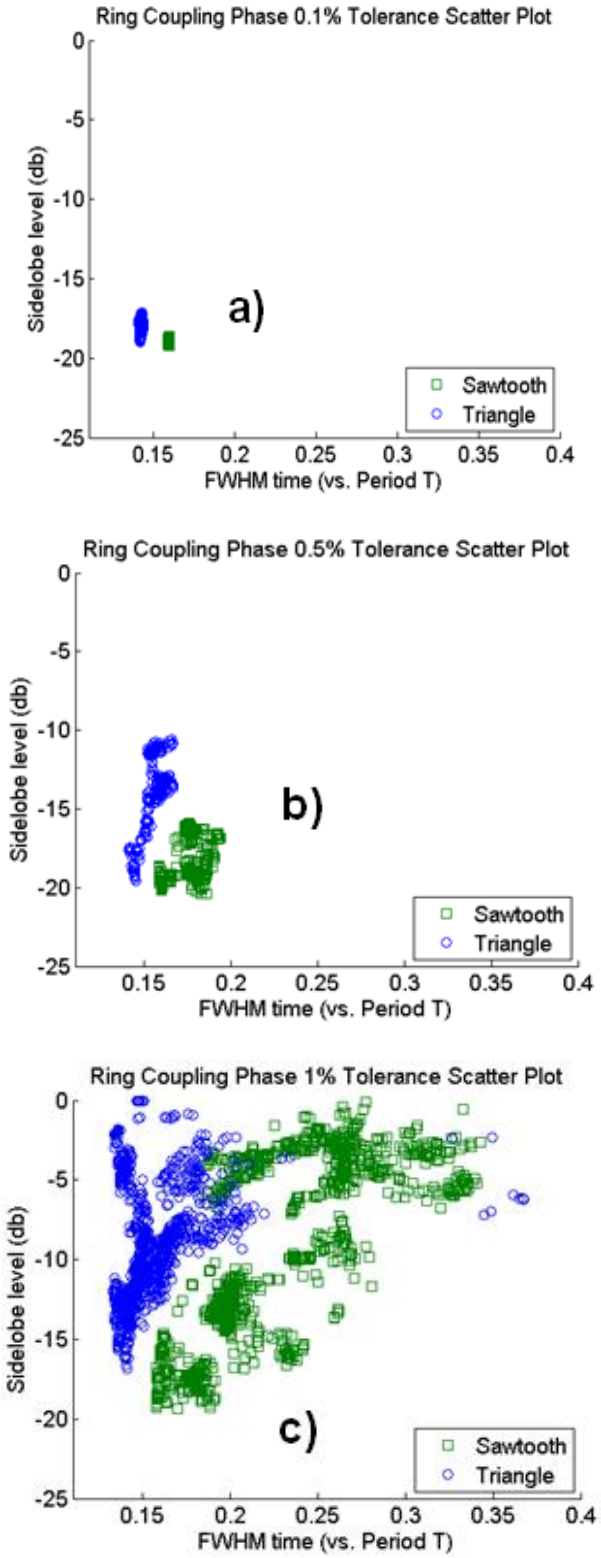

Fig. 77 **N**LFM optimized group delay filter tolerance scatter plots for random coupling and phase offsets of: a) 0.1% b) 0.5% c) 1%.

D. Proof of Concept Experiment

This experiment has been designed to show that tunable integrated optical ring resonators can produce an amplitude variation in constant amplitude frequency modulations. The experimental setup is shown in Fig. 78. This experiment will use six of the thermally controlled silicon-nitride rings in the found in the dynamic dispersion compensator (described in Chapter VI). Each ring has an FSR of 50GHz. The group delay and amplitude response of the rings was measured using the group delay measurement system (described in Chapter V). Each ring was set to have about 230 ps of peak group delay ($= \frac{11.5}{FSR}$ for a 50 GHz FSR) (see Fig 79a). Additionally each ring was found to have about 0.11 db/roundtrip of loss (see Fig 79b).

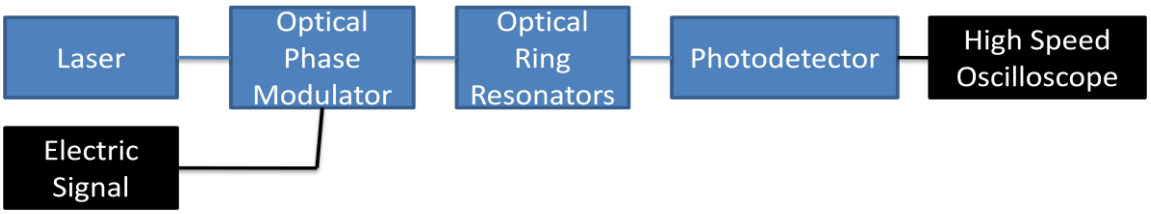

Fig. 78 Group delay compression filter proof-of-concept experimental setup.

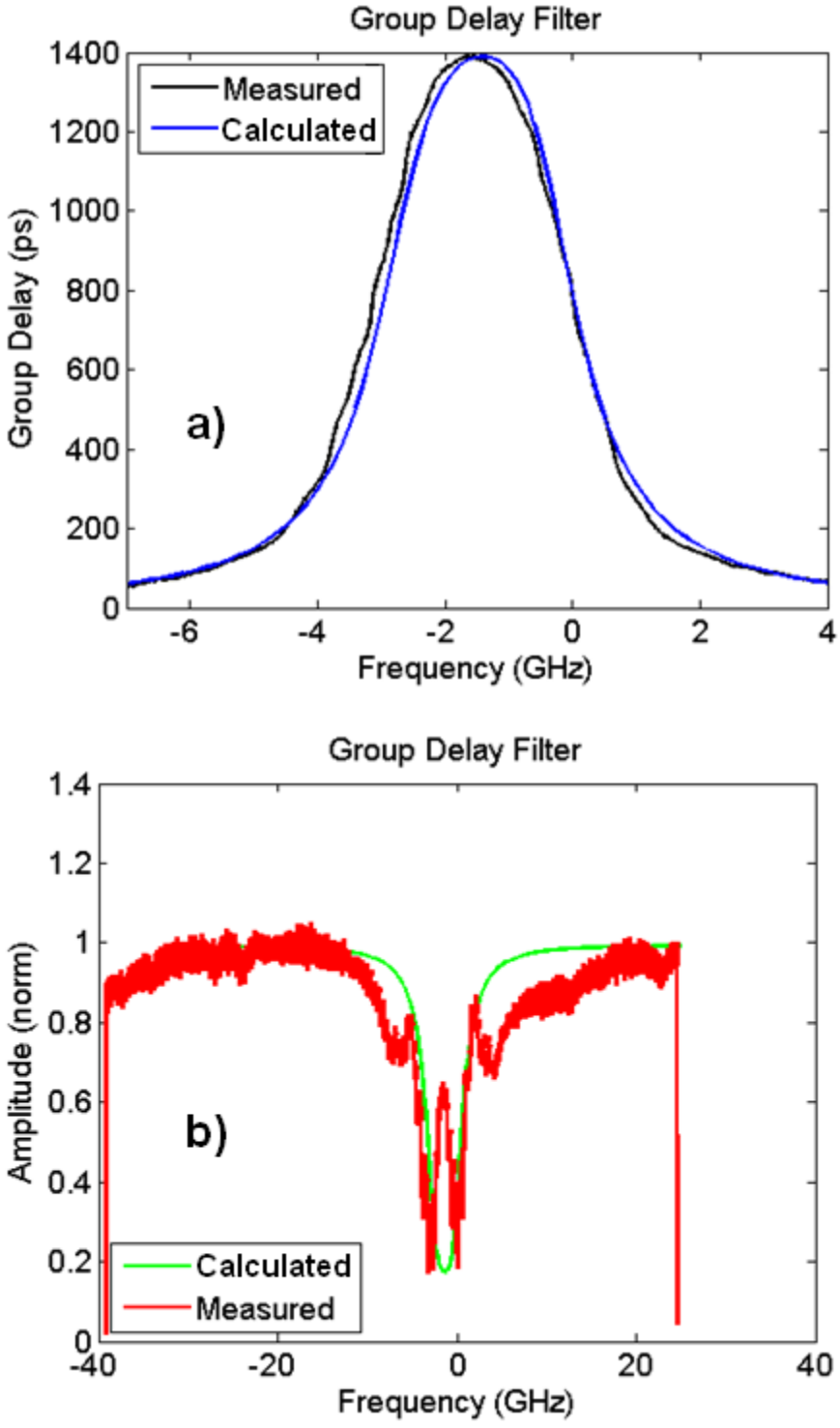

Fig. 79 a) Measured and calculated group delay response of all six optical ring resonators. b) Measured and calculated amplitude response of all six optical ring resonators.

There are two requirements to do an experiment like this which reach towards each other: producing a large chirp and/or producing a high amount of group delay. With such high FSR ring not much group delay was possible (only 1400 ps). This translates into a short pulse times (T<1.4 ns) and at these high speeds large bandwidth chirps were hard to produce. ($B \approx \frac{1}{T} \approx 1\ GHz$) Because of this low chirp bandwidth the chirps weren't so much compressed as converted from phase modulation to amplitude modulation. Nonetheless fairly good results were obtained for such short pulse times ($0.5 \leq T \leq 0.833ns$). Figs. 80–82 show the output of the ring resonators, as compared to the un-filtered chirps.

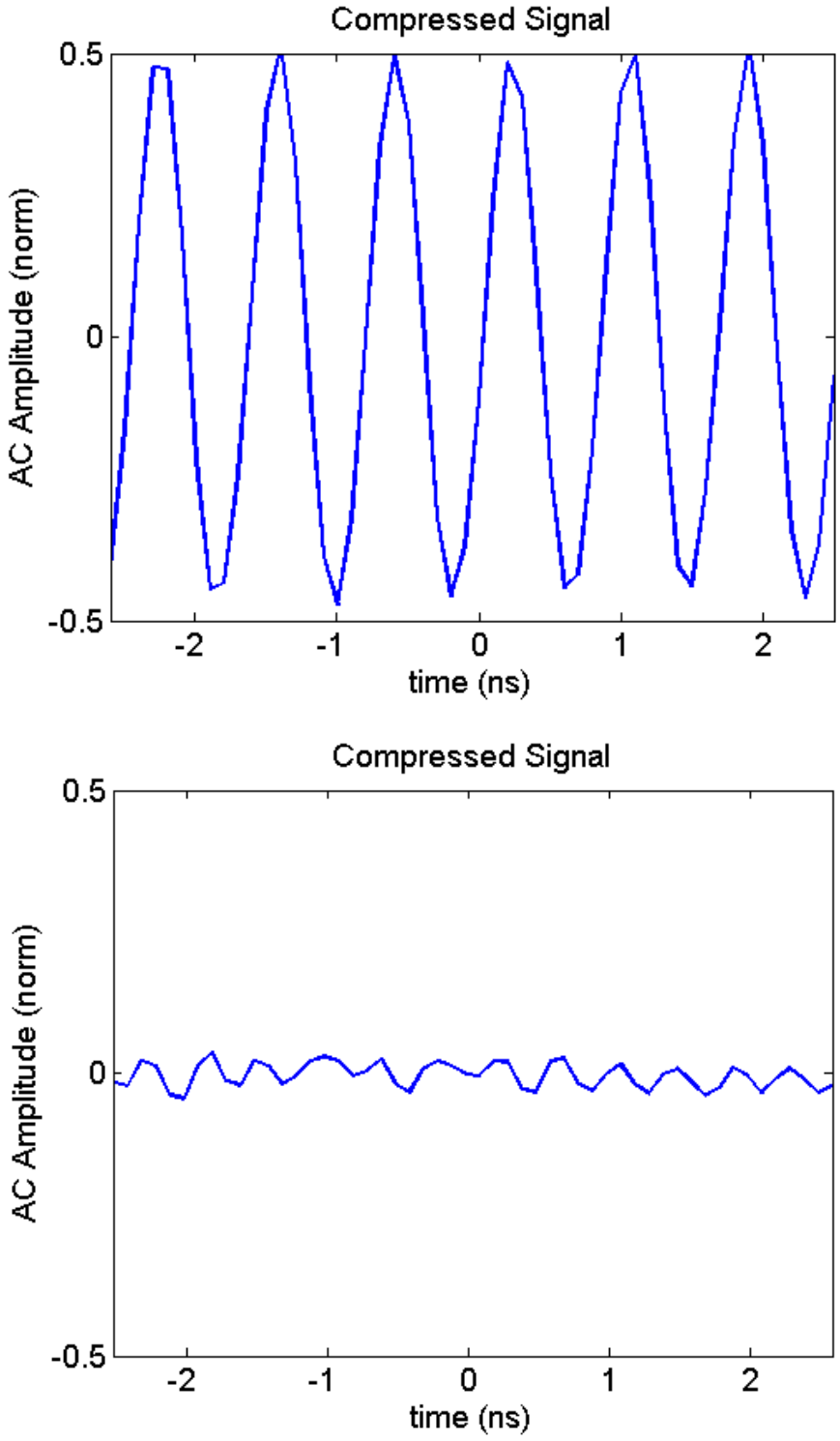

Fig. 80 a) Group delay filtered chirp output amplitude for chirp period T = 0.833ns. b) Unfiltered chirp output amplitude.

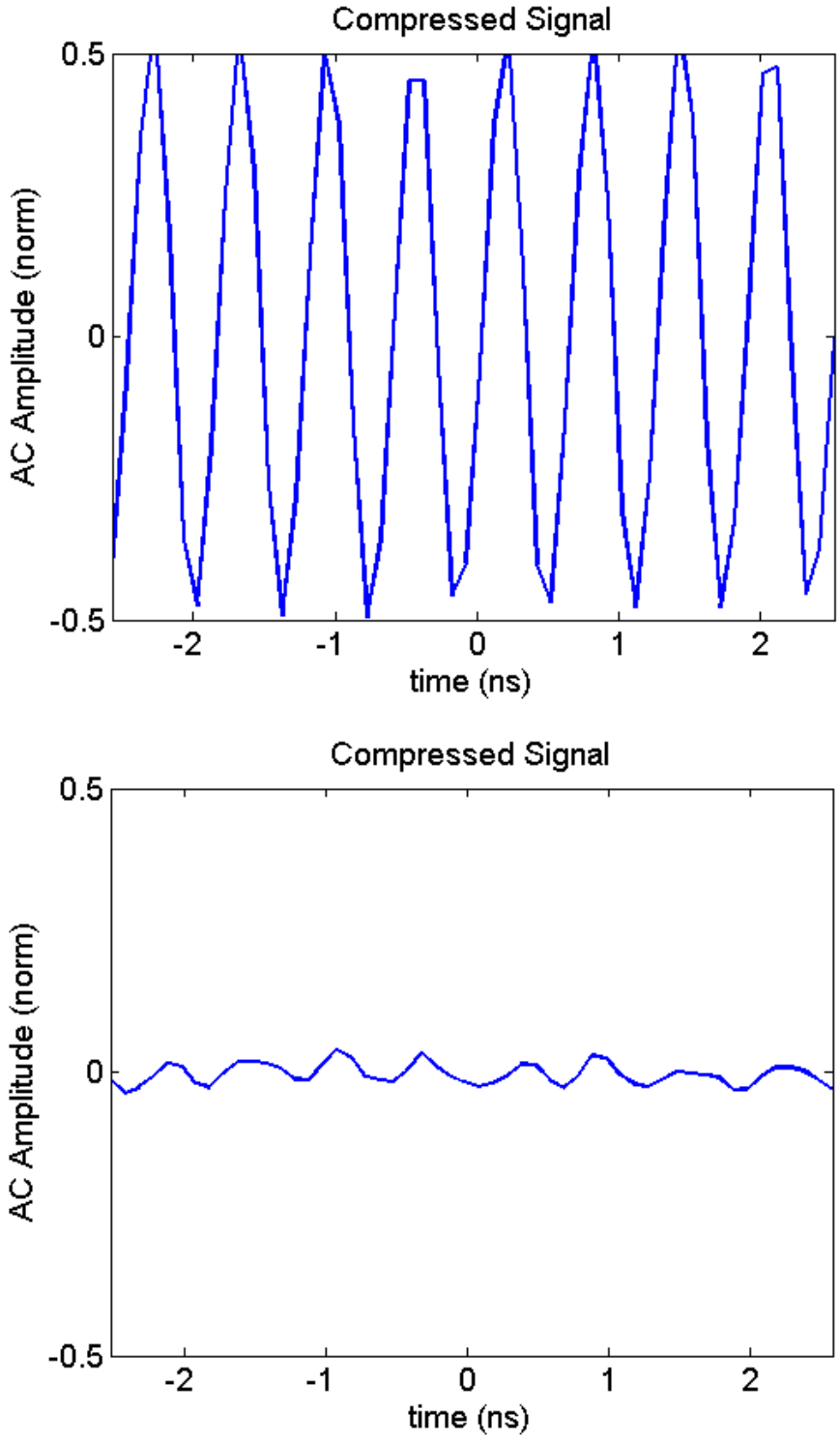

Fig. 81 a) Group delay filtered chirp output amplitude for chirp period T = 0.667ns. b) Unfiltered chirp output amplitude.

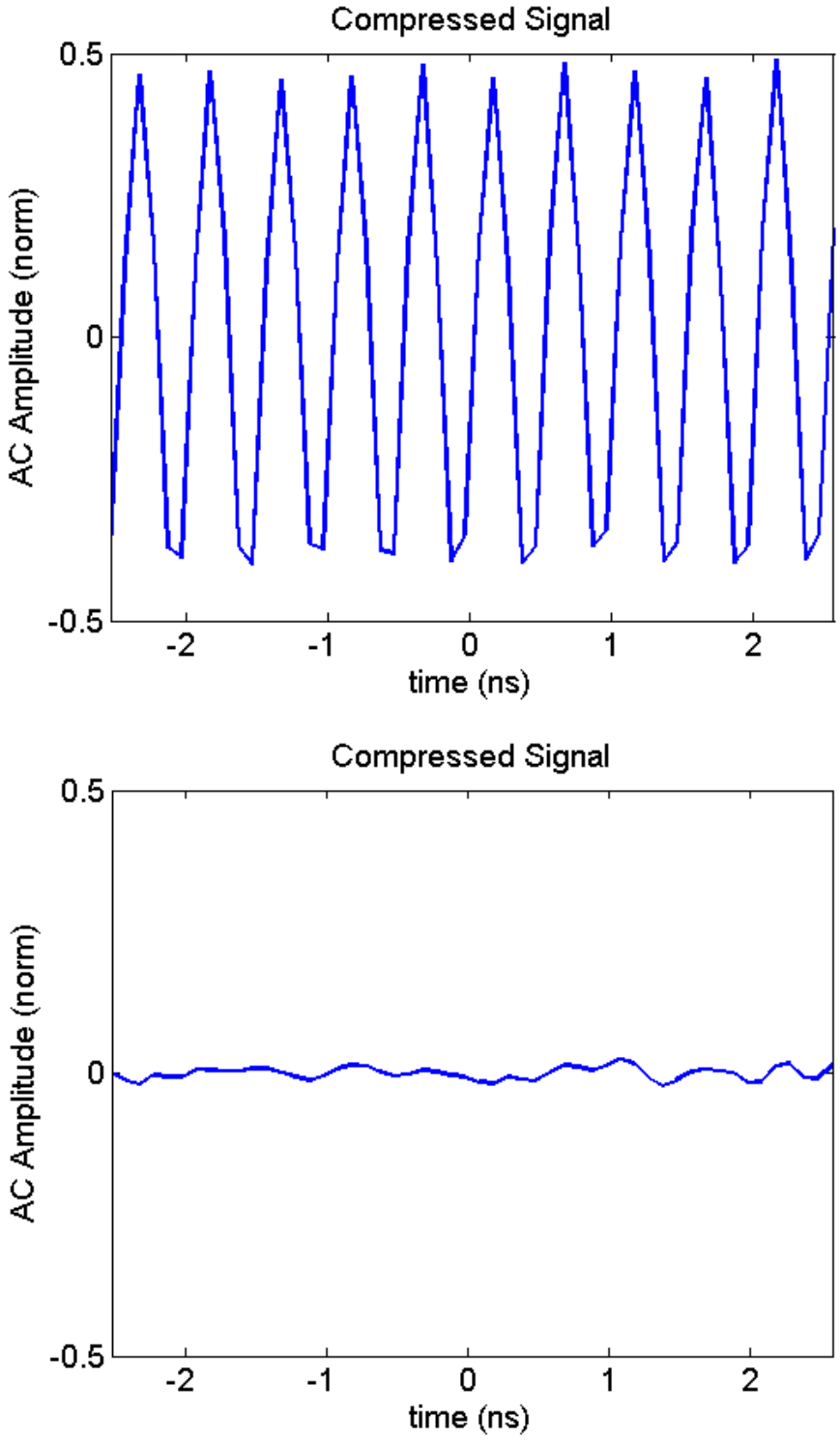

Fig. 82 a) Group delay filtered chirp output amplitude for chirp period T = 0.5ns. b) Unfiltered chirp output amplitude.

CHAPTER X

CONCLUSION

A. Future of Integrated Optical Ring Resonators

This work has explored three of the many applications of integrated optical ring resonators through simulation and proof-of concept experiment only. Although simulation and proof-of concept experiments are very instructive in describing necessary device parameters, current system capabilities are principally controlled by fabrication techniques. In other words, the majority of future research for integrated optical ring resonators lies in device fabrication.

There are many areas of fabrication technology that could be improved through continued research. These include: improving waveguide loss and minimum bend radius; exploring other refractive index effects such as charge carrier injection or the electro-optic effect; increasing the number of devices on a single integrated chip; incorporating gain and/or polarization control into device functionality; and so forth. Many of these areas are already under intense investigation.

As knowledge of ring resonator devices increases and state-of-the-art manufacturing technologies improves, there will be a greater number of novel devices with increased flexibility and a higher level of integration. The application space for such devices is almost endless.

B. Further Research: Dynamic RF Phase Shifter

As said in the previous section, the majority of future research of the dynamic RF phase shifter lies in fabrication technology. This application would benefit greatly from

device miniaturization, as most applications will require quite a few phase controllers. Devices that use a faster refractive index changing effect would lead to faster transition times for the beamsteering network as a whole. Additionally the incorporation of photodetectors or even the optical source onto a single chip would also be highly desirable from a system engineering standpoint.

Perhaps the simplest and most important improvement would be lower loss waveguides. As discussed previously, waveguide loss leads to ring round-trip loss, and this in turn creates notches in the ring's amplitude spectrum. Because phase shifting is accomplished by shifting the spectrum of the ring, ring round-trip loss creates a phase-dependent loss in the final RF signal. Although reducing the waveguide loss is the best answer to the phase-dependent RF signal loss, an external optical or RF gain system could also be used for amplitude compensation. This likely is the most natural research to be pursued next for the RF phase shifter.

C. Further Research: LADAR Waveform Generation

Once again, the most important improvements to the LADAR waveform generation system all involve improved fabrication techniques. Most importantly, by far, is a faster refractive index tuning effect, preferably the electro-optic effect, because of its high speed and low optical loss. Also incorporating more rings will increase the chirp bandwidth, which in turn improves system performance.

D. Further Research: Pulse Compression via Group Delay Filtering

Not surprisingly, the most important research yet to be done on the group-delay compression filters involves fabrication. A platform with low round-trip loss, low FSR

rings is vital to the functionality of this system. Additionally, with such tight tolerances on both ring coupling and spectral phase location, a system with tunable phase and coupling is highly desirable, if not necessary, to adequate system performance.

Depending on the speed of the refractive index effect, a combined waveform generation and group-delay based compression system could also be designed that would be able to change bandwidth and period dynamically to suit system requirements.

One important part of many LADAR systems, for which the group-delay compression system may be used, is the ability to detect Doppler shift. The previous research didn't address this requirement. A solution could be sought in several ways. First, the generated waveform's chirp bandwidth and period could be varied, and the group-delay filter response also, to detect Doppler shift rather than time of flight. Second, an additional laser source or detector could be incorporated to help with Doppler shift detection. This yet remains an open research topic.

REFERENCES

[1] S. Ramachandran, "Introduction and overview," in *Fiber Based Dispersion Compensation*, New York: Springer, 2007, pp. 1–6.

[2] C. Lin, H. Cogelnik, and L. G. Cohen, "Optical-pulse equalization of low-dispersion transmission in single-mode fibers in the 1.3–1.7-μm spectral region," *Optics Letters*, vol. 5, no 11, pp. 476-478, Nov. 1980.

[3] F. Ouellette, "Dispersion cancellation using linearly chirped Bragg grating filters in optical waveguides," *Optics Letters*, vol. 12, no. 10, pp. 847-849, Oct. 1987.

[4] J. P. Gordon, and R. L. Fork, "Optical resonator with negative dispersion," *Optics Letters*, vol. 9, No. 5, pp.153-155, May 1984.

[5] D. Rafizadeh, J. P. Zhang, S. C. Hagness, A. Taflove, K. A. Stair, and S. T. Ho, "Waveguide-coupled AlGaAsyGaAs microcavity ring and disk resonators with high finesse and 21.6-nm free spectral range," *Optics Letters*, vol. 22, no. 16, pp. 1244–1246, Aug. 1997.

[6] J. C. Palais, *Fiber Optic Communications*, Upper Saddle River, NJ: Pearson Prentice Hall, 2005.

[7] C. K. Madsen and J. H. Zhao, *Optical Filter Design and Analysis: A Signal Processing Approach*, 1st. ed. New York: John Wiley & Sons, 1999.

[8] H. Nishihara, M. Haruna, and T. Suhara, *Optical Integrated Circuits*, New York: McGraw-Hill Book Company, 1989.

[9] R. F. Harrington, *Time-Harmonic Electromagnetic Fields*, New York: John Wiley & Sons, 2001.

[10] M. L. Calvo and V. Lakshminarayanan, ”Silicon waveguides for integrated optics,” in *Optical Waveguides: From Theory to Applied Technologies.* Boca Raton, FL : CRC Press, 2007, pp. 234–239.

[11] W. C. Tan, M. E. Solmaz, J. Gardner, R. Atkins, and C. K. Madsen, “Optical characterization of a-As2S3 thin films prepared by magnetron sputtering,” *J. Appl. Phys*. vol. 107, no. 3, pp. 033524–033524.6, Feb. 2010.

[12] J. F. Viens, C. Meneghini, A. Villeneuve, T. V. Galstian, E. J. Knystautas, M. A. Duguay, K. A. Richardson, and T. Cardinal, "Fabrication and characterization of integrated optical waveguides in sulfide chalcogenide glasses," *J. Lightw. Technol.,* vol. 17, pp. 1184–1191, 1999.

[13] M. E. Solmaz, D. B. Adams, S. Grover, W. Tan, X. Xia, O. Eknoyan, and C. K. Madsen, “First demonstration of an As2S3-on-LiNbO3 ring resonator;” *Optical Fiber Communcation Conf. and Expo*., Los Angeles, CA. 2009, pp. 1-3.

[14] D.G. Rabus, “Building blocks of ring resonator revices,” in *Integrated Ring Resonators: The Compendium.* Berlin, Germany: Springer, 2007, pp. 112–117.

[15] H.P. Weber and R. Ulrich, “A thin film ring laser.” *Appl. Phys. Lett*., vol. 19, no. 2, pp. 38–40 July 1971.

[16] A.S.H. Liao and S. Wang, “Semiconductor injection lasers with a circular resonator.” Appl. Phys. Lett., vol. 36, no. 10, pp. 801–803, May 1980.

[17] T.F. Krauss, P.J.R. Laybourn, and J. Roberts, “CW operation of semiconductor ring lasers,” *Electron. Lett*., vol. 26, no. 25, pp. 2095–2097, Dec. 1990.

[18] C. K. Madsen, G. Lenz, A. J. Bruce, M. A. Cappuzzo, L. T. Gomez, and R. E. Scotti, "Integrated all-pass filters for tunable dispersion and dispersion slope compensation*," IEEE Photonics Technol. Lett*., vol. 11, no. 12, pp. 1623-1625, Dec. 1999.

[19] D. M. Baney, B. Szafraniec, and A. Motamedi, "Coherent optical spectrum analyzer," *IEEE Photonics Technol. Lett*., vol. 14, no. 3, pp. 355-357, Mar. 2002.

[20] B. Szafraniec, A. Lee, J. Y. Law, W. I. McAlexander, R. D. Pering, T. S. Tan, and D. M. Baney, "Swept coherent optical spectrum analysis," *IEEE Trans. Instrum. Meas*., vol. 53, no. 1, pp. 203-215, Feb. 2004.

[21] D. Derickson, "Dispersion measurements," in *Fiber Optic Test and Measurement,* Upper Saddle River, NJ: Pearson Prentice Hall, 1998, pp. 482–485.

[22] B. Costas, D. Mazzoni, M. Puleo, and E. Vezzoni, "Phase shift technique for the measurement of chromatic dispersion in optical fibers using LED's," *IEEE J. of Quantum Electron*., vol. 18, no. 10, pp. 1509-1515, Oct. 1982.

[23] D. K. Gifford, B. J. Soller, M. S. Wolfe, and M. E. Froggatt, "Optical vector network analyzer for single-scan measurements of loss, group delay, and polarization mode dispersion," *Applied Optics*, vol. 44, no. 34, pp. 7282-7286 Dec. 2005.

[24] M. Froggatt, and B. Soller, "Establishing a known basis set for OVA measurements," LUNA Technologies, Blacksburg, VA, Tech. Rep. Apr. 2003.

[25] W. Shieh, "Principal states of polarization for an optical pulse," *IEEE Photonics Technol. Lett*., vol. 11, no. 6, pp. 677–679, Jun. 1999.

[26] B. Szafraniec, A. Lee, J. Y. Law, W. I. McAlexander, R. D. Pering, T. S. Tan, and D. M. Baney, "Swept coherent optical spectrum analysis," *IEEE Trans. Instrum. Meas*., vol. 53, no. 1, pp. 203–215, Feb. 2004.

[27] P. Kockaert, M. Peeters, S. Coen, Ph. Emplit, M. Haelterman, and O. Deparis, "Simple amplitude and phase measuring technique for ultrahigh- repetition-rate lasers," *IEEE Photon. Technol. Lett*., vol. 12, no. 2, pp. 187–189, Feb. 2000.

[28] N. Berger, B. Levit, and B. Fischer, "Complete characterization of optical pulses using a chirped fiber Bragg brating," *Opt. Commun*., vol. 251, no. 4-6, pp. 315–321, July 2005.

[29] J. Debeau, B. Kowalski, and R. Boittin, "Simple method for the complete characterization of an optical pulse," *Opt. Lett*., vol. 23, no. 22, pp. 1784–1786, Nov. 1998.

[30] C. K. Madsen, "A novel optical vector spectral analysis technique employing a limited-bandwidth detector," *EURASIP J. Appl. Signal Process*., vol. 2005, no. 10, pp. 1566–1573, 2005.

[31] D. R. Morgan and C. K. Madsen, "Wide-band system identification using multiple tones with allpass filters and square-law detectors," *IEEE Trans. Circuits Syst. I, Reg. Papers*, vol. 53, no. 5, pp. 1151–1165, May 2006.

[32] W. Chen, S. Chu, B. Little, J. Hryniewicz, D. Gill, O. King, F. Johnson, R. Davidson, K. Donovan, J. Gibson, H. Jiao, and G. Carter, "Compact, fullC-band, widely tunable optical dynamic dispersion compensators," *Optical Fiber Communcation Conf. and Expo*., Los Angeles, CA., 2006.

[33] J. Han, B.-J. Seo, S. Kim, H. Zhang, and H. R. Fetterman, "Single-chip integrated electro-optic polymer photonic RF phase shifter array," *J. Lightw. Technol.*, vol. 21, no. 12, pp. 3257–3261, Dec. 2003.

[34] M. Y. Frankel and R. D. Esman, "True time-delay fiber-optic control of an ultrawideband array transmitter/receiver with multibeam capability," *IEEE Trans. Microw. Theory Tech*., vol. 43, no. 9, pt. 1–2, pp. 2387–2394, Sep. 1995.

[35] M. Y. Frankel, P. J. Matthews, and R. D. Esman, "Fiber-optic true time steering of an ultrawide-band receive array," *IEEE Trans. Microw. Theory Tech*., vol. 45, no. 8, pt. 2, pp. 1522–1526, Aug. 1997.

[36] H. Zmuda, R. A. Soref, P. Payson, S. Johns, and E. N. Toughlian, "Photonic beamformer for phased array antennas using a fiber grating prism," *IEEE Photon. Technol. Lett*., vol. 9, no. 9, pp. 241–243, Sep. 1997.

[37] Y. Liu, J. Yang, and J. Yao, "Continuous true-time-delay beamforming for phased array antenna using a tunable chirped fiber grating delay line," *IEEE Photon. Technol. Lett*., vol. 14, no. 8, pp. 1172–1174, Aug. 2002.

[38] J. Yang, J. Yao, Y. Liu, and S. C. Tjin, "Continuous true-time-delay beamforming employing a tunable multiwavelength fiber ring laser source with equally increased or decreased wavelength spacing," *Opt. Eng*., vol. 42, No. 1, pp. 239–244, Jan 2003.

[39] J. LeGrange, A. Kasper, C.Madsen, M. Cappuzzo, E. Chen, A. Griffin, E. J. Laskowski, and M. Rasras, "Demonstration of an integrated, tunable high

resolution true time delay line," in *17th Annu. Meeting IEEE Lasers and Electro-Optics Society (LEOS 2004)*, vol. 2, pp. 790–791, Nov. 2004.

[40] M. S. Rasras, C. K. Madsen, M. A. Cappuzzo, E. Chen, L. T. Gomez, E. J. Laskowski, A. Griffin, A. Wong-Foy, A. Gasparyan, A. Kasper, J. Le Grange, and S. S. Patel, "Integrated resonance-enhanced variable optical delay lines," *IEEE Photon. Technol. Lett.*, vol. 17, no. 4, pp. 834–836, Apr. 2005.

[41] C. K. Madsen, "Compact solid-state variable optical delay line with a large continuous tuning range," *U.S. Patent 6 956 991*, Oct. 18, 2005.

[42] C. K. Madsen, M. Thompson, D. B. Adams, and M. Solmaz, "Boundless-range optical phase shifters and sideband reduction," presented at the *Optical Amplifiers and Their Applications/Coherent Optical Technologies and Applications Conf.*, 2006.

[43] B.-J. Seo and H. Fetterman, "True-time-delay element in lossy environment using EO waveguides," *IEEE Photon. Technol. Lett.*, vol. 18, no. 1, pp. 10–12, Jan. 2006.

[44] D. Youmans, "Coherent ladar imaging of the SEASAT satellite retro-reflector array using linear-FM chirp waveforms and pulse compression," *SPIE Laser Radar Tech. and Appl. XII*, vol. 6550, pp. 655004, 2007.

[45] J. Buck, A. Malm, A. Zakel, B. Krause, and B. Tiemann, "High-resolution 3D coherent laser radar imaging," *SPIE Laser Radar Tech. and Appl. XII*, vol. 6550, pp. 655002 2007.

[46] D. Youmans, "Coherent lidar imaging of dust clouds: waveform comparisons with the poly-phase (P4) modulation waveform," *Proc. SPIE Laser Radar Tech. and Appl. XIII*, Vol. 6950, pp. 695009, 2008.

[47] J.A. Johnston, and A.C. Fairhead, "Waveform design and doppler sensitivity analysis for nonlinear FM chirp pulses," *in IEE Proceedings F*, vol. 133, no. 2, pp 163 – 175, Apr. 1986.

[48] M. Luszczyk, "Numerical evaluation of ambiguity function for stepped non-linear FM radar waveform" *International Conf. on Microwaves, Radar & Wireless Communications*, pp 1164 – 1167, May 2006.

[49] T. Collins, and P. Atkins, "Nonlinear frequency modulation chirps for active sonar," Radar, Sonar and Navigation, *IEE Proceedings*, vol. 146, no. 6, pp 312 – 316, Dec. 1999.

[50] G. Zhiqiang, H. Peikang, and L. Weining, "Matched NLFM pulse compression method with ultra-low sidelobes," *European Radar Conference*, pp 92 – 95, Oct. 2008.

[51] D. Youmans, "Waveform comparison for coherent ladar imaging using a helicopter facet model target," *Proc. SPIE Laser Radar Tech. and Appl. XIV*, Vol. 7323, pp. 732304, 2009.

[52] Y. K. Chan, M. Y. Chua, and V. C. Koo, "Sidelobes reduction using simple two and tri-stages nonlinear frequency modulation (NLFM)," *Progress In Electromagnetics Research (PIER) 98*, pp 33 – 52, 2009.

[53] A. W. Doerry, “Generating precision nonlinear FM chirp waveforms,” *Proc. SPIE Radar Sens. Tech. XI*, vol 6547, pp. 65470D, 2007.

APPENDIX A

SIMULATION CODE

The simulations shown in this dissertation are comprised of several thousand lines of Matlab code. A complete listing of all code would be unwieldly and probably longer than the text itself. Therefore the code shown here has been reduced to two key samples.

The first piece of sample code is derived directly from the equations shown in Chapter IV. Indeed many of the lines can be directly correlated to equations shown there. The most important of these though is line 25, which is directly derived from (4.15). This code effectively gives the amplidue, phase, and group delay response of an optical ring resonator. Changes in any of the ring's fundamental quantities (coupling constant, round trip loss, or feedback delay time) will correspondingly change the response.

```
1  % ******************
2  % Basic Ring Response
3  % ******************
4
5  lambda = 1530e-9;
6  c = 299792458;
7  fmin = c/(lambda+1e-10);
8  fmax = c/(lambda-1e-10);
9  df = (fmax-fmin)/1000;
10 freqaxis = fmin:df:fmax;
11
12 theta1 = 0.25*pi;  % 50% power coupling (kappa = 0.5)
13
14 ng = 2.4;
15
16 L = 12e-3;        % 12 mm round trip length
17
18 FSR1 = c/(L*ng);  % ~= 10 GHz Free spectral range
19
20 z = exp(1j*freqaxis*2*pi./FSR1);
21
```

```
ring_loss = 0;                % db/round-trip
gamma = 10^(-ring_loss/20);   % = 1 for lossless rings

Ring_filt_1 = (cos(theta1) - gamma.*z.^-1) ./ (1 -
   cos(theta1).*gamma.*z.^-1);

Group_delay_D1 = -diff(unwrap(angle(Ring_filt_1)))/(2*pi*df);
```

The second piece of sample code relates to the simulation of rings undergoing rapid changes to their fundamental quantities. The digital filter theory approach to ring simulations assumes stationary ring quantities; therefore this theory needs to be altered slightly for time-varying simulations. This approach is somewhat similar in structure to (4.13). The function shown below was used for all the simulations of time-varying ring responses in Chapter VII.

```
function [y] =
   lossyTVAPF(N,Fsamp,FSR,th,ringlossdb,ModFreq,ModAmp,ModOffset)
% also see Bilbao, IEEE Sig Proc Lett, 2005
% N = number of samples
% Fsamp = sample frequency
% FSR = Ring Free Spectral Range
% th = Ring coupling coeff
% ringlossdb = Ring round trip loss in decibels
% ModFreq = Frequency of Ring feedback modulation
% ModAmp = Amplitude of Ring feedback modulation
% ModOffset = DC ofseed of Ring feedback modulation

c=cos(th)*ones(1,N);
s=sin(th)*ones(1,N);

t = (1/Fsamp):(1/Fsamp):(N/Fsamp);

phi = cos(2.*pi.*t.*ModFreq).*ModAmp + ModOffset;

M = round(Fsamp/FSR);

x = ones(1,N);
y = zeros(1,N);
ph = zeros(1,N);
ls = 10^(-ringlossdb/10);
for cnt=1:M
    y(cnt)=c(cnt)*x(cnt);
end
for cnt=(M+1):N
    ph(cnt-M)=ls.*exp(-1j*phi(cnt-M));    % Round Trip phase
```

```
30      y(cnt)= c(cnt)*x(cnt) + s(cnt)/s(cnt-M)*ph(cnt-M)*(c(cnt-
       M)*y(cnt-M) - x(cnt-M));  % Ring Feedback Equation (eq 16 from
       Bilbao paper)
31 end
```

VITA

Donald Benjamin Adams was born in Provo, Utah. He received his B.S. degree (electrical engineering) from Brigham Young University, Provo, Utah in 2004. He started pursuing his Ph.D. degree at Texas A&M University in Sept 2004, working with dynamically tunable integrated optical ring resonators, and received his degree in 2010. He can be reached at the following address:

Donald Benjamin Adams

Microsystems Engineering

Rochester Institute of Technology

77 Lomb Memorial Drive

Rochester, NY, USA 14623